IDENTIFYING SPATIAL PATTERNS OF STORM DRIVEN FLOODING AND EROSION AT NELSON LAGOON, ALASKA

By

Reyce C. Bogardus, B.S.

A Thesis Submitted in Partial Fulfillment of the Requirements

for the Degree of

Master of Science

in

Geosciences

University of Alaska Fairbanks

May 2021

APPROVED:

Chris Maio, Committee Chair
Daniel Mann, Committee Member
Jacquelyn Overbeck, Committee Member
Paul McCarthy, Chair
Department of Geosciences
Kinchel Doerner, Dean
College of Natural Sciences and Mathematics
Richard Collins, *Director of the Graduate School*

ABSTRACT

This project quantifies localized potential for shoreline change and flooding at Nelson Lagoon, a small fishing community located on the Bering Sea coast of the Alaska Peninsula. The overall goal of this project is to generate societally relevant and locally applicable map and data products through synergistic relationships with federal, state, private, tribal, and public partners. This project intends to substantiate anecdotal observations by local residents, with the ultimate goal of informing erosion and flooding mitigation efforts moving forward.

Long-term trends of shoreline change were measured using multi-temporal orthorectified aerial imagery between 1983 and 2019, while annual changes in shoreline morphology were measured via cross-shore elevation profiles using a survey grade Real-time-Kinematic Global Navigational Satellite System (RTK-GNSS). Shoreline positions were extrapolated using linear regression techniques. A digital surface model (DSM) of the community was derived using Structure-from-Motion (SfM) with >2,400 aerial images collected with an Unmanned Aerial Vehicle (UAV) and used to assess flooding vulnerability after being geodetically referenced and related to a local tidal datum computed by this project. New and existing topographic and bathymetric datasets were compiled and refined into a 6,000 km^2 topobathymetric "seamless elevation" model of the Nelson Lagoon area, over which storm-tide induced currents were simulated using Delft3D FM Suite HMWQ.

Remote sensing records indicate that the Nelson Lagoon spit elongated by more than 800 m and narrowed with an average Net Shoreline Movement (NSM) of -16.9 m between 1983 and 2019 (distal end not included). Though, NSM values show high variability (σ = 21.9 m) and the lagoon and seaward sides of the spit are exhibiting very different erosional regimes. On both sides of the spit, episodes of rapid erosion mainly occurred during high storm-tide events that coincided with significant wave action. For this reason, the long-term erosion rates ultimately reflect the combined erosional impact of just a few storm events. Sand dunes in the supratidal zone on both sides of the spit are eroding at the vegetation line while the dune face retreats landward. By assessing erosion and flooding vulnerabilities for the Nelson Lagoon community, this study adds to an ever-growing database of such assessments statewide; which, ultimately, advance our understanding of regional coastal change in a shifting environment.

[This page is intentionally left blank]

TABLE OF CONTENTS

Page

LIST OF FIGURES

Page

LIST OF TABLES

Page

LIST OF APPENDICES

Page

LIST OF ABBREVIATIONS

AA	Arctic Amplification
ACGL	Arctic Coastal Geoscience Laboratory
ADEC	Alaska Department of Environmental Conservation
ADLWD	Alaska Department of Labor and Workforce Development
ADVs	Acoustic Doppler Velocimeters
AFZ	Arctic Frontal Zone
AGU	American Geophysical Union
AHAP	Alaska High Altitude Photography
AIJ	Alaska Institute for Justice
ANTHC	Alaska Native Tribal Health Consortium
AOOS	Alaska Ocean Observing System
ASG	Alaska Sea Grant
ASOS	Automated Surface Observing System
CIFAR	Cooperative Institute for Alaska Research
DCRA	Division of Community and Regional Affairs
DGGS	Department of Geologic and Geophysical Surveys
DLG	Dillingham
DSAS	Digital Shoreline Analysis System
DSM	Digital Surface Model
DTM	Digital Terrain Model
EPR	End Point Rate
ESRI	Environmental Systems Research Institute
FEMA	Federal Emergency Management Agency
FM	Flexible Mesh
GAO	Government Accountability Office
GCP	Ground Control Point

GIS	Geographic Information System
GLONASS	Global Orbiting Navigation Satellite System
GNSS	Global Navigation Satellite System
GSA	Geological Society of America
IfSAR	Interferometric Synthetic Aperture Radar
MHW	Mean High Water
MLLW	Mean Lower Low Water
MSL	Mean Sea Level
MSLP	Mean Sea Level Pressure
NASA	National Aeronautics and Space Administration
NAVD88	North American Vertical Datum of 1988
NIR	Near-infrared
NLG	Nelson Lagoon
NNK	Naknek
NOAA	National Oceanographic and Atmospheric Administration
NSF	National Science Foundation
NSM	Net Shoreline Movement
NWS	National Weather Service
OPUS	Online Positioning User Service
PDO	Pacific Decadal Oscillation
PDOP	Position Dilution of Precision
QAPP	Quality Assurance Project Plan
RGB	Red, Green, Blue
RMS	Root Mean Square
RSL	Relative Sea Level
RSLR	Relative Sea Level Rise
RSS	Root Sum Square
RTK	Real-time Kinematic

SECD	Strategic Economic and Community Development
SfM	Structure-from-Motion
SIFT	Scale-Invariant Feature Transform
SONAR	Sound Navigation and Ranging
SVTM	Single Value Threshold Map
TBC	Trimble Business Center
TIN	Triangulated Irregular Network
TWL	Total Water Level
UAV	Unmanned Aerial Vehicle
UNAVCO	University NAVSTAR Consortium
USACE	United States Army Corps of Engineers
USGS	United States Geologic Survey
WCI	Weighted Confidence Interval
WEAR	Waste Erosion Assessment and Review
WIS	Wave Information Study
WLR	Weighted Linear Regression Rate
WMO	World Meteorological Organization
WR2	Weighted R Squared

ACKNOWLEDGEMENTS

This research was funded by the Cooperative Institute for Alaska Research (CIFAR) as well as Alaska Sea Grant (ASG), with generous support from the National Science Foundation (NSF) (Grant # 1848542). I would like to thank Uma Bhatt, Nancy Fresco, and Sarah Garcia from CIFAR – their assistance allowed for the training I received from Deltares Institute as well the site visit to Nelson Lagoon in 2019. A special thank you to Ginny Eckart and Christina Sutton from ASG for their persistent support in enabling my research and education.

I would also like to thank the Nelson Lagoon Environmental Depart for their continued communication and assistance on the ground at Nelson Lagoon; thank you so much Mark McNeley, Angela "Angie" Johnson, and Samantha "Sam" McNeley. I greatly appreciate your help and look forward to our continued collaboration. Thank you to Jared Roberts for your work in 2018 collecting survey data in Nelson Lagoon. Thank you, Ronnie McPherson from HDR Alaska Inc., for taking time out of your busy schedule to talk with me and provide a trove a data from which I could build from. Thank you to Robin Bronen from Alaska Institute for Justice (AIJ) for initiating communication with the Native Village of Nelson Lagoon and moving forward efforts to monitor and record coastal change.

I would like to thank my advisor and committee chair, Dr. Chris Maio, whose unwavering work ethic, and passion for geoscience inspired me to pursue higher education. A big thank you to Dr. Daniel Mann. Your curiosity and discipline in learning has taught me what a true scientist looks like. I would also like to thank Jaci Overbeck; your steadfast dedication to quality and societal applicability has taught me perspective in the science world.

I have received help in various forms from many others over these last three years and am grateful to all of you; thank you Rich Buzard, Vladimir Alexeev, Shira Ellenson, Skye Hart, Harper Baldwin, and Autumn Fournier. I would also like to thank Paul McCarthy and Kinchel Doerner for their review of this document as well as their understanding and flexibility.

Finally, a heartfelt thank you to my parents. I am inspired by you; you have taught me attention to detail, self-honesty, and self-discipline. I promise to always bring pride to our name.

[This page is intentionally left blank]

CHAPTER 1

INTRODUCTION

1.1 Introduction

Alaska has undergone substantial changes over the last few decades in various atmospheric and cryospheric systems and processes (Bader et al., 2011). Typical annual average statewide temperatures are now 3 to 4ºF (~2 to 3ºC) warmer than during the early and mid-20th century (Thoman and Walsh, 2019). This regional warming has been linked to increased storm frequency and intensity in the Bering Sea due, in part, to enhanced land-sea thermal contrast along the Arctic Frontal Zone (AFZ) (Zhang et al, 2004; Day and Hodges, 2018). This rapid Arctic warming relative to northern hemisphere mid-latitudes – referred to as Arctic Amplification (AA) – has been attributed to more frequent high-amplitude (wavy) jet-stream configurations, which also increases the frequency of extreme weather events (warm/cold snaps, storms, etc.) (Wallace and Hobbs, 1979; Francis and Vavrus, 2015). When combined with increased open water days due to the decline in sea-ice, this regime change has increased the occurrence of synchronous changes to shoreline morphology (Jones et al., 2009; Vermaire et al. 2013), rapid habitat degradation through salinization of freshwater and terrestrial ecosystems (Vermaire et al. 2013), and the destruction of infrastructure in coastal communities throughout the region (Graham and Diaz, 2001; Jones et al, 2009; Mesquita et al., 2010; Kinsman and DeRaps, 2012; Farquharson et al, 2018). These effects are especially relevant to Alaskan communities, since, as early as 2003, the United States General Accounting Office (GAO) reported that 184 out of 213 (86%) of Alaska Native villages are affected by flooding and erosion related hazards (GAO, 2003). Understanding the trends and dynamics of these changes along the Bering Sea coast is predicated on grasping both the spatial and temporal variability of storm climatologies in the North Pacific and Bering Sea (Atkinson, 2005; Rachold et al., 2005).

One such community located along the southern Bering Sea coastline is Nelson Lagoon (**Figure 1**), a native community of 50 people located on a narrow sand spit with no road connection to any other community. Essential infrastructure, such as freshwater resources and the airstrip, have

recently experienced substantial storm-driven erosion. The community lies at the historical southern limit of the open ocean sea-ice maximum and, starting over the last few decades, no longer experiences sea-ice each year (AOOS, 2014). This leaves the coastline without a natural barrier to blunt the impact of waves and surge for longer periods of time throughout the year (Vermaire et al. 2013). It also means surface winds have more contact with ocean water over larger areas for longer periods of time throughout the year, producing larger waves and surge (Erikson et al., 2015). This phenomenon has been quantified at St. Lawrence Island in the Bering Sea by Erikson et al. (2015), who found that the magnitude of surge events has increased over the last 30 years. Barrier beach systems are among the most dynamic of depositional coastal landforms and respond rapidly to changes in littoral sediment supply and sea level, as well as to the dynamic processes associated with severe storms including surge events (Mason and Jordan, 1993; Houser et al., 2008; Davidson-Arnott et al., 2019). This makes Nelson Lagoon and similar barrier beach systems that have likewise experienced modern declines in sea-ice extent and duration particularly useful as case studies to determine ramifications of the ongoing regime shift in the oceanographic and climatic conditions in the southern Bering Sea region.

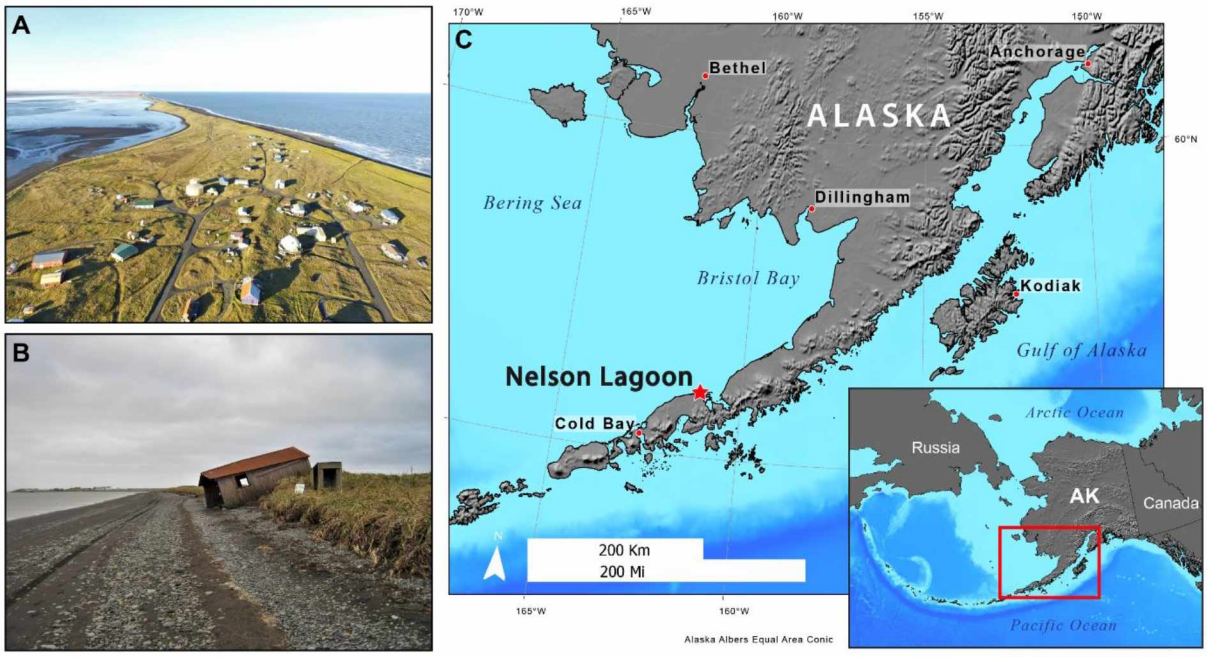

Figure 1. Study site map of the Native Village of Nelson Lagoon. (A) UAV imagery over the residential portion of the community. The right side of the image is the Bering Sea, left side is the back-barrier lagoon. (B) Cross-shore image showing set-net cabin whose foundation has been undercut by storm-driven surge and wave action on the lagoon-side of the spit. (C) Regional map showing Nelson Lagoon's location on the North side of the Alaska Peninsula in Bristol Bay.

This project applies contemporary scientific tools combined with field investigations to determine Nelson Lagoon's vulnerability to flooding and erosion from future storm surge, as well as develop tools for mitigation applications (i.e. Smith, 2014).

1.2 Research Question and Objectives

This goal of this project is to identify spatial patterns of vulnerability to storm driven erosion and inundation at Nelson Lagoon through topographic analyses and by constructing a local hydrodynamic model set up for inclusion in a regional scale storm surge model. This goal was accomplished through the following objectives:

1) Conduct field investigations that include topographic, bathymetric, tide, and sediment surveys; compile climatic and oceanographic datasets.
2) Carry-out change analyses using remote sensing and surveyed datasets to quantify the extent and magnitude of shoreline change and flooding.
3) Construct a "seamless" topobathymetric elevation model and computational grid from existing and new survey data for inclusion in a regional storm surge model using Delft 3D FM.
4) Produce data products that inform community decision making and mitigation strategies.

1.3 Background

1.3.1 Regional Storm Regime

The center of a closed surface cyclonic circulation outside of the tropics is normally referred to as an extratropical cyclone (Jones et al., 2003; Bader et al., 2011). According to the Beaufort Wind Scale, an extratropical cyclone is categorized as a storm when the wind speed attains values greater than 24.5 m/s (55 mph) (WMO, 1970). Storms can last anywhere from 12 and 200 hours (up to >8 days), depending on the season and local geography and can vary in size from the mesoscale (≤1000 km) to synoptic scale (>1000 km). Storms are often associated with damaging winds (Mesquita et al., 2009) and/or strong precipitation in the form of rain and snow and are an integral part of the atmospheric transport of heat, moisture (Sorteberg and Walsh, 2008), and momentum polewards (Yin, 2005; Bader et al., 2011).

While various analyses of storm activity have appeared in the literature, most have focused on the northern hemisphere as a whole, with the Arctic being treated separately in some instances (Keegan, 1958; Whittaker and Horn, 1984; Serreze, 1995; McCabe et al., 2001; Hoskins and Hodges, 2002; Zhang et al., 2004; Sorteberg and Walsh, 2008). Relatively few studies have focused on the North Pacific or Bering Sea region (Mason et al., 1996; Mesquita et al., 2009). This is a serious research gap because recent studies indicate that a warmer Arctic is accompanied by a northward shift in extratropical cyclone tracks (Geng and Sugi, 2003; Fischer-Bruns et al., 2005; Yin, 2005; Bengtsson et al., 2006; Rinke and Dethloff, 2008; Schuenemann and Cassano, 2010; Bader et al., 2011). The Northern Pacific/Bering Sea is one of the two main storm corridors in the Northern Hemisphere (**Figure 2**) (Hoskins and Hodges, 2002; Bernstein et al., 2008; Overland and Wang, 2019), mainly because of the geographical distribution of ocean and land in the Northern Hemisphere, which control the structure and magnitude of meridional temperature gradients (Rodionov et al., 2007).

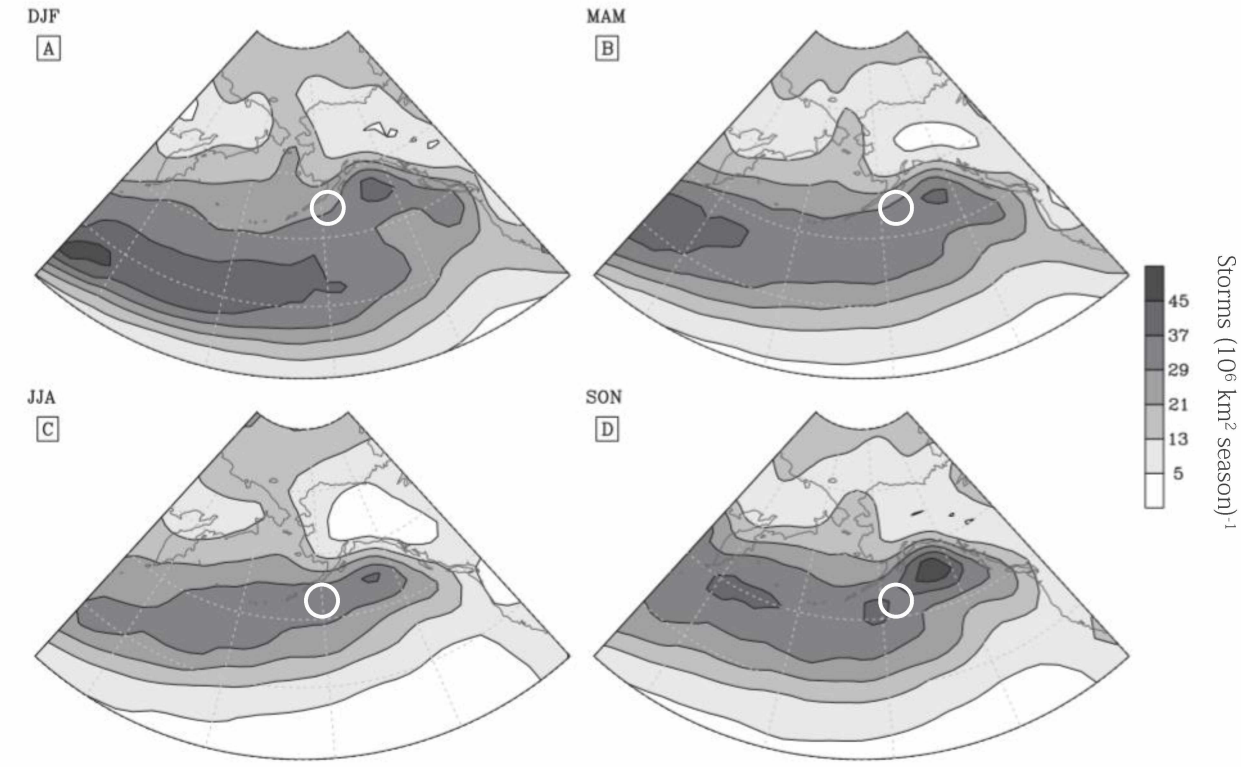

Figure 2. Storm track density climatology in the North Pacific from 1948/49 to 2008. (A) winter (DJF), (B) spring (MAM), (C) summer (JJA), and (D) autumn (SON) seasons. Units: Storms (10^6 km^2 season)$^{-1}$. Location of Nelson Lagoon is noted by the white circles. Notice that Nelson Lagoon observes greater than 20 storms per season on average (after Mesquita et al., 2009).

The Bering Sea is characterized as an area of high lysis density (number of storms that dissipate within a defined region), especially during autumn and winter months (October – February); with winter storms being more intense (Cacchione and Drake, 1979; Overland and Pease, 1982; Sallenger et al., 1983; Mesquita et al., 2009). The principal influence on the Bering Sea surface is the Aleutian Low pressure cell (Mason et al., 1996; Rodionov et al., 2005). The Aleutian Low describes a statistical tendency toward low pressure associated with the passage of storms. One of the most widely used indices for the overall strength of the Aleutian Low is the North Pacific (NP) index (**Figure 3A**), which is related to the Pacific Decadal Oscillation (PDO) (**Figure 3B**) (Trenberth and Hurrell, 1994). When the NP index is positive it means that the Aleutian Low is relatively weak, and when it is negative the Aleutian Low is relatively strong. Rodionov et al. (2007) analyzed the NP index through time and found a correlation between negative NP index values and anomalously warm winters in the Bering region (**Figure 3C**). This occurs because the frequency of storms along the Alaskan track increases dramatically during the climate regimes of a strong Aleutian Low, increasing the overall probability of anomalously warm winters in the Bering Sea. As seen in Fig. 3A over the past 100+ years there were two multidecadal regimes of a strong Aleutian Low (1924–1946 and 1977–2005+) and two regimes of a weak Aleutian Low (1901–1923 and 1947–1976). The overall downward trend (increased storminess) in the NP index is noteworthy.

A study by Sepp and Jaagus (2011) found that the trend in the annual total number of cyclones in the Arctic increased by 55.8 cyclones over the period 1948–2002 and that the greatest increase in the frequency of cyclones was during the winter. There was a significant increase in the frequency of cyclones that specifically moved into the Arctic basin through the Bering Strait (Sepp and Jaagus, 2011). Moreover, the same study identified that the sea level pressure of Arctic cyclones showed a significant decreasing trend of 2.5 hPa (stronger storms) over the same study period.

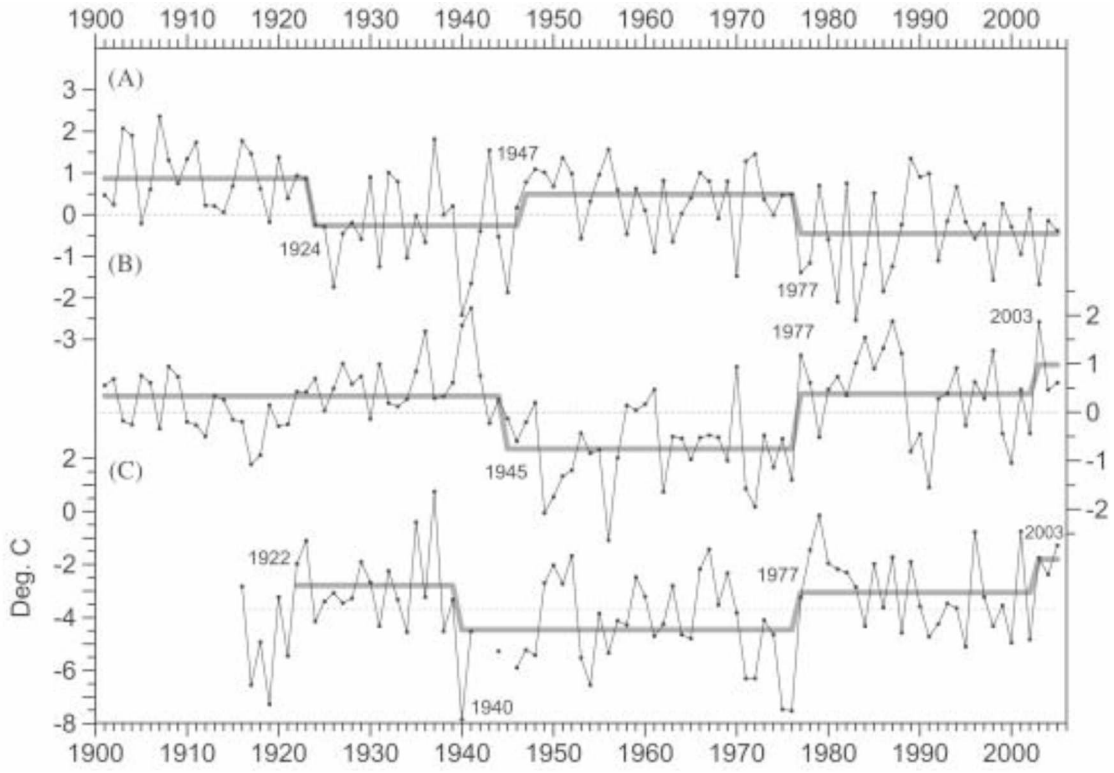

Figure 3. Plot showing the last hundred years of the mean winter (DJFM) North Pacific index, Pacific Decadal Oscillation Index, and surface air temperature in the Bering Sea. (A) North Pacific index, 1901–2005, unitless (B) Pacific Decadal Oscillation index, 1901–2005, unitless, and (C) surface air temperature in Celsius at St. Paul, 1916–2005. Bold gray lines characterize regime shifts calculated using the sequential method (from Rodionov et al., 2007).

1.3.2 Regional Sea Ice Regime

Sea-ice extent and duration strongly influence Arctic and Subarctic coastal dynamics, and changing climate is now altering the sea-ice regime of the Bering Sea (Farquharson et al., 2018). Open ocean sea-ice is an important moderator of wave fetch and water temperature, and shorefast sea-ice shields coastlines from wave action. Specifically, the extent of sea-ice has an inverse relationship with wave fetch, height, and swell size in Arctic seas (Stabeno et al., 2007; Francis et al., 2011; Overeem et al., 2011; Thomson and Rogers, 2014; Thomson et al., 2016), with the open-water season having the most wave energy available for coastal erosion and sediment transport (Overeem et al., 2011; Farquharson et al., 2018). Storms during the ice-free season generate the most geomorphologically significant wave events along Arctic coastlines and, hence, strongly influence coastal processes (Reimnitz et al., 1994; Mason et al., 1996; Forbes, 2011; Barnhart et al., 2014; Farquharson et al., 2018).

Winter ice formation in the Bering Sea has been described using the "conveyor belt" analogy (e.g., Muench and Ahlnas, 1976; Pease, 1980; Burns et al., 1981) in that sea-ice forms along the south facing coasts where polynyas (an open stretch of water) develop as the predominantly northerly winds carry sea-ice southward away from the coasts. Major polynyas occur south or down-wind of the Chukchi Peninsula, St. Lawrence and St. Matthew islands, and the Seward Peninsula. Sea-ice is then blown southward until it reaches warmer water where it melts, cooling the SST and allowing the ice edge to move southward (Stabeno et al., 1999; Stabeno et al., 2007; Danielson et al., 2011). In recent history, the southward edge seldom extended farther south than the deep water of the Aleutian basin south of the Bering Sea continental shelf (**Figure 1**).

The rate and dynamics of the sea-ice conveyor belt is strongly influenced by regional winds on a year-to-year basis (Zhang et al., 2010). Ice drift rates vary from 17 to 22 km/day to as fast as 28-32 km/day (Shapiro and Burns, 1975; Muench and Ahlnas, 1976; Weeks and Weller, 1984). In the Bering Strait, speeds as fast as 50 km/day have been observed, although there are reversals driven by wind events (Pease, 1980; Stabeno et al., 1999). Thus, the amount of ice moving south fluctuates considerably from year to year because of the substantial interannual variability of the winter northeasterly winds, which are linked to the location and intensity of the Siberian High and the Aleutian Low (Overland et al., 1999; Stabeno et al., 2001; Stabeno et al., 2007). The position of the mean ice edge during winter and early spring (January to April) is farthest south and relatively stable until April, after which the ice edge begins to retreat northward (Jones et al., 2020). By June, the ice edge has typically retreated northward through the Bering Strait, and by September, reaches its northernmost position off the continental shelf in the Chukchi and Beaufort Seas (Frey et al., 2015).

Over the past three decades, there have been significant changes in the timing and extent of sea-ice cover across the Bering, Chukchi, and Beaufort Seas (Jones et al., 2020). Satellite data reveal that patterns in sea-ice cover have been spatially heterogeneous through time, with significant declines of sea-ice extent in the Chukchi and Beaufort Seas, and complex multi-year variability in the Bering Sea south of St. Lawrence Island (**Figure 4**) (Frey et al., 2015). Stabeno et al. (2012) describe this multi-year variability in sea-ice cover over the southeastern Bering Sea shelf as involving oscillations between warm years (e.g., 2001–2005) with less extensive ice (driven

by weak, easterly winds) and cold years (e.g., 2007–2012) with more extensive ice (driven by cold, northerly winds). For example, the period 1979 to 2000 was characterized by high interannual variability in sea-ice, 2001 to 2005 was characterized by relatively low sea-ice cover, and 2006 to 2012 was characterized by relatively high sea-ice cover (AOOS, 2014; Frey et al., 2015). A weakened/wavy jet stream due to AA is associated with this increased variability in sea-ice cover across the Bering Sea (e.g., Wendler et al., 2014), a connection made evident by a shift from dominantly positive PDO values to more negative values over the last decade (Frey et al., 2015).

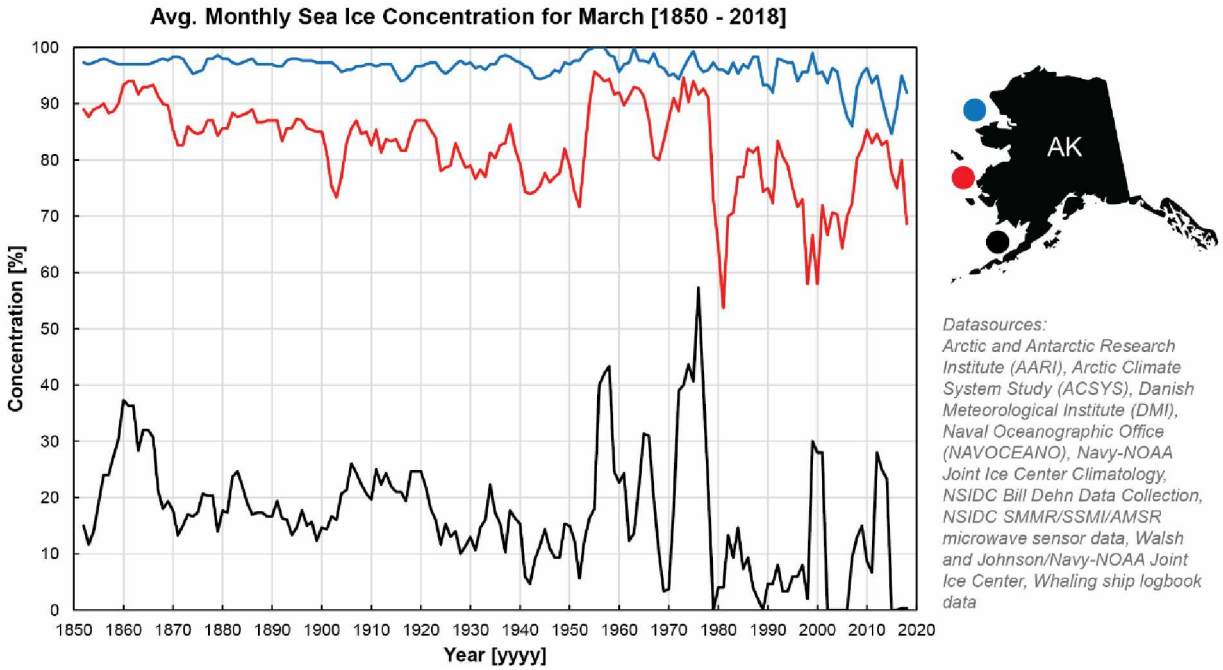

Figure 4. Megatransect of sea-ice concentrations for the month of March between 1850 and 2018 compiled from the Alaska Ocean Observatory Network (AOOS) Sea Ice Atlas. (0–30%) Open Water to very open drift, (30–90%) open drift to close pack, (90–100%) very close pack to compact. The black, red, and blue points in the upper right inset map correspond to the black, red, and blue sea-ice time series in the main graph. Notice how sea-ice in the Bering Sea (black) no longer consistently observe sea-ice each year (2000 onward).

The impacts of record low sea-ice extents in the Bering Sea since 2012 have been widespread and profound (Overland et al., 2011), including unprecedented weather events (Thoman et al., 2020), marine wildlife die-offs (Thoman et al., 2020), and sightings of animals outside of their normal range (Herring et al., 2018). Most pertinent to this project's analysis of storm-driven

flooding and erosion, though, is the impact that the regional decrease in sea-ice extent has on wave and surge generation, as well as on storm tracks in general. Overland and Pease (1982) examined the relationship between interannual variations in Bering Sea maximum sea-ice extent and Pacific storm tracks. They found that sea-ice extent in a given winter appears to be primarily controlled by the tracks of storms entering the Bering Sea and, to a lesser extent, by the number of storms. In years of greatest ice extent, fewer storms entered the region, and low-pressure centers were quasi-stationary in the western Gulf of Alaska and southeastern Bering Sea (Rodionov et al., 2007). Given this context, quantifying the geomorphic response to shifts in the sea-ice regime at Nelson Lagoon, which no longer observes sea-ice from year-to-year, can forewarn communities located further north along the Bering Sea coastline who may soon experience comparable changes in the sea-ice regime in their locations.

1.3.3 Erosion / Flooding

Coastal erosion is of increasing concern to rural Alaskan communities in Bristol Bay; however, direct topographic and hydrographic measurements remain absent along much of this coastline (Overbeck, 2018; Buzard et al., 2020). Currently, a great deal of effort is being made by public, private, and government agencies to address this data gap. As explored in detail below, coastal erosion in Bristol Bay is primarily caused by the combined effects of ocean currents, wave action, and storm surge, with wave action being the predominant cause (Sharma et al., 1972; Stockdon et al., 2006). Coastal erosion is usually described in terms of sediment transport in and out of an along- and cross-shore cell, where the volume and direction of material movement is quantified (Bergillos et al., 2017). The rate of sediment transport is dependent upon wave energy and wave direction along a reach of coastline, as well as the composition of a shoreline (USACE, 2019). The most dynamic shorelines are those composed of coarse to fine sand, as is the case for Nelson Lagoon, because these are the particle sizes most easily transported by wave action (Green and Coco, 2014; USACE, 2019). Nelson Lagoon's sandy beaches are fringed in the supratidal zone by foredunes created by sand transported by wind action (Hoyt, 1967; Davidson-Arnott et al., 2019). Wave action, however, is the primary driver of coastal change at Nelson Lagoon. Net erosion of the dunes along Nelson Lagoon has been constant for at least the last 40 years, though long-term averages of erosion along the Nelson Lagoon's foredune are generally the result of short-term severe events with substantial wave action and run-up (Nelson Lagoon

SECD, 2001), when the equivalent of multiple years' worth of "normal" sediment transport can occur (i.e. Hume and Schalk, 1967; Dygas and Burrell, 1976). Shoreline erosion at and up current of Nelson Lagoon supplies a major contribution to the sediment budget of the spit, a contribution likely much larger than that of riverine input (i.e. Reimnitz and Maurer, 1979).

Coastal *flooding* is caused by elevated water levels due to highest astronomical tides, wave setup, and storm surge. Astronomical tides are long-period waves that move through the oceans in response to the differential forces of gravity exerted on the Earth by the moon and sun (Gross, 2007). Tides originate in the oceans and progress toward the coastlines where they appear as the regular rise and fall of the sea surface. There are differences between the time and amplitude of measured tides at a location from those predicted solely from consideration of astronomical factors (Haigh et al., 2020). Leaving aside sea level changes due to meteorological factors, these differences arise from the irregular distribution and shape of land masses on the Earth's surface, the interaction of the tidal waves with the ocean bed and the land margins, the effects of inertia of the water mass and the Coriolis force produced by rotation of the Earth (Davidson-Arnott et al., 2019).

1.3.3.1 Storm surge

Coastlines also experience short-term water level fluctuations, which can either enhance or dampen the tidal signal. During storms, changes in sea level occur as a result of wind stress on the water surface as well as deviations in atmospheric pressure leading to positive displacement of the water level (storm surge or set-up) or negative displacement (negative surge or set-down). For example, there is a change in sea level of about 1 cm for every 1 millibar (roughly 0.1 kPa) in atmospheric pressure (Fu and Pihos, 1994). As a result, sea level responds not only to pressure changes associated with weather systems but also to seasonal changes in pressure (Davidson-Arnott et al., 2019). As such, tide levels are, on average, higher during the autumn which exacerbates storm surge (Fok, 2012).

1.3.3.2 Wave run-up

In addition to elevated water caused by storm surge, waves can wash up over the beach causing inundation, breaching, and overwash (Sallenger, 2000). Wave run-up is the sum of wave set-up

and swash uprush and is added to the water level reached as a result of tides and storm setup. Runup is a complex phenomenon that depends on the local water level (including surf beat or infragravity wave effects), the incident wave conditions (height, period, steepness, direction), and the nature of the beach or structure being run-up (e.g., slope, reflectivity, height, permeability, roughness) (Dean et al., 2005; Weaver, 2008). As such, *total* water level (TWL) is a summation of the processes discussed above (Erikson et al., 2018) and can be generalized as the combination of 1) a static (or assumed static or slowly varying) mean water level associated with astronomical tides, storm surges, and wave setup; and 2) a fluctuation about that mean (swash) associated with surf beat and the motion of individual waves at the shoreline (**Figure 5**).

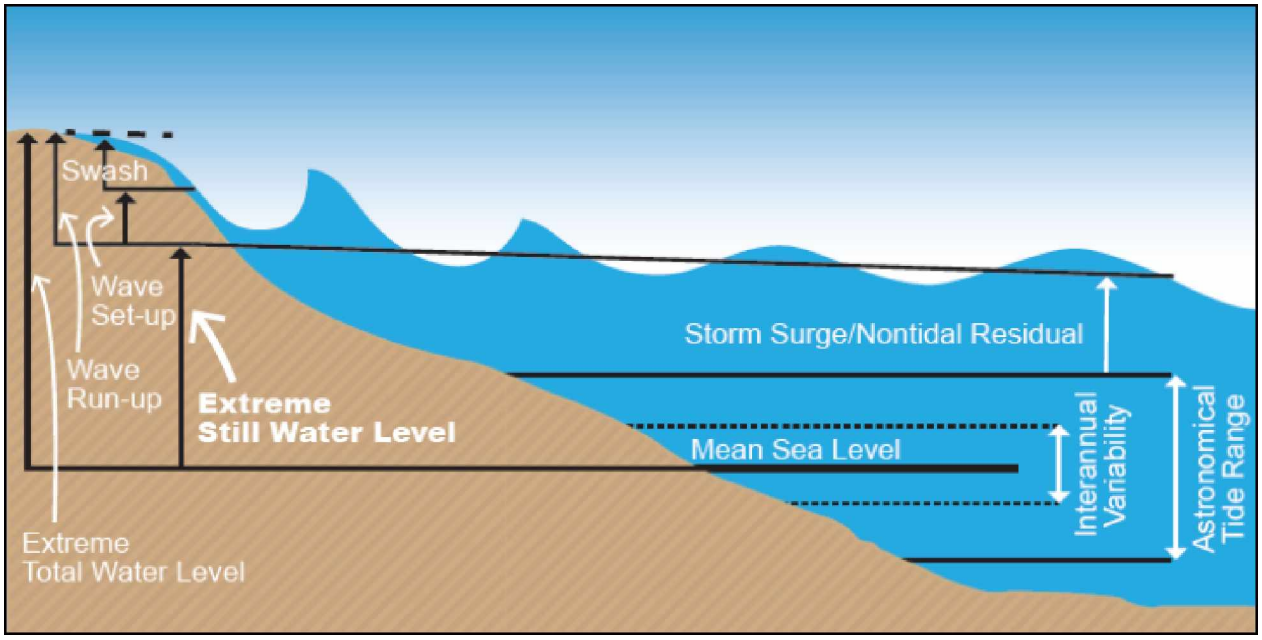

Figure 5. Diagram showing the various components of Total Water Level (TWL); waves, tides, and nontidal residuals. After Moritz et al., 2015.

Wave run-up can add meters to the total water level on the open ocean coast, which is not only very important for inundation levels but also controls the elevation of the primary dune toe and wave impact hours as computed from a TWL time series (Ruggiero et al., 2001; Ruggiero, 2004). Extreme TWLs in Nelson Lagoon have interfered with access to the community dock and airstrip facilities multiple times over the last 30 years (USACE, 2007). However, minimal or no data are available that document these events, which means that there are no past TWL elevations to compare future flooding events to for historical context (Buzard et al., 2020).

1.4 Study Site

Nelson Lagoon is one of six communities in the Aleutians East Borough. It comprises 635 km^2 of land and 510 km^2 of water and was specifically established to take advantage of commercial fishing opportunities (Nelson Lagoon SECD, 2001). Historically, Nelson Lagoon was an Aleut summer fishing camp along the adjacent Bear River. The lagoon was named in 1882 after Edward William Nelson of the U.S. Signal Corps, an explorer in the Yukon Delta region between 1877 and 1920. A Salmon saltery operated from 1906 to 1917, which attracted Scandinavian fisherman, but there has been no cannery since then. Starting in 1965 the community has been occupied year-round (Nelson Lagoon SECD, 2001). Since 2018, the UAF Arctic Coastal Geoscience Lab (ACGL) has maintained erosion monitoring sites for the community Environmental Department, which include measuring stakes along predetermined cross-shore transects and continuously operating time lapse cameras.

1.4.1 Demographics

According to the 2010 Census, Nelson Lagoon has a population of 52 – down from 83 as reported in the 2000 and 1990 Census. The majority (78%) of the population is Alaska Native. There are 32 housing units in the community, of which 22 are currently occupied. Of the 10 vacant units, 9 are for seasonal, recreational, or occasional use (HDR, 2011).

1.4.2 Economy

As of 2009, 23 residents hold commercial fishing permits, primarily for salmon gillnet. Though, some subsistence and trapping activity also occurs. Local government is the largest employment source, comprising 42% of the community's workers (ADLWD, 2011). The breakdown of employment sectors are as follows:

- Local government (42%)
- Education and health services (19%)
- Trade, transportation, and utilities (10%)
- Professional and business services (10%)
- Financial activities (10%)
- Information (3%)
- Other (6%)

1.4.3 Transportation

Access to the community is generally via two facilities:

- A State-owned 1,200 m long by 25 m wide gravel airstrip, which is available year-round and located approximately 2 km east of the community. Scheduled air service is generally available three days a week via Cold Bay.
- A dock facility located approximately 1.5 km east of the community. This dock is approximately 80 m long with several berthing areas and is large enough to receive commercial barges. There is also a boat loading ramp for smaller craft.

Within the community, transportation is generally via the unpaved road system constructed primarily of sand or along the beaches. Motorcycles, four-wheelers, and pickups are the modes of transport within the community.

1.4.4 Infrastructure

According to the Source Area Assessment for Nelson Lagoon (ADEC, 2004), the Nelson Lagoon water system is a Class A, 145 liter per minute water system that obtains water from a lake located approximately 15 km west of the community. A four-inch-diameter pipe transfers water from the intake/pump to the community's 2.2 million liter holding tank (Nelson Lagoon SECD, 2001) located on a former foredune near the north side of the beach (**Figure 6**). Initially, the pipe was located above ground, but two years after construction, the line was buried approximately two to four feet below the surface, but the location of the air valves and the pipe was not recorded, and thus the exact location of the line is generally unknown (CE2, 2002). During several erosional events, the pipe was exposed and damaged; >300 m of pipe had to be replaced due to damage. Community water lines have been replaced three times in past years due to erosion and storm damage (costs were not reported) (USACE, 2007).

Most of the community is served with individual wastewater (septic) disposal systems since there is not an identified central treatment or discharge location. The buildings in the community (**Figure 6**) are served by power and telephone lines above and below ground. Community electricity is provided by diesel generators.

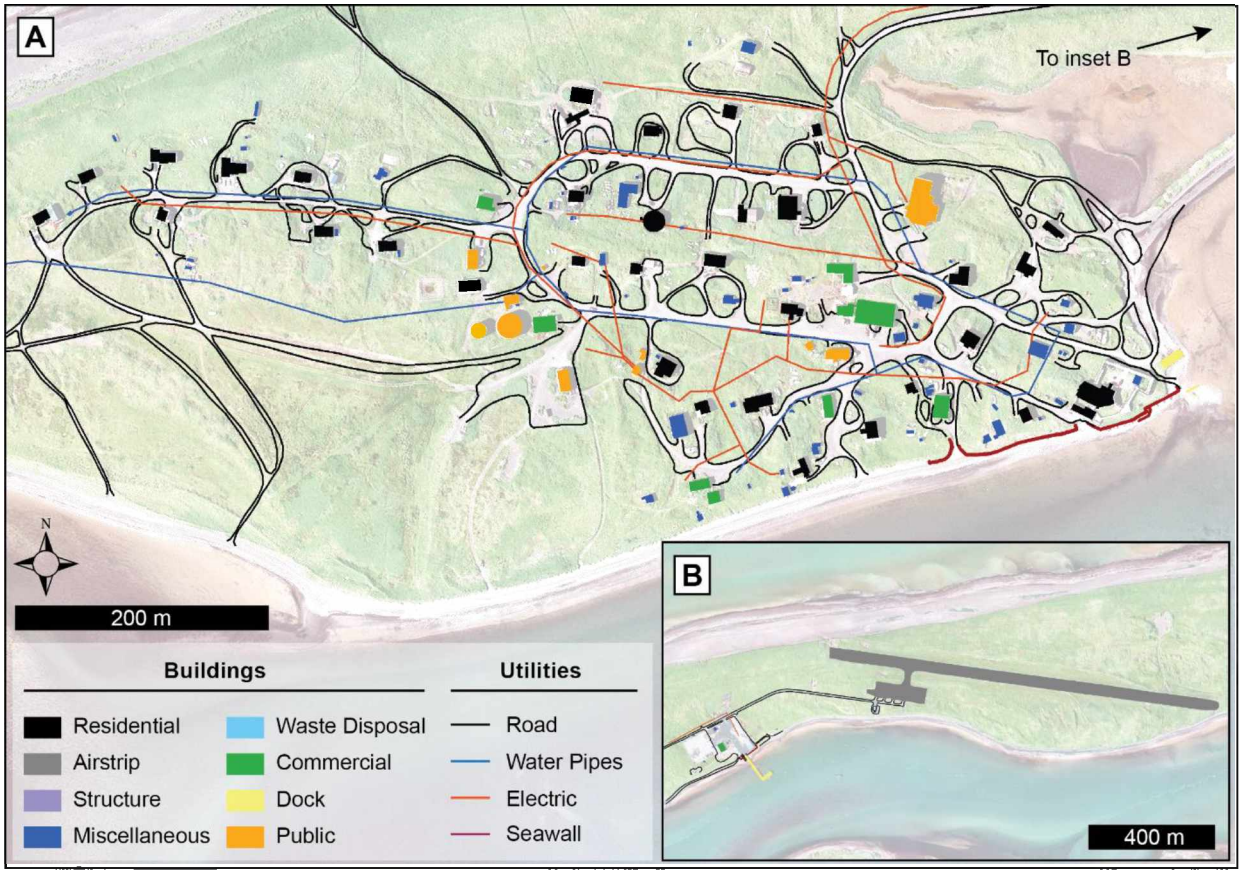

Figure 6. Map showing the building and utility infrastructure of Nelson Lagoon. (A) The residential portion of the community, (B) the tank farm, dock, and airstrip. Data are displayed over an orthoimage collected in 2013 by Kodiak Mapping Inc.

Solid waste disposal for Nelson Lagoon consists generally of disposing of refuse in shallow trenches approximately 1 km west of Nelson Lagoon. The refuse in the trenches is burned to reduce volume. Items such as old propane tanks, vehicle parts, and heavier metal items are segregated and stored in the solid waste disposal area (WEAR, 2015).

The fuel tank farm is located near the dock facility, approximately 1.5 km east of Nelson Lagoon. This relatively new fuel facility provides fuel storage for vehicles, power generation, and structures. The tanks are located within a bermed containment area. Buried fuel lines transfer product from the dock area to the fuel farm. Trucks and potentially other vehicles are utilized to deliver fuel oil to individual buildings.

Most of the buildings and facilities in the community are constructed on timber foundations and on shallow post and pad foundations at the ground surface. The base of most structures are generally skirted with plywood. In limited instances, buildings are on concrete footings. Due to the relatively high permeability of the sand, drainage problems around the structures are generally not observed. There is also no indication of significant settlement occurring at any of the buildings (HDR, 2011).

The community utilizes a combination of road systems in the interior portions of the community and the beaches for travel otherwise. The road surface is composed of medium to fine sand with low silt content. There is little in the way of fines (silt sized or smaller materials) to bind the sands together on the interior road surfaces, thus, the roads are subject to pushing and rutting (HDR, 2011). In some areas, gravel has been added to the road surface to provide a driving surface. In beach areas, driving is generally performed on moist to wet areas or areas with gravel to reduce the pushing and rutting.

1.5 Environmental Setting

1.5.1 Geography [Bristol Bay Region / Alaska Peninsula]

Bristol Bay is a low-salinity, meso-tidal embayment of the southern Bering Sea, with an approximate 0.2 m/km regional gradient. Tidal energy accounts for 60 – 90% of the horizontal kinetic energy produced over the Bristol Bay shelf (Kinder and Schumacher, 1981), which is characterized by water depths <120 m with an average depth of approximately 50 m (Johnson, 1983). The shelf break is located at a depth of 180 m. The Bristol Bay coastline of the Alaska Peninsula includes six large embayments protected from the open ocean by barrier islands and spits. The non-embayed beaches of this coastline are typically backed by dunes or bluffs of varying height that are eroded into unconsolidated deposits (Kinsman and Gould, 2014). Sand and gravel type beaches are typical, and they experience a wave energy regime that declines eastwards along the coastline (Jordan, 2001; Kinsman and Gould, 2014).

The Nelson Lagoon spit lies west of the Kudobin Islands and forms a barrier complex across the mouth of the Bear River, which flows along the entire southern flank of the spit. The spit is approximately 19 km long, reaches 1,400 m at its widest point, and narrows to only 120 m at its

narrowest point. Of the occupied sections of the spit, its width ranges from approximately 300 m (at the solid waste disposal site) to 650 m (at the residential area). The vegetation over the spit is predominantly dune grass (*Leymus mollis*). A large, wave generated foredune between 4 and 13 m in elevation runs along the entire Bering Sea side of the spit. The elevation of this incipient dune nearest the residential section of the community is generally between 7 and 10 m (**Figure 7**). There are breached portions of the seaward dune and over washing occurs during high storm-tide events, typically in the autumn and winter months. Beach morphology is more tidally influenced on the lagoon-side of the spit with substantially lower foredune crest elevations (2 – 5 m) and extensive mud flats. As erosion advancsea sidees on both sides, the spit is getting longer and narrower through time (*section 4.2*) (USACE, 2007).

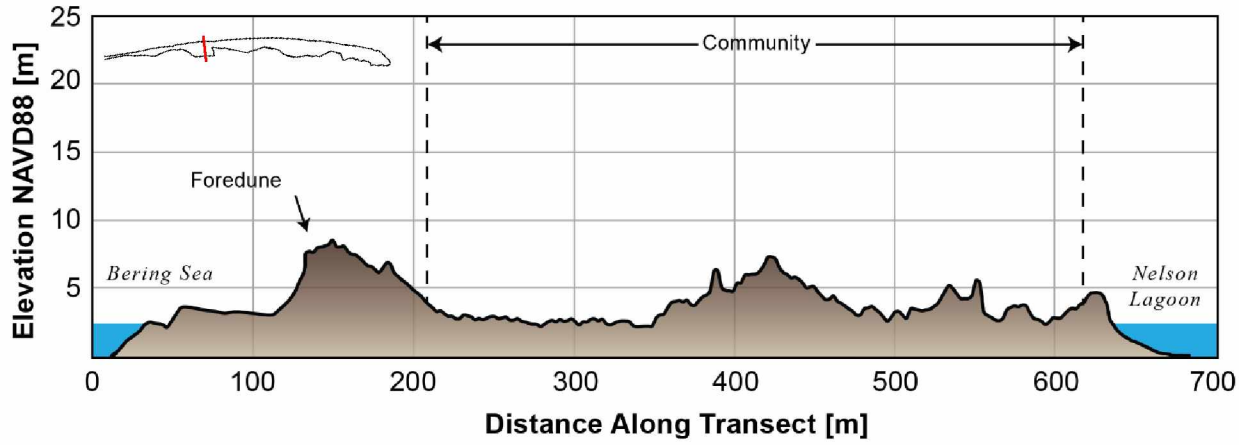

Figure 7. Cross-section of the Nelson Lagoon spit where the residential area is located. Elevation data is from 2019 and is comprised of RTK-GNSS profiles as well as SfM-derived surfaces from UAV imagery. A smoothing kernel of 2 m has been applied. Notice the different dune heights and morphologies between the Sea and Lagoon sides of the spit.

The lagoon itself covers an area of approximately 130 km^2 and is mostly shallow (0.5 – 2 m), with deeper, tidally incised channels (3 – 15 m) that permit maritime navigation. The geometry of the lagoon is such that, though it is a mostly protected stretch of open water, there is up to 9 km of fetch from the most inland shoreline and the Nelson Lagoon spit.

The major sediment sources are the sediment discharge from streams, sediment eroded directly from the shoreline by wave action, ash fall from volcanoes bordering the sea, and material transported into the area from ocean currents (Johnson, 1983). D90 sediment size of Nelson

Lagoon's Bering Sea fronting beach ranges from 0.5 to 1.75 mm (portion of particles with diameters below this value is 90%), with cobble-sized consolidated rock atop various storm terraces along the beach profile (fieldnotes, 2019) (**Figure 8**).

Figure 8. Cross-shore photograph taken in 2019 on the Bering Sea side of the Nelson Lagoon spit near the community. Notice the winter berm and the eroded face of the foredune.

1.5.2 Geologic Setting

The geology of the immediate Nelson Lagoon area is comprised of unconsolidated and poorly consolidated surficial deposits of Quaternary, Pleistocene, and Upper Tertiary age (**Figure 9**) (Wilson et al., 2015). The geology to the south predominantly consists of volcanic and sedimentary rocks of Tertiary to Eocene age (Wilson et al, 2015). The spit itself lies in a low-relief coastal plain adjacent to the inner shelf of the Bering Sea, with an abundance of unconsolidated detritus (Glaeser, 1978).

Nelson Lagoon's location along the Alaska Peninsula makes it part of the North American tectonic plate which is the overriding plate of the Aleutian subduction complex. The Pacific plate is subducting along the Aleutian trench at a rate of approximately 6 to 8 cm/yr (Grow and Atwater, 1970; Cooper et al., 1976). This regional subduction has given rise to the magmatism on the Alaskan Peninsula, Unimak, and Amak Islands and the tensional Amak and Bristol Bay grabens which have formed on the continental shelf, in the tectonic back-arc area (Marlow et al., 1976; Jordan, 2001). The tectonic setting of Nelson Lagoon is unusual, in that it is located in the Shumigan Gap, which is characterized by a lack of plate motion and, therefore, lack of seismic activity. The Shumagin seismic gap extends from the western end of the rupture zone of 1938 to the eastern end of the 1946 earthquake (Davies et al., 1981). The Shumagin seismic gap, had not ruptured during a great earthquake since at least 1899-1903 before a Mw 7.8 earthquake occurred in July 2020 (*see section 4.3.2*).

In summary, the coastal zone of the Alaska Peninsula is a moraine- and outwash- mantled lowland, with local relief of about 3 to 75 m. There are also relict sea level stand terraces in the area (dates unknown); a testament to the complex sea level history in the last 100,000 years which can be directly attributed to climatic and glacial fluctuations (Johnson, 1983) and/or earthquake deformation cycles (*see section 4.3.2*).

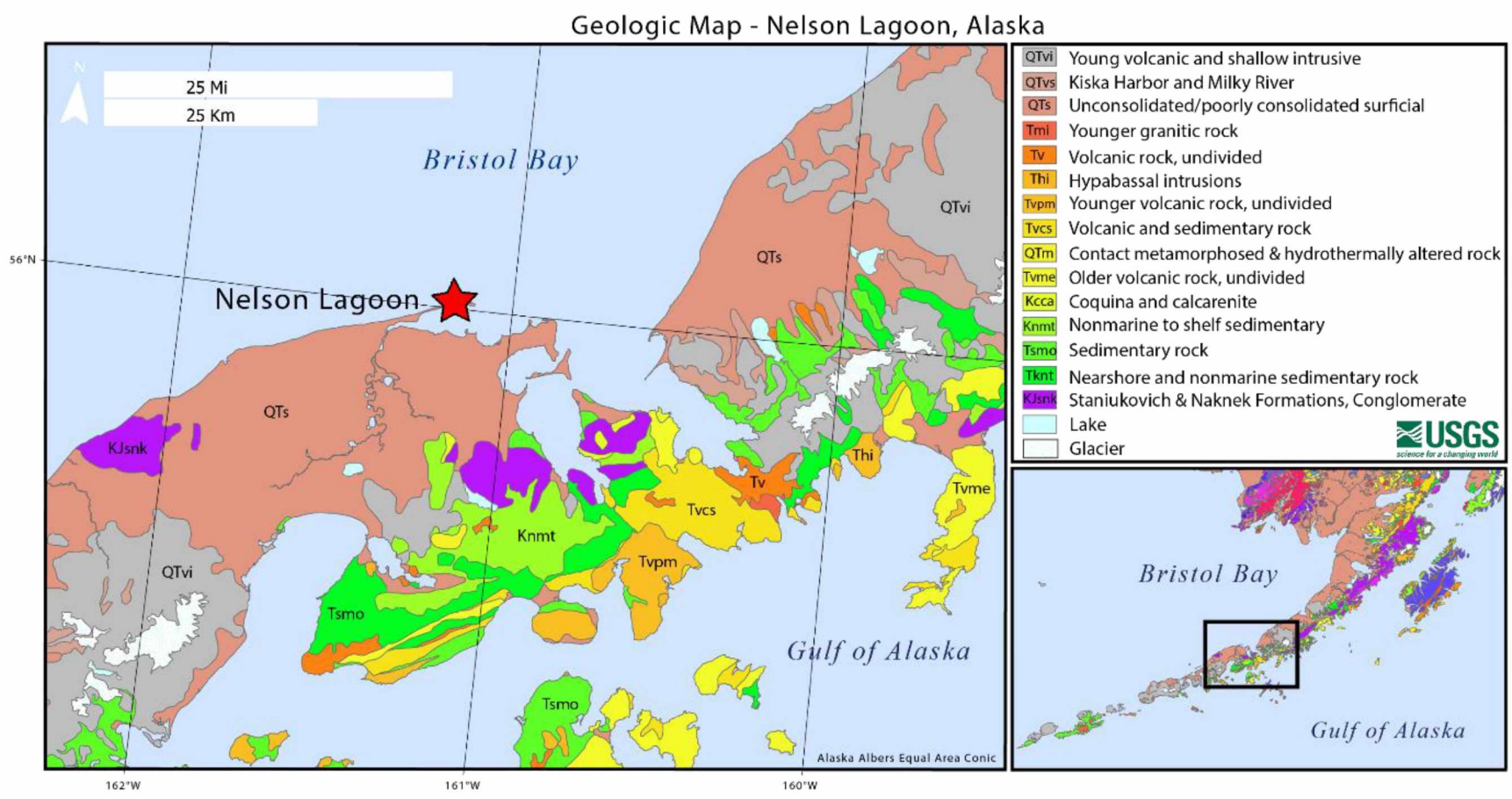

Figure 9. Generalized surficial geology of the Nelson Lagoon area (red star), each color representing a different type or age of rock, from USGS Scientific Investigations Map 3340 - Geologic map of Alaska. (Credit: Frederic Wilson and Keith Labay, USGS. Public domain.)

1.5.3 Oceanographic Setting

Nelson Lagoon is located on a wave dominated coast, with a mesotidal tide regime (**Figure 10**). The lagoon is tidally connected to Herendeen Bay and Port Moller, both of which are large and deep embayments. Nelson Lagoon's energetic wave regime, coupled with its tide range, means that it is a dynamic sedimentary environment. Wave and tidal regimes, as well as sea level fluctuations at Nelson Lagoon, are explored in more detail below.

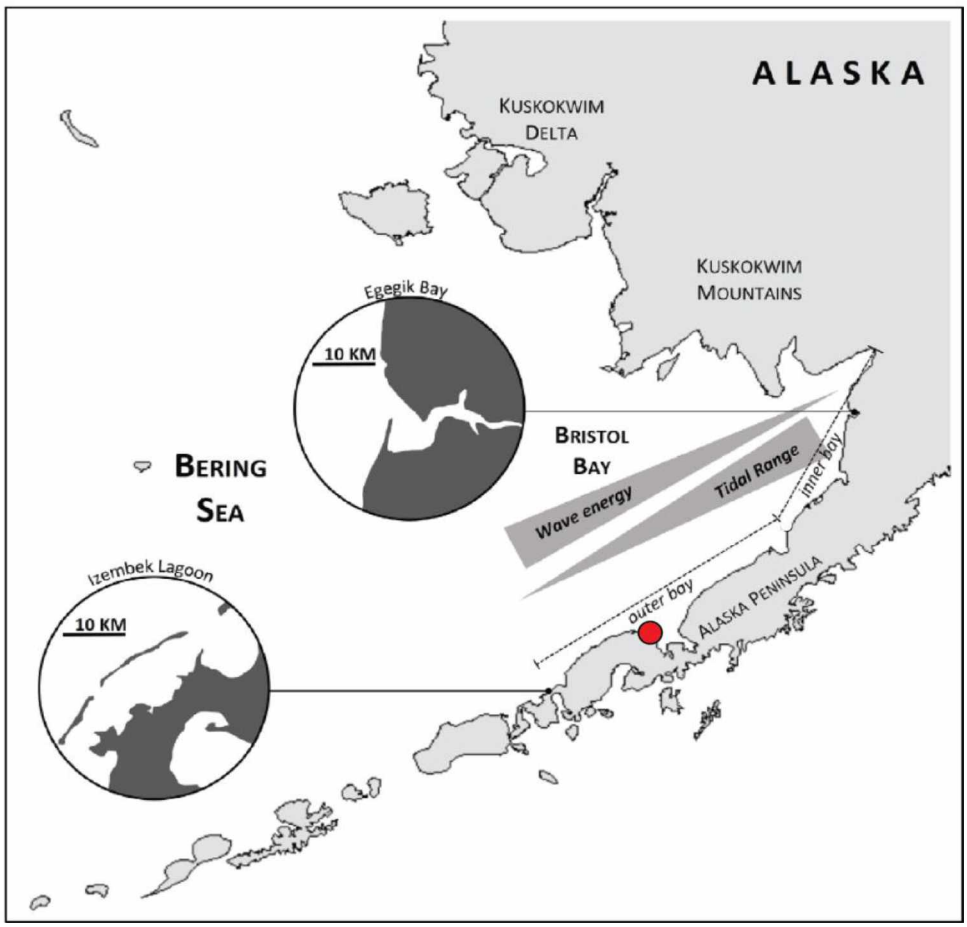

Figure 10. Graphic representation of the relative strength of component marine energy (tide and wave) in Bristol Bay, and the characteristic barrier morphologies in the outer (well-developed barrier islands, such as Izembek Lagoon) and inner bay (barrier spits at embayment mouths, such as Egegik Bay). Nelson Lagoon notated by the red circle (after Kinsman and Gould, 2014).

In 2019, a water level gauge was installed and vertically referenced to a known land-based datum in Nelson Lagoon. Before then, the closest water level gauge with a computed tidal datum was approximately 40 km away in Port Moller, which has been non-operational since 2017 (NOAA, 2020). Tidal datums are calculated from geodetically tied local water level data, which provides

a necessary conversion for storm forecasting and floodplain mapping (Overbeck, 2018). A tidal datum was computed for Nelson Lagoon using data over a 6-month period with JOA Surveys, LLC tidal datum tool (i.e., Spargo et al., 2006) and found that Nelson Lagoon had a great diurnal range of approximately 2.3 m. Various tidal datums were computed and made relative to NAVD88, which allowed for the flooding vulnerability analysis carried out by this project (**Figure 11**).

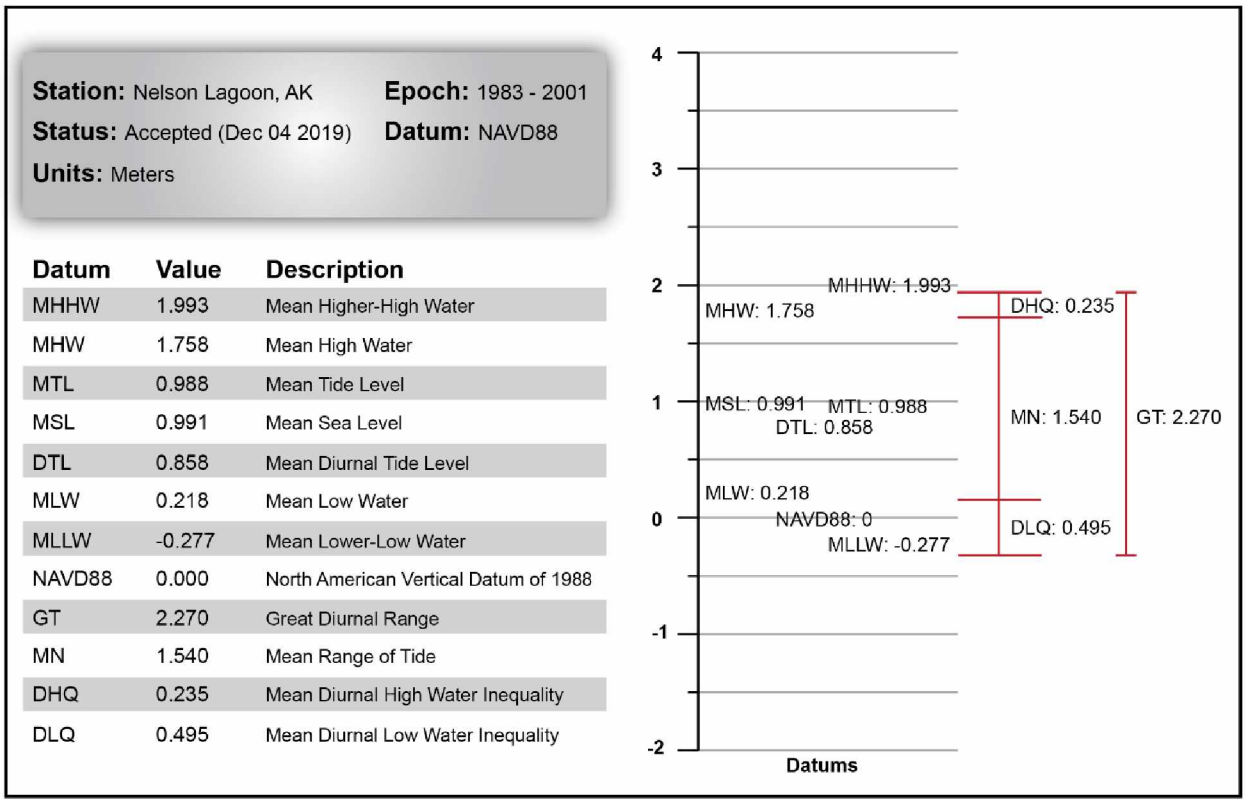

Figure 11. Various tidal datums computed using data over a 6-month period for Nelson Lagoon with JOA Surveys, LLC tidal datum tool. The water level gauge was vertically referenced to a land-based datum (NAVD88).

Due to the geometry of the lagoon as well as discharge from the Bear River, the tidal prism at Nelson Lagoon involves significant ebb currents. HDR Alaska Inc. calculated tidal currents within Nelson Lagoon using a hydrodynamic numerical model. It was found that strong currents occurred particularly within the river channel during incoming and outgoing tides. These currents reach over 2 m/s (HDR, 2014a). However, next to the community it was found that currents were generally slight during all phases of the tide, reaching just over 0.5 m/s.

Nelson Lagoon lacks long-term measured surface wave data. As such, modeled offshore wave data from the Army Corps of Engineers Wave Information Study (WIS) is used to characterize Nelson Lagoon's wave regime (Hubertz, 1992). Specifically, data is compiled from WIS Station 82289 (56.25°, -161.25°). This station is approximately 30 kilometers north north-west of Nelson Lagoon. The dominant wave height directions throughout the year are from the west and west north-west.

There is significant seasonality in the wave regime, with the winter (October – March) experiencing higher variability in both prevailing wave height and direction compared to the summer months (April – September). For example, October, November, and December have the highest occurrence of wave heights >3 meters while June and July have the lowest occurrence of wave heights >1 meter (**Figure 12**). High frequency wind waves <1m in amplitude are propagated across the lagoon during high southerly wind events. HDR Alaska Inc. found that a 100-year return period wind event produces wave heights >1m in deeper, less restricted portions of Nelson Lagoon (HDR, 2014b). Wave heights immediately adjacent to the community reached 0.3 to 0.6 m with the same wind speeds.

1.5.4 Climatological Setting

Temperature data is available from 2010-2020 via the meteorological station at Nelson Lagoon's airstrip (ASOS, 1998). The brevity of this record restricts the amount of long-term variation that can be assessed; however, summer and fall temperatures during these years indicate marked warming. Between 2010 and 2020, the average summer temperature in Nelson Lagoon increased from 8.29°C (2012) to 12.15°C (2016). The three coldest years occurred between 2010 and 2012, and the three warmest years between 2016 and 2020. The average fall temperature in Nelson Lagoon between 2010 and 2020 was 6.73°C. The warmest autumn during this period occurred in 2019, averaging 9.38°C, while the coldest autumn was in 2012, when the average temperature was 4.39°C (**Figure 13**). The three coldest years occurred between 2010 and 2012, and the warmest three falls have occurred between 2016 and 2019. The average temperature during this warm period of 2016-2019 was 7.90°C.

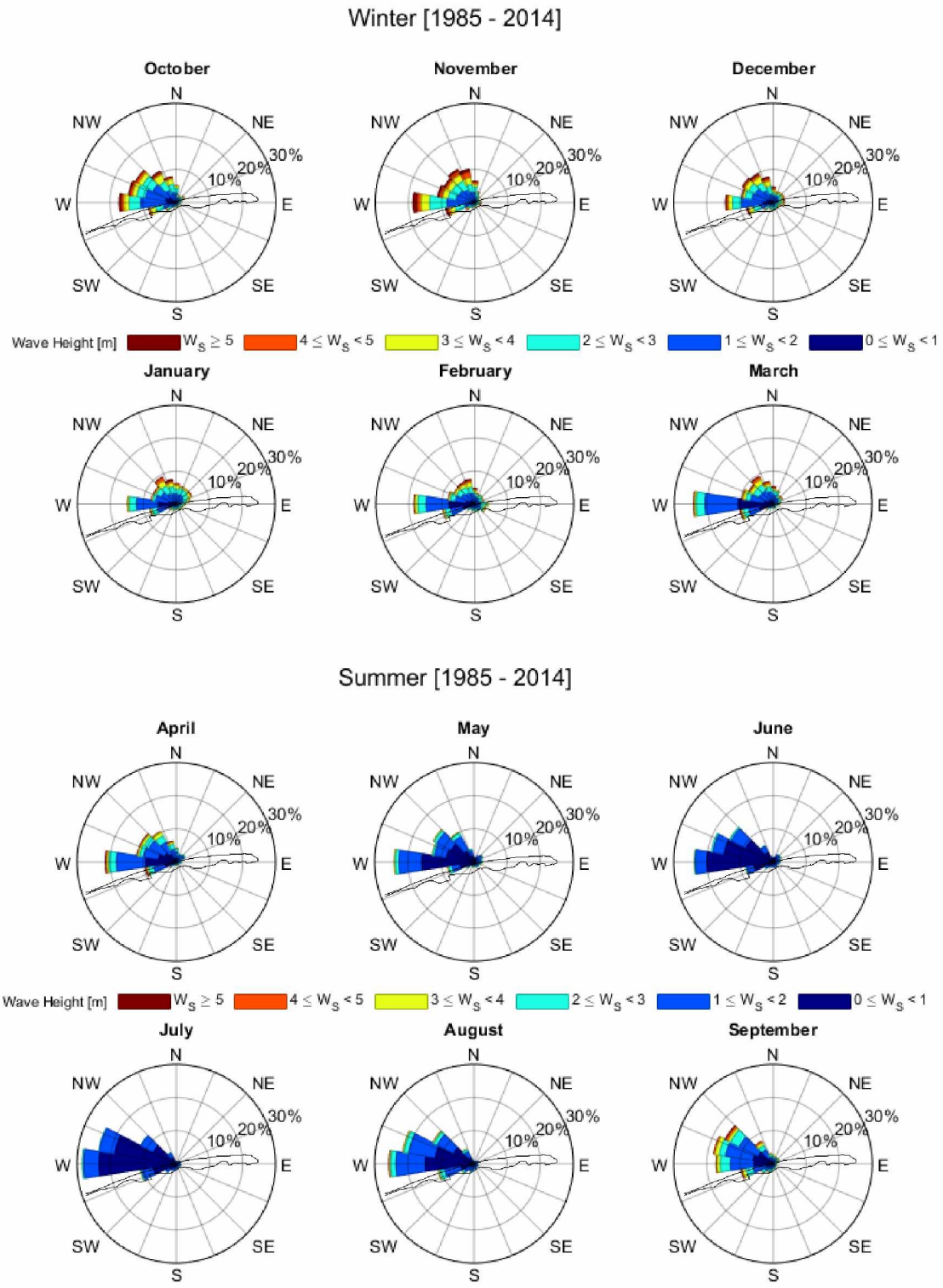

Figure 12. Wave roses for each month averaged over 29 years (1985-2014) from "digital buoy" WIS station 82289 (56.25°, -161.25°). Spokes in each plot point in the compass direction from which waves traveled. Colors within each spoke denote wave height bins and the length of the spokes denote the frequency of occurrence.

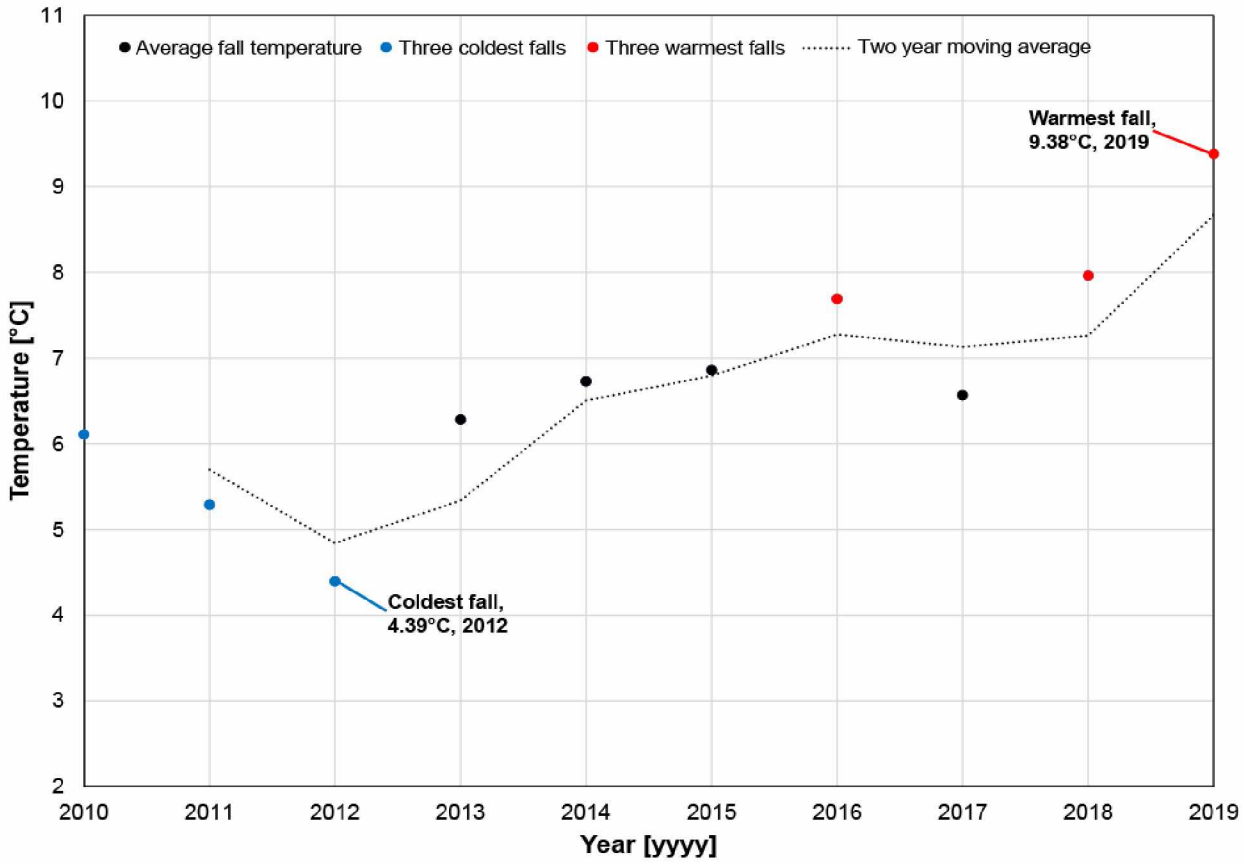

Figure 13. Mean fall temperatures at Nelson Lagoon's airstrip between 2010 and 2019 compiled from the Automated Surface Observing System (ASOS). Temperature averages were calculated from the average of daily temperatures between September 1st and November 30th each year of the timeseries.

Records of wind strength and direction at Nelson Lagoon date back to 2010 and are sourced from the Automated Surface Observing Systems (ASOS) network (ASOS, 1998). The winds in the area are strong, averaging 20 mph, with record maximum speeds >60 mph (Brower et al., 1977). Southerly winds dominate during the summer, while northerly winds are the winter norm. Though, strong winds of gale force may come from any direction, anytime during the year (Mason et al., 1996). Wind speeds >50 mph have been observed during all months of the year (**Figure 14**). Wind speeds >60 mph have been recorded in February, March, April, September, October, and November. Wind speeds >70 mph has been recorded in October and November. In the winter months when wind speeds are highest, the predominant wind direction is from the north and southeast. This has important implications on the wave climate of Nelson Lagoon and, ultimately, the direction of longshore sediment transport (see Chapter 4).

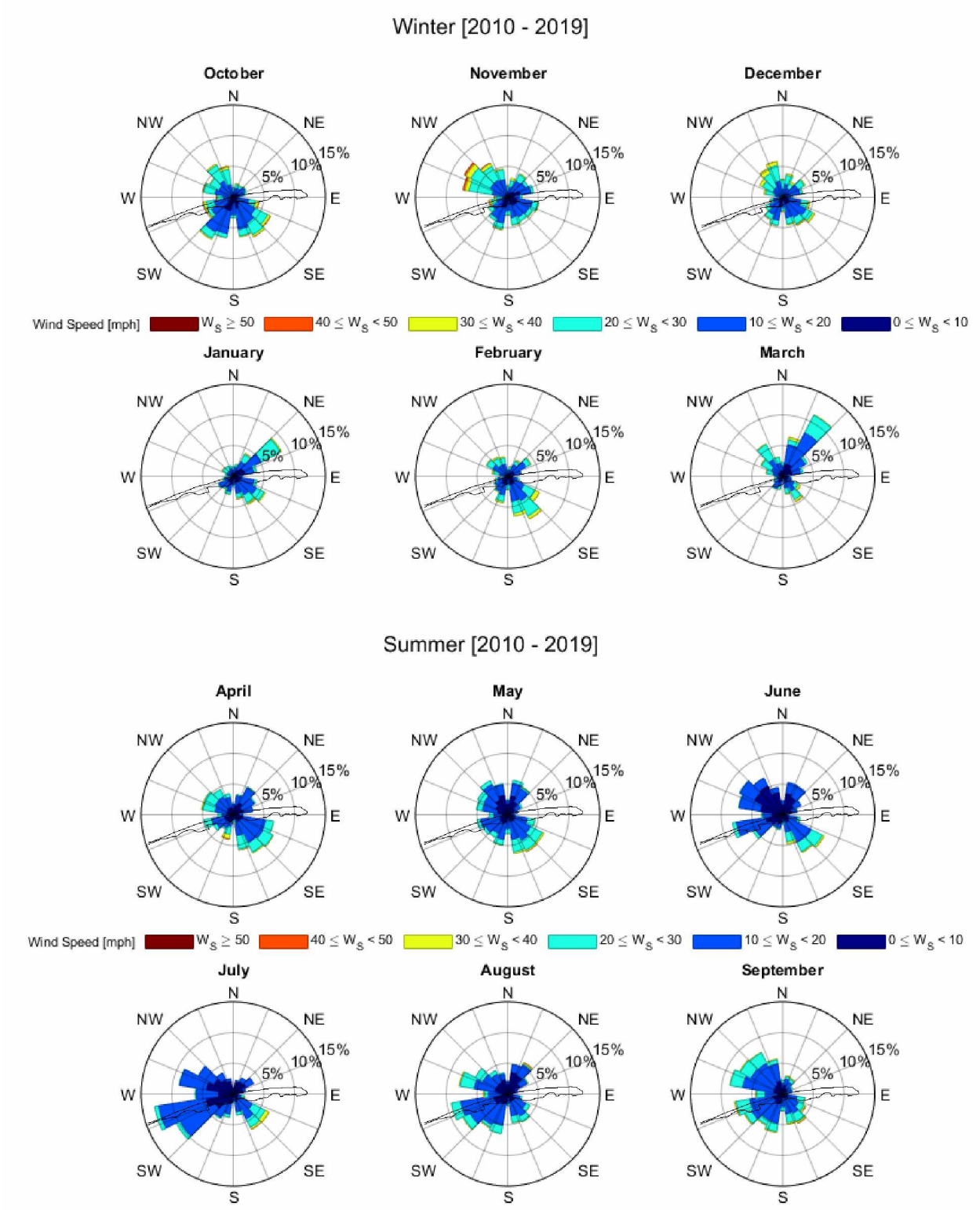

Figure 14. Wind roses for each month averaged over 9 years of observations (2010 - 2019) from the ASOS-integrated meteorological station at the Nelson Lagoon airport. Spokes in each plot point in the compass direction from which winds traveled. Colors within each spoke denote wind speed bins and the length of the spokes denote the frequency of occurrence.

1.6 Previous Work at Nelson Lagoon

Though Nelson Lagoon has been included in a 2019 statewide assessment by the USACE, most of the previous work has been carried out by private engineering firm HDR Alaska, Inc. As per the statewide assessment conducted through a team of scientists and engineers from UAF, USACE, and CRRE, Nelson Lagoon was ranked 58 out of 115 threatened communities in terms of risks associated with erosion and flooding (USACE, 2019). Though, no on-the-ground field work was conducted for the effort and therefore, provided no datasets to build from.

HDR Alaska Inc. was hired by the Aleutians East Borough in 2011 to conduct a Coastal Erosion Study Project at Nelson Lagoon. HDR produced a Historic Shoreline Erosion Map and Analysis, a Beach Profile Study, a Wave Climate Study and a 20% Preliminary Design Report. These reports were funded with qualified outer continental shelf oil and gas revenues by the Coastal Impact Assistance Program, the U.S. Fish and Wildlife Service, and the U.S. Department of the Interior. Most pertinent to this thesis project, HDR collected various cross-shore elevation profiles with RTK-GNSS, conducted a shoreline evolution study using aerial imagery (HDR, 2011; HDR 2014c), and developed hydrodynamic numerical models of waves (HDR, 2014b) and currents (HDR, 2014a) for Nelson Lagoon. Though, the shoreline evolution study conducted by HDR did not systematically quantify rates of change using the USGS Digital Shoreline Analysis System (DSAS) (*section 2.2*), nor were uncertainty values derived as was carried out by this project.

CHAPTER 2

METHODS

2.1 Overview

This study was conducted to assess spatial patterns of vulnerability to erosion and flooding over long- and short-timescales, as well as to identify at-risk infrastructure in Nelson Lagoon. This was accomplished through ground-, water-, and air-based surveys coupled with computer-based processing and analysis using a geographic information system (GIS). Various software packages were utilized including ESRI ArcGIS, Agisoft Metashape, MATLAB R2019B, Microsoft Excel, Trimble Business Center (TBC), RGFGRID, QUICKIN, and Delft3D FM Suite 2019.01 HMWQ. The following subsections describe data acquisition, processing, and analysis.

2.2 Quantifying Patterns of Erosion Vulnerability

2.2.1 Shoreline Change Analysis

To quantify decadal shoreline change the lateral position of shorelines along the Nelson Lagoon spit was delineated using orthorectified aerial imagery spanning approximately 40 years (**Table 1**). Net shoreline changes and weighted linear change rates were calculated using the USGS Digital Shoreline Analysis System (DSAS) by casting cross-shore virtual transects at 25 m intervals with 500 m smoothing over the shorelines from a reference line (referred to as a baseline) (**Figure 15**) (Anders and Byrnes, 1991; Bheeroo et al., 2016; Himmelstoss et al., 2018).

Table 1. Summary of aerial imagery used for shoreline delineation.

Year	Type	Source	Spectral Attributes	Resolution [m^2]
1983	Aerial	NASA AHAP	NIR Composite	2.2
2013	Aerial	Kodiak Mapping Inc.	RGB	0.61
2018	Aerial	UAF ACGL	RGB	0.15
2019	Aerial	UAF ACGL	RGB	0.15

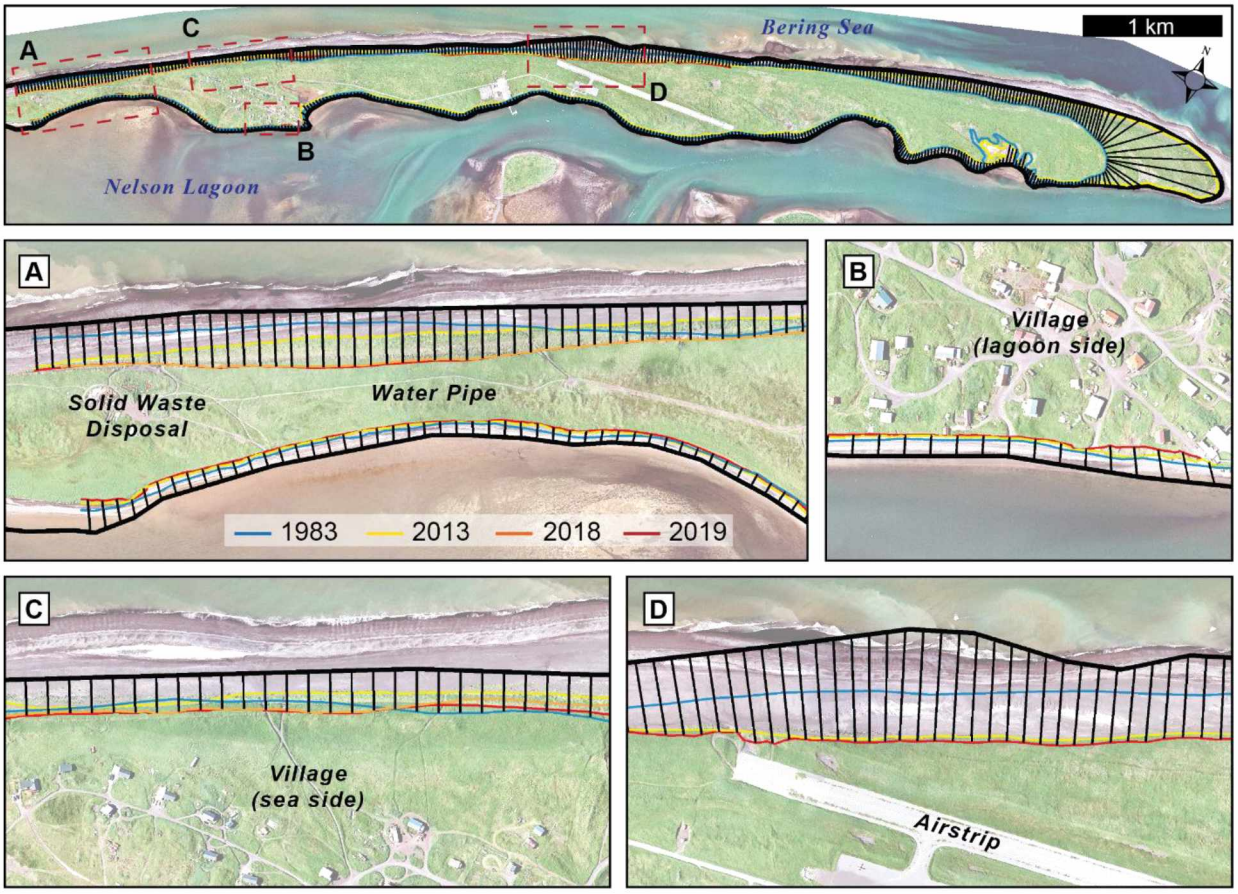

Figure 15. Map displaying the digital transects (thin black line) that were cast from a base line (thick black line) across the digitized shorelines. (A) Insert map showing the solid waste disposal site and main water line, (B) the lagoon-side of the community, (C) the sea-side of the community, and (D) the airstrip. Digital transects are spaced 25 m; a smoothing distance of 500 m has been applied. Data are displayed over an orthoimage collected in 2013 by Kodiak Mapping Inc.

The vegetation line (vegline) was selected as the shoreline indicator because it is easily discernable on the ground and in aerial imagery, and there is no inherent error due to tidal fluctuations and/or swash action as is the case with other potential indicators (Pajak and Leatherman, 2002; Boak and Turner, 2005; Buzard et al., 2020). For example, traditional shoreline erosion studies often compare the position of mean high water, or indicators of high water, over time to determine how quickly and in what direction the shoreline or beach is changing (e.g., Anders and Byrnes, 1991; Ruggiero et al., 2013; da Silva et al., 2016). However, the relationship between the high-water position and erosion is not always straightforward, especially in the case of foredunes (like Nelson Lagoon) since they experience episodic erosion

and recovery. This means that, on a seasonal cycle, the morphology of the beach and even extent of vegetation along the beach can vary. Though, this seasonal effect is mitigated for this project, since all aerial imagery datasets used to delineate the vegline were collected in the summer months (Boak and Turner, 2005; Buzard, 2017).

The average *rate* of change of the area over the 40-year study period was quantified using the weighted linear regression rate-of-change statistic (WLR) computed at each transect along the shoreline (**Eq. 1**). Unlike the linear regression approach this method uses user uncertainty values to give more control to shoreline positions with higher certainty (Genz et al., 2007; Buzard et al., 2020). The weight (w) is defined as a function of the variance in the uncertainty of the measurement (Ut) (Genz et al., 2007):

$$w = 1/Ut^2 \quad [1]$$

The WLR is supported with a 95% confidence interval (WCI) and R-squared value (WR^2) (**Eq. 2**). It is calculated as follows,

$$WR^2 = 1 - \sqrt{\frac{\Sigma(y-y')^2}{\Sigma(y-\bar{y})}} \quad [2]$$

Where y is measured distance from the baseline for a shoreline data point, y' is predicted distance from the baseline based on the equation of the best-fit regression line, and $\bar{y}$ is mean of the measured shoreline distances from the baseline. This WR^2 value quantifies the proportion of the variability in the dependent variable y that is explained by the regression model through the independent variable x.

Total change was calculated using the net shoreline movement (NSM) statistic, which describes the distance between the oldest and most recent shoreline along each transect over the study period (Himmelstoss et al., 2018). Calculating the NSM of each sequential image pair describes the horizontal position change on the smallest temporal scale achievable given available datasets, but, since the sequential image pairs are separated by varying lengths of time (i.e., 1983 to 2013 vs. 2013 to 2018, etc.), the NSM is unable to account for non-linear change (Buzard, 2017; Farquharson et al., 2018). Regardless, NSM is a useful statistic in quantifying the overall extent of lateral change. So, the NSM and WLR for all shorelines were used in tandem to describe the magnitude and linearity of erosion over the study period.

Uncertainty values (U_t) for each shoreline were calculated by the root sum of squares (RSS) of the digitizing uncertainty (U_d), orthorectification uncertainty (U_o), and ground control uncertainty (U_c) (**Table 2**) (e.g., Ruggiero et al., 2013; Kinsman and Gould, 2014; Gibbs and Richmond, 2015; Buzard, 2017). Though, there is not a universal standard in quantifying shoreline change uncertainty (e.g., Crowell, Leatherman, and Buckley, 1993; Ruggiero et al., 2013; Gibbs and Richmond, 2015; Overbeck et al., 2020).

Table 2. Vegline uncertainty values with total uncertainty (U_t) bolded (after Buzard, 2017). Digitizing uncertainty (U_d), orthorectification uncertainty (U_o), and ground control uncertainty (U_c).

Year	U_d (m)	U_o (m)	U_c (m)	U_t (m)
1983	2.20	2.50	0.03	**3.33**
2013	0.61	0.50	0.03	**0.79**
2018	0.15	0.35	0.03	**0.38**
2019	0.15	0.30	0.03	**0.34**

2.2.2 Cross-shore Elevation Profiles

To allow for a more holistic picture of the processes driving the shoreline changes, elevation profiles were collected along cross-shore transects at 30+ locations in 2018 and 2019 (**Figure 16**). This new data builds on the datasets collected by HDR Alaska, Inc. in 2014 and 2015 (HDR, 2015). Precise horizontal and vertical measurements were collected with a GLONASS-enabled GNSS system consisting of dual frequency Trimble R2 and R8s receivers with a TSC3 field controller running Trimble Access software (e.g., Kinsman and DeRaps, 2012; Buzard, 2017). The Trimble R8s receiver served as a mobile base station for the Real-time-Kinematic (RTK) survey, with RTK vectors ranging between approximately 200 and 4,600 m. Both receivers used an elevation mask of 15 degrees.

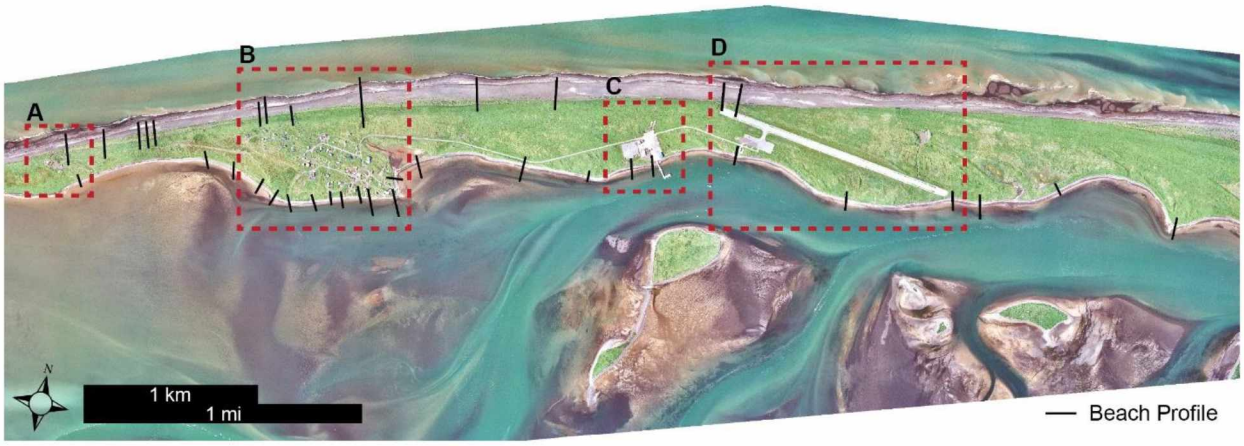

Figure 16. Map showing the location of each cross-shore elevation profile (black line) and community infrastructure (red box). (A) Transfer site, (B) Residential area, (C) Dock and boat storage, (D) Airstrip. Imagery date: 2013. Data are displayed over an orthoimage collected in 2013 by Kodiak Mapping Inc.

Each XYZ coordinate was resolved by averaging 3 epochs over a 3 second occupation period. Average root mean square (RMS) values were approximately 0.03 m (combined horizontal and vertical uncertainty of each point), with average horizontal and vertical precisions being approximately 0.016 m and 0.020 m, respectively (**Table 3**). Sampling density along each transect varied between <1 and 10+ m so that complex features were captured at a representative scale for both small features such as dune geometry and large features such as the broad subtidal shelf.

Table 3. Overview of average RTK vector precision characteristics by survey category. The average: position dilution of precision (PDOP), horizontal precision (P_h) and vertical precision (P_v) reported to the 95% confidence interval, number of satellites (N_{sat}), and vector length (distance from the control point) (ΔX) is given.

Survey	PDOP	P_h (m)	P_v (m)	N_{sat}	ΔX (m)
Ground Control	1.56	0.015	0.019	13.3	1,130
Beach Profiles	1.61	0.016	0.020	13.5	1,292
Other	1.85	0.017	0.022	12.3	1,187
Average	***1.60***	***0.016***	***0.020***	***13.5***	***1,271***

Coordinates from the R8s mobile base station, which were resolved by a 24+ hour occupation static survey, were further refined via the National Geodetic Survey's Online Positioning User Service (OPUS) after subsampling the 1 second observations to 15 second intervals. OPUS is a popular tool which helps survey-grade GPS users tie their local surveys to the National Spatial Reference System and improves raw GPS results via the Continuously Operating Reference Station (CORS) network (Soler et al., 2011). CORS in Port Moller (51 km), Chignik Lake (171 km), and Cold Bay (131 km) were used as control stations for the survey (**Figure 17**). The ellipsoid height of the mobile station was converted to its orthometric height in NAVD88 with an overall RMS of 0.010 m, computed using Alaska Geoid12B (i.e., Elaksher et al., 2018). All point locations in the ground survey campaign were then recalculated in TBC using the OPUS-refined mobile base station coordinate.

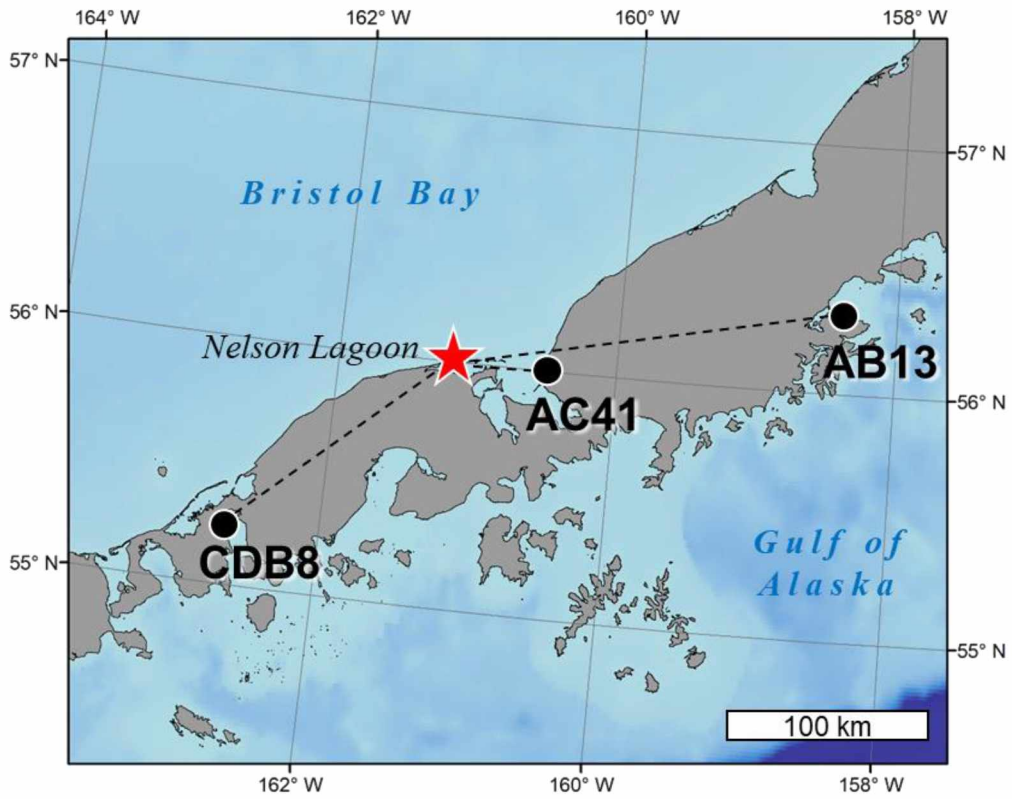

Figure 17. Map showing the location of CORS stations used to refine the base station coordinates. CDB8, Cold Bay; AC41, Port Moller; AB13, Chignik Lake. Nelson Lagoon shown as red star.

2.3 Quantifying Patterns of Flooding Vulnerability

2.3.1 Single-Value Threshold Map

To capture spatial patterns of flooding potential, a high-resolution (<20 cm) digital surface model (DSM) was constructed via Structure-from-Motion (SfM) and vertically adjusted relative to the tidal datum computed for this project (e.g., Tschetter et al., 2014). A Single Value Threshold Map (SVTM) was then produced and color-coded based off the elevation of individual pixels above the water surface. Elevation values were made relative to Mean High Water (MHW) (e.g., Bogardus et al., 2020).

The DSM was derived from roughly 2,400 aerial photographs taken from 100 m altitude with a FC300S camera aboard a DJI Phantom 3 Advanced UAV. The survey, consisting of 9 individual flights, took place over a period of 4 days and was carried out during low tide stages when it was feasible to capture as much of the beach face and mud flats as possible (**Table 4**).

Table 4. Overview of the UAV surveys used to construct the Digital Surface Model (DSM). The name and date of each survey is given with the total number of images acquired (N_{img}), GCPs contained within flight area (N_{GCP}), and tie points within each sparse cloud (N_{tie}). Area of each survey footprint is provided.

Name	Date	N_{img}	N_{GCP}	N_{tie}	Area (km^2)
Flight A	05/02/2019	349	19	492,593	0.135
Flight B	05/05/2019	261	7	1,764,621	0.204
Flight C	05/05/2019	261	13	100,442	0.133
Flight D	05/05/2019	286	10	282,887	0.195
Flight E	05/06/2019	201	15	249,920	0.164
Flight F	05/06/2019	252	9	265,620	0.140
Flight G	05/06/2019	186	10	28,067	0.053
Flight H	05/06/2019	177	7	212,067	0.133
Flight I	05/06/2019	424	18	102,181	0.327
Merged	**-**	***2,397***	***118***	***3,498,398***	***2.350***

The aerial images were aligned into point cloud "chunks" using a photogrammetric software Agisoft Metashape (e.g., Mancini et al, 2013), which aligns images using the Scale-Invariant Feature Transform (SIFT) algorithm (Agisoft LLC, 2019). SIFT is a method that transforms an image into a large collection of feature vectors, each of which is invariant to image translation, scaling, and rotation, though only partially invariant to illumination changes and local geometric distortion (Laporte-Fauret et al., 2019). These preliminary point clouds were processed using an iterative refinement procedure where up to ~20% of the total points within the point cloud are manually omitted based off reprojection uncertainty (~10% of points) and reconstruction accuracy (~10% of points). The positions of all points were re-optimized after each deletion phase, better informing dense cloud generation. The chunks were then merged into a single point cloud based off the 118 ground control points (**Figure 18**).

The resultant dense cloud had an RMS error of 0.32 m (combined horizontal and vertical uncertainty) and an average tie point multiplicity of 4.87, which is the average number of projections for each tie point (Agisoft LLC, 2019).

The survey was accompanied by an extensive ground control campaign using RTK-GNSS (**Figure 17**) (*see section 2.2.2*) to vertically reference the DSM (*see appendix i*) (Watanabe and Kawahara, 2016), relate elevations to the tidal datum computed for this project (Antunes, 2000), but also to validate the vertical accuracy of the refined topographic surface (James et al., 2017).

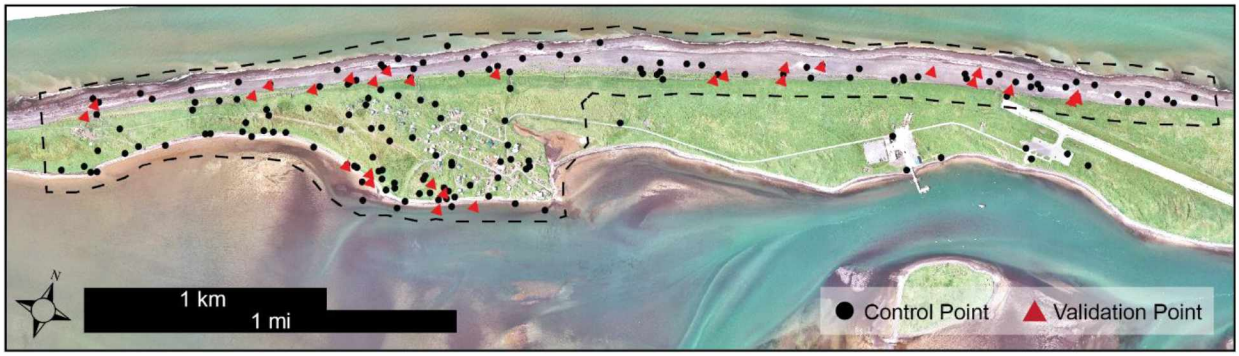

Figure 18. Map showing the locations of control and validation points used to process the UAV-derived DSM. The black dashed line shows the approximate footprint of the survey. Data are displayed over an orthoimage collected in 2013 by Kodiak Mapping Inc.

This validation was carried out following Gindraux et al. (2017), where the vertical values of the unused GCPs from the alignment phase are compared against the refined topographic surface (**Figure 19**). The covariance test showed a high degree of accuracy, with an average Root Mean Square Error (RMSE) of ~0.17 m (n = 30).

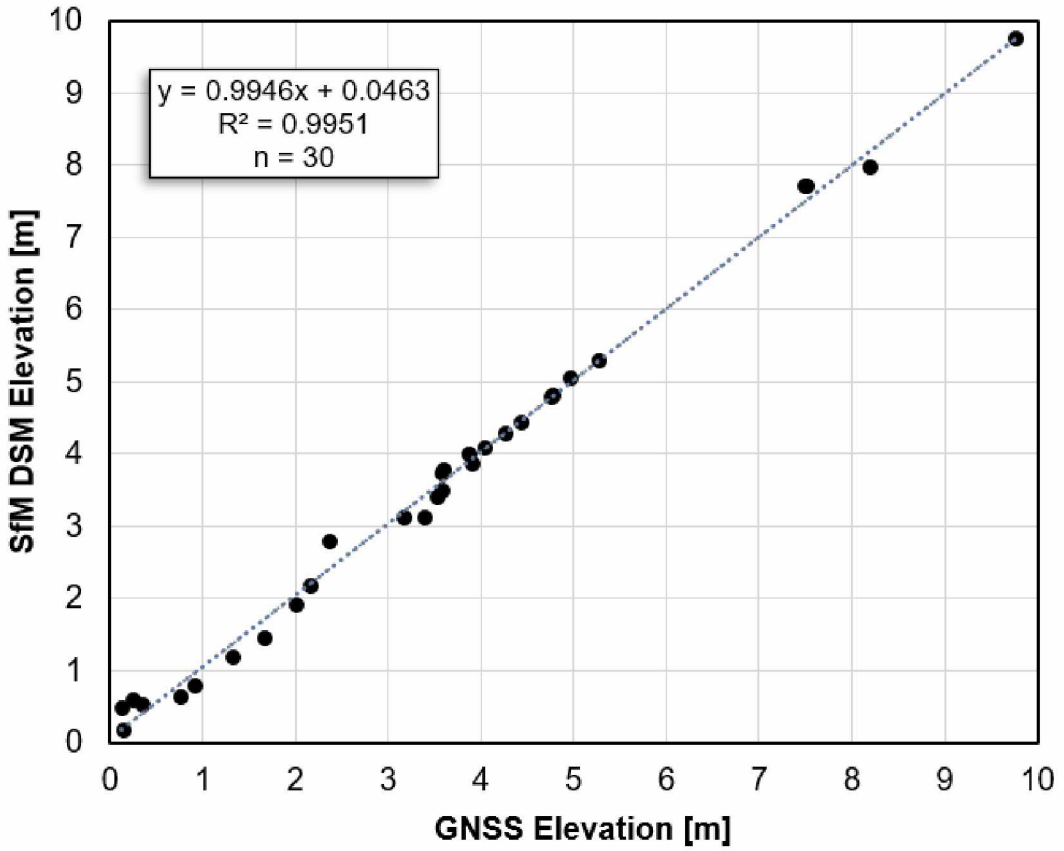

Figure 19. Plot of the covariance between the elevation values of the refined DSM surface (y-axis) and GNSS points used to validate the model (x-axis). RMSE of ~0.17 m (n = 30).

The resultant SVTM provides an effective first-order method for identifying areas vulnerable to flooding based on a static 'bathtub-style' assessment, in that it utilizes single-value water surfaces for each mapped interval (after Kinsman et al., 2013; Tschetter et al., 2014). This simplistic assessment has five main limitations: (1) surge levels are based on empirical estimates, (2) wave setup and run-up factors along the open-ocean coast are not included in computed water levels, (3) intra-storm changes in the foreshore such as dune blowouts are not accounted for, (4) the elevation data follows the height of vegetation, which is particularly an issue on the lagoon-side of the spit most susceptible to flooding, and (5) unrealistic inland 'ponds' of low elevation have not been manually removed. Despite these limitations, the assessment provides a first step in identifying flood-prone sections of the Nelson Lagoon spit and infrastructure susceptible to inundation of varying extents (Kinsman et al., 2013).

2.3.2 Delft3D FM Model

To permit a more accurate assessment of flood vulnerability, beyond that of the SVTM at Nelson Lagoon in the future, this project constructed a regional topobathymetric ("seamless") elevation model from an array of datasets and carried out a simple hydrodynamic simulation using this surface as proof of functionality (i.e., Arnold, 2020). Results were compared with the smaller scale HDR model (*section 3.3.2*). This deliverable will eventually be included in a synoptic scale storm surge model encompassing all of Bristol Bay, in which Nelson Lagoon will be included (*see 4.5*). The proof of functionality was carried out with the Deltares Delft3D-FLOW model (Lesser et al., 2004; Deltares, 2011), a module within the integrated Delft3D Flexible Mesh (FM) suite. The main purpose is the two-dimensional (2D, depth averaged) and three-dimensional (3D) simulation of tidal and wind-driven flow by solving the unsteady shallow water equations in two or three dimensions, although the simulation done for this study was carried out in depth-averaged (2D) mode, which is a valid assumption for well mixed/turbulent water bodies like Nelson Lagoon (Draper et al., 2010; Deltares, 2013). In this approach the vertical momentum equation is reduced to the hydrostatic pressure relation. Vertical accelerations are assumed to be small compared to the gravitational acceleration and are not considered. As such, the momentum equations solved within each computational cell in the x- and y-directions are (Luijendijk, 2001):

$$\frac{\partial u}{\partial t} + u\frac{\partial u}{\partial x} + v\frac{\partial u}{\partial y} + g\frac{\partial \eta}{\partial x} - fv + \frac{\tau_{bx}}{\rho_w(d+\eta)} - \frac{F_x}{\rho_w(d+\eta)} - \nu\left(\frac{\partial^2 u}{\partial x^2} + \frac{\partial^2 u}{\partial y^2}\right) = 0$$

$$\frac{\partial v}{\partial t} + u\frac{\partial v}{\partial x} + v\frac{\partial v}{\partial y} + g\frac{\partial \eta}{\partial x} + fu + \frac{\tau_{by}}{\rho_w(d+\eta)} - \frac{F_y}{\rho_w(d+\eta)} - \nu\left(\frac{\partial^2 v}{\partial x^2} + \frac{\partial^2 v}{\partial y^2}\right) = 0$$

(1) (2) (3) (4) (5) (6) (7) (8)

in which:

d	= water depth below plane of reference(m)
f	= Coriolis parameter (1/s)
$F_{x,y}$	= x- and y-component of external forces (N/m^2)
u,v	= depth averaged velocity (m/s)
U	= absolute magnitude of total velocity, $U=(u^2+v^2)^{1/2}$; (m/s)
ρ_w	= mass density of water (kg/m^3)
ν	= diffusion coefficient (eddy viscosity); (m^2/s)
η	= water level variation above plane of reference (m)
g	= gravity of acceleration (m/s^2)
$\tau_{bx,y}$	= x- and y-component of the bed shear stress (N/m^2)

The formulas consist of (1) velocity gradients, (2)(3) advective terms, (4) barotropic pressure gradients, (5) Coriolis force, (6) bottom stress, (7) external forces (wind), and (8) viscosity.

D-FLOW is suited with a flooding and drying algorithm where grid cells are activated when water levels exceed a flooding threshold, while grid cells are de-activated when local water levels drop below half of this threshold (Deltares, 2012). A large advantage of using Delft3D FM over its predecessor (Delft3D 4.0) is the implementation of a coordinate system. Grid features in the FM suite are coordinate based, instead of grid administration based. This allows for quick adaptations of the grid without the time-consuming task of updating all definitions of boundaries, cross-sections, and observation points. These are defined by their position in the used coordinate system and not linked to specific grid points (Laan, 2019).

2.3.2.1 Seamless Elevation Model

The seamless elevation model was constructed by combining ship-based single-beam surveys, digitized t-sheets, delineated satellite imagery, sea-surface satellite altimetry, as well as IfSAR-derived topography (**Table 5**) (i.e., Gesch and Wilson, 2001). A bathymetric survey was also carried out during the field work campaign in May 2019 (*see NLG19*). NLG19 was collected with a Seafloor HydroLite SONAR depth finder integrated with the GNSS equipment (*see section 2.2.2*). The survey targeted areas proximal to community infrastructure (docks, residences, fishing cabins, etc.) as well as sections of river and tidal channels where data gaps existed. This survey added to HDR Inc.'s survey of the primary river channel that runs along the south side of the Nelson Lagoon spit (**Figure 1**). For the nearshore region fronting Nelson Lagoon and Port Moller, a total of 10 ship-based NOAA surveys collected between 1955 and 1960 were compiled from NOAA's Bathymetric Viewer web interface (NOAA, 2020). Likewise, a 1:80,000 scale NOAA T-Chart was used to derive bathymetry within Herendeen Bay and Port Moller. All bathymetric datasets (besides ETOPO1) were corrected for tidal related variations in water level using Port Moller station (Station ID: 9463502) and made relative to MLLW. The deepest waters within the model's domain made use of NOAA's ETOPO1 dataset, which has a resolution of 1 km^2 (Amante and Eakins, 2009). ETOPO1 was not made relative to any datum, as its uncertainty is larger than the entire tidal range at Nelson Lagoon and Port Moller and is why its use was restricted to waters deeper than 50 m.

Table 5. Overview of the compiled datasets/surveys used to construct the seamless elevation model upon which the computational grid was derived. Data is organized by geography. The survey, year of acquisition, source, number of XYZ points (N_{xyz}), average sampling density (S_{dens}), and depth/elevation range (R_z) is provided.

Survey	Year	Source	N_{xyz}	S_{dens} (per km^2)	Rz (m)
Topography					
IfSAR DTM	2018	USGS	2,095,934	40,000	12
Offshore					
ETOPO1	2009	NOAA	432	1.0	60
Nearshore					
H08537	1960	NOAA	6,347	75.6	24
H08488	1959	NOAA	7,008	3.5	65
H08487	1959	NOAA	8,573	38.3	37
H08486	1959	NOAA	10,492	35.0	40
H08485	1959	NOAA	12,455	42.9	42
H08434	1958	NOAA	4,183	3.2	55
H08433	1958	NOAA	8,626	47.9	37
H08432	1958	NOAA	10,151	44.1	42
H08224	1955	NOAA	18,839	78.5	24
H08223	1955	NOAA	6,203	5.0	50
Nelson Lagoon					
NLG19	2019	This project	15,947	1,993.4	13
Man. Interp.	2014	This project	6,857	67.9	1
Herendeen Bay / Port Moller					
TChart16363	2019	NOAA	1,169	3.5	104
Bear River					
HDR13	2013	HDR Inc.	36,873	6,704.2	11
Total	**-**	**-**	***2,250,089***	**-**	***120***

The 0 m isobath along the Nelson Lagoon spit, islands, and Herendeen Bay and Port Moller shoreline, was extracted from satellite data (SPOT-7) after querying the tidal stage captured by the imagery with RTK-GNSS elevations of the water surface (i.e., Kelly and Gontz, 2018). Above 0 m elevation, USGS' 5 m^2 IfSAR derived DTM was used, restricted to the backshore regions within the domain lower than ~20 m in elevation. Elevation values from every pixel of the DTM within the domain were sampled, resulting in roughly 2 million XYZ points.

The combined dataset contains roughly 2.3 million XYZ points, spanning approximately 120 m in elevation (**Figure 20**). Since datasets were integrated, spanning 60+ years, the sampling density varies widely across the domain, the lowest being ETOPO1 (1 per km^2) and the highest being the IfSAR DTM (40,000 per km^2). Though, ultimately, the resolution of the elevation surface is dictated by the cell size of the computational grid, discussed below (*see 2.3.2.2*). For visualization purposes, a triangular irregular network (TIN), a form of vector-based digital geographic data, was produced from the 2.3 million points.

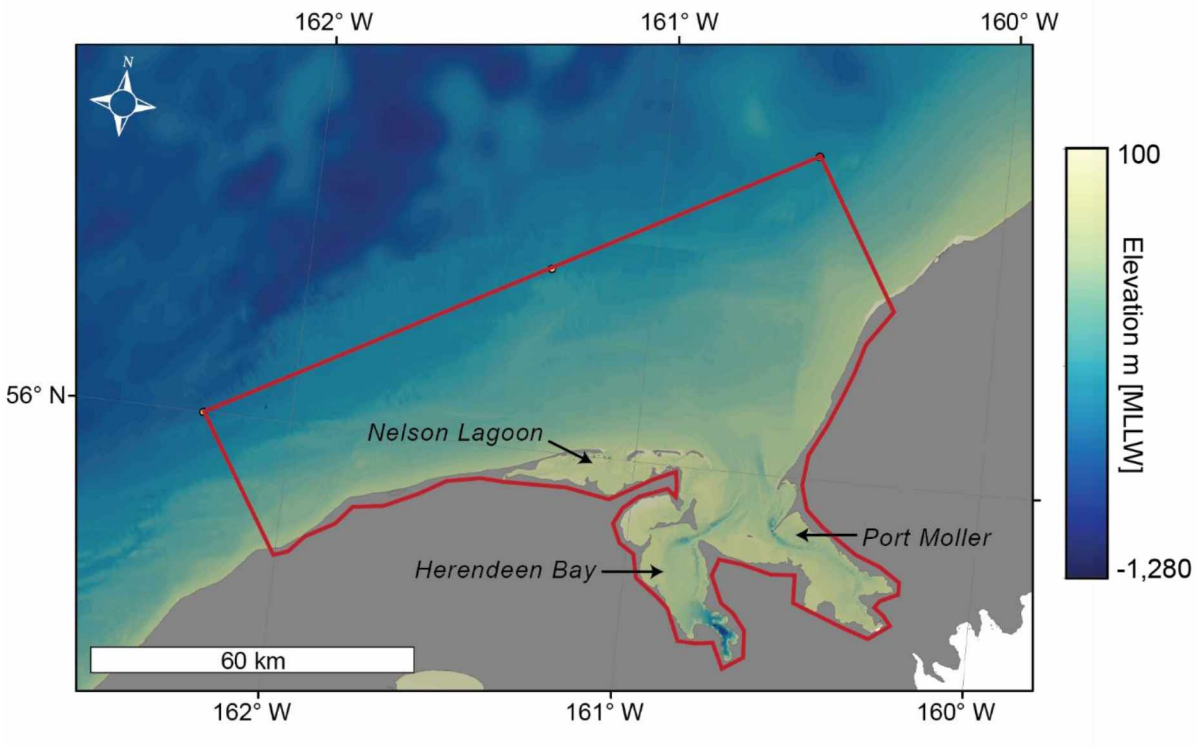

Figure 20. Map showing the D-FLOW model domain (red line) and bathymetry. Nelson Lagoon, Herendeen Bay, and Port Moller is noted by the black arrows.

While the combined bathymetry (<0 m) was not validated because of travel restrictions in 2020, the topographic (>0 m) surface's accuracy was tested in the same manner as the UAV derived DSM (*see 2.3.1*), following Gindraux et al. (2017). A total of 80 RTK-GNSS points located in relatively stable areas (landward of the incipient dune) on both sides of the Nelson Lagoon spit were compared against the values of the IfSAR DTM pixels in which each validation point fell (**Figure 21**). Though, it is important to note that vertical inconsistencies are inevitable, given that the DTM's 5 m^2 pixels represent a single elevation value, averaged over the 5 m^2 pixel area. As such, high gradient areas of the DTM are most affected by this source of error. Regardless, such a covariance test provides a good first-order test of vertical accuracy. The test showed an acceptable degree of covariance, with an RMSE of 0.56 m (n=80).

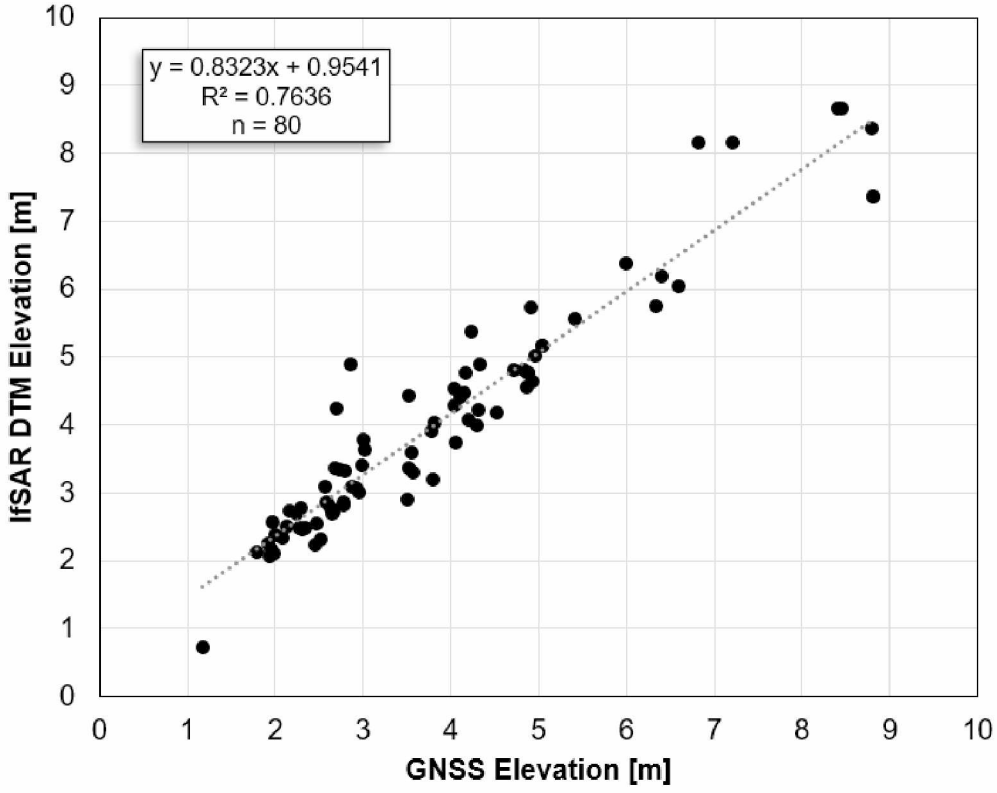

Figure 21. Plot of the covariance between the elevation values of the IfSAR DTM surface (y-axis) and GNSS points used to validate the model (x-axis). RMSE of 0.56 m (n = 80).

Another important caveat to this covariance test is that only the area of the DTM where RTK-GNSS data was collected is represented in the test. Though, the vertical accuracy of the DTM is most important around infrastructure (assessing vulnerability to flooding) which is where the GNSS survey was carried out.

2.3.2.2 Model Set up

Given the seamless elevation model described above, a computational grid was derived using RGFGRID and QUICKIN, two pre-processing programs within the Delft3D suite.

RGFGRID was used to create, manipulate, and visualize an orthogonal grid for the D-FLOW run described below, which is an ordered set of horizontal coordinates, at the locations of the depth points (Luijendijk, 2001). When constructing a grid several restrictions of a numerical nature must be considered: (1) grid lines must intersect perpendicularly, and (2) grid spacing must vary smoothly (M- and N-smoothness). The orthogonality is the extent to which a cell resembles a square. It should be kept low (< 0.04) as the error in the D-FLOW cross advection term is proportional to this value. The M and N smoothness refers the ratio between adjacent grid cell lengths. A maximum factor of 1.3 to 1.4 is advised to minimize errors in finite difference operators. The grid constructed for this thesis had a smoothness of 1.002 and an orthogonality of 0.010. Once the orthogonal grid was generated, QUICKIN was used to interpolate a surface from the seamless elevation model (*see 2.3.2.1*) and, from the interpolated surface, tie a depth value to each cell of the grid produced via RGFGRID (**Figure 22**).

The event chosen to simulate tides and flow over the produced bathymetry and grid was the November 11, 2011 Bering Sea storm (Kinsman and DeRaps, 2012; Terenzi et al., 2014), since it resulted in the largest storm-tide water residual (observed water level minus predicted) recorded at the Port Moller tidal station (NOAA, 2020). Specifically, a simulation of water levels between 11/11/2011 0:00 and 11/13/2011 0:00 was carried out with 30 second timesteps. The model was forced with time varying wind fields from the ASOS-integrated meteorological station at the Nelson Lagoon airstrip and water level fluctuations from the Port Moller tide station at the open ocean boundaries. Fluvial input was not considered.

Most physical and numerical parameters were kept default (**Table 6**) since the goal of this component of the thesis was to assess the functionality of the input morphology (topobathymetric model) (i.e., Arnold, 2020). A sensitivity analysis using various environmental conditions was not performed, as a synoptic scale surge model will be built using the input surfaces produced by this thesis (*see 4.4*). Though, results were qualitatively assessed against HDR's smaller scale flow model using MIKE (*section 3.3.2*).

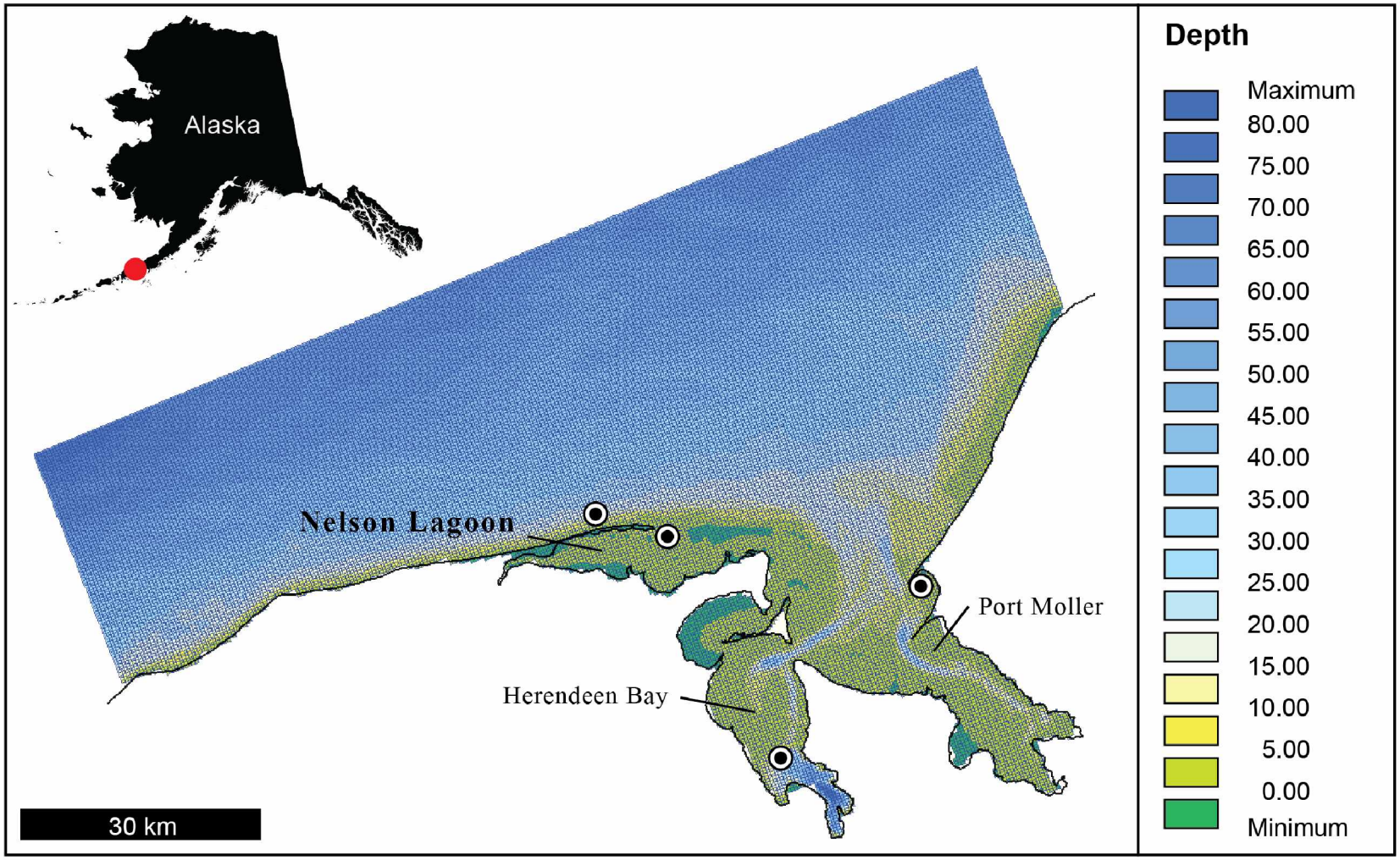

Figure 22. Map showing the bathymetry of the Nelson Lagoon area on a structured Delft3D grid. The locations of output observation points are shown as white and black dots.

Table 6. The parameter settings of the D-FLOW run.

Parameter	Value	Unit
Latitude	56	°
Time step	30	s
Gravity	9.813	m/s^2
Water density	1,000	kg/m^3
Air density	1.205	kg/m^3
Temperature	6.0	°C
Salinity	30	ppm
Bottom roughness Manning (uniform)	0.023	-
Horizontal eddy viscosity	1.0	m^2/s
Threshold depth	0.001	m
Max Courant Number	0.7	-

Observation points with which to query variable outputs, were placed at four separate locations within the model domain (Nelson Lagoon spit, Nelson Lagoon mouth, Port Moller, and Herendeen Bay) (**Figure 22**).

2.4 Assessing At-risk Infrastructure

To assess the implications of the analyses described above, infrastructure datalayers from the Alaska Division of Community and Regional Affairs (DCRA) were compiled from AutoCAD and converted to an ESRI geodatabase (AK DGGS, Personal Communication) (**Figure 6**). Information about the type and purpose of each structure in Nelson Lagoon is included and allows for a practical assessment of coastal hazards and their immediate risk to community resources. Coupling project results (Chapter 3) with these infrastructure data serve as invaluable deliverables (Smith, 2014).

Infrastructure vulnerable to erosion was identified and categorized by extrapolating the most recent shoreline across a given shoreline section at 10-year intervals using the average WLR rate of that section (*see section 3.2*). There is an assumption of linearity made in this type of analysis and is discussed further in section 4.2.1. Infrastructure vulnerable to flooding was identified and categorized by which flood height interval a given structure fell within the SVTM. This type of analysis assumes that an area with an elevation less than a projected flood level will be flooded like a "bathtub." This is discussed in section 4.2.1.

CHAPTER 3

RESULTS

3.1 Overview

The following subsections display and describe results from the community erosion and flooding vulnerability assessment. Measurements of coastal change are coupled with infrastructure data layers to quantify the overall risk to the community's buildings and utilities, and project future risks with an assumption of linearity in shoreline change rates. A subsample of the plotted cross-shore elevation profiles from representative sections of the shoreline are presented and discussed. The complete dataset can be found in appendix ii.

3.2 Patterns of Erosion Vulnerability

As discussed in section 2.2.1, the shoreline change analysis tracked purely lateral changes in the position of the shoreline through time. As such, results from this analysis are supplemented with the cross-shore elevation profiles, allowing for a more holistic picture to be assembled of the morphodynamic process driving the detected changes. The analysis revealed that the Nelson Lagoon spit narrowed between 1983 and 2019, with an average NSM of -16.9 m (both sides, terminus of the spit not included); however, this value showed variability above the average (σ = 21.9 m), and the lagoon and seaward sides of the spit exhibited different erosional regimes (**Figure 23**). The spit also elongated by more than 800 m between 1983 and 2013. These findings render averaged shoreline changes extremely misleading. Given this spatial variability, the results of the historic shoreline change analysis have been split up into four shoreline sections based on their proximity to infrastructure: A) the solid waste disposal site, B) the lagoon-side of the community, C) the sea-side of the community, and D) the airstrip (**Table 7**). This section documents the results of the erosion vulnerability assessment, with an emphasis placed on identifying infrastructure at risk of erosion over spatiotemporal scales relevant to community planning; the long term morphodynamic evolution of the entire spit is discussed in Chapter 4.

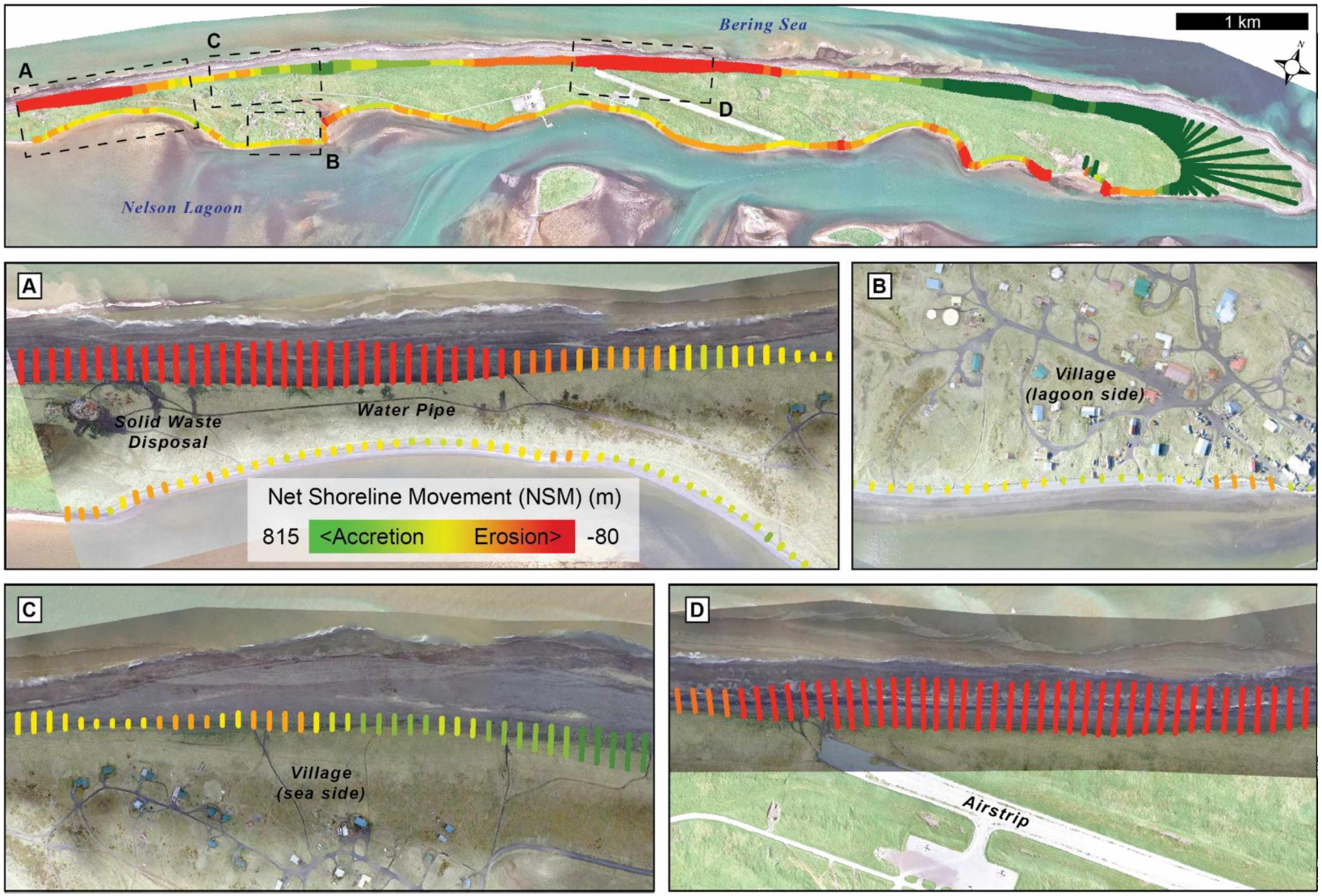

Figure 23. Map showing the Net Shoreline Movement (NSM) between 1983 and 2019 as computed by the historic shoreline change assessment. The top panel displays the entire spit; letters correspond to each inset map.

Table 7. Average shoreline change analysis results by shoreline section. Net shoreline movement (NSM) and Weighted Linear Regression (WLR) rate is provided. Refer to figure 22 for the extent of each section; letters correspond to each inset map.

Section	NSM (m)	WLR (m/yr)	WCI (m/yr)	WR2
A – Solid Waste Disposal	-29.6	-0.98	2.72	0.71
B – Community (lagoon-side)	-6.30	-0.19	1.25	0.76
C – Community (sea-side)	2.31	-0.06	3.01	0.18
D – Airstrip	-55.8	-1.53	2.52	0.98

Section A – The shoreline fronting the solid waste disposal site showed among the highest average NSM across the spit, with a value of -29.6 m. The lagoon shoreline along this section observed significantly less change when compared to the seaward coastline (-7.6 m as opposed to -48.6 m avg. NSM). The average WLR across section A came out to -0.98 ± 0.36 m/yr (90% confidence; WR2 = 0.71). Using this rate to extrapolate the position of the shoreline shows that both the road and solid waste disposal site is at risk of erosion (**Figure 24**). In fact, the solid waste disposal site has been flooded by storms from the seaward side multiple times in recent years (discussed further in section 4.4). Of most concern is the main water line that runs across this portion of the spit, though its exact position is unknown (CE2, 2002).

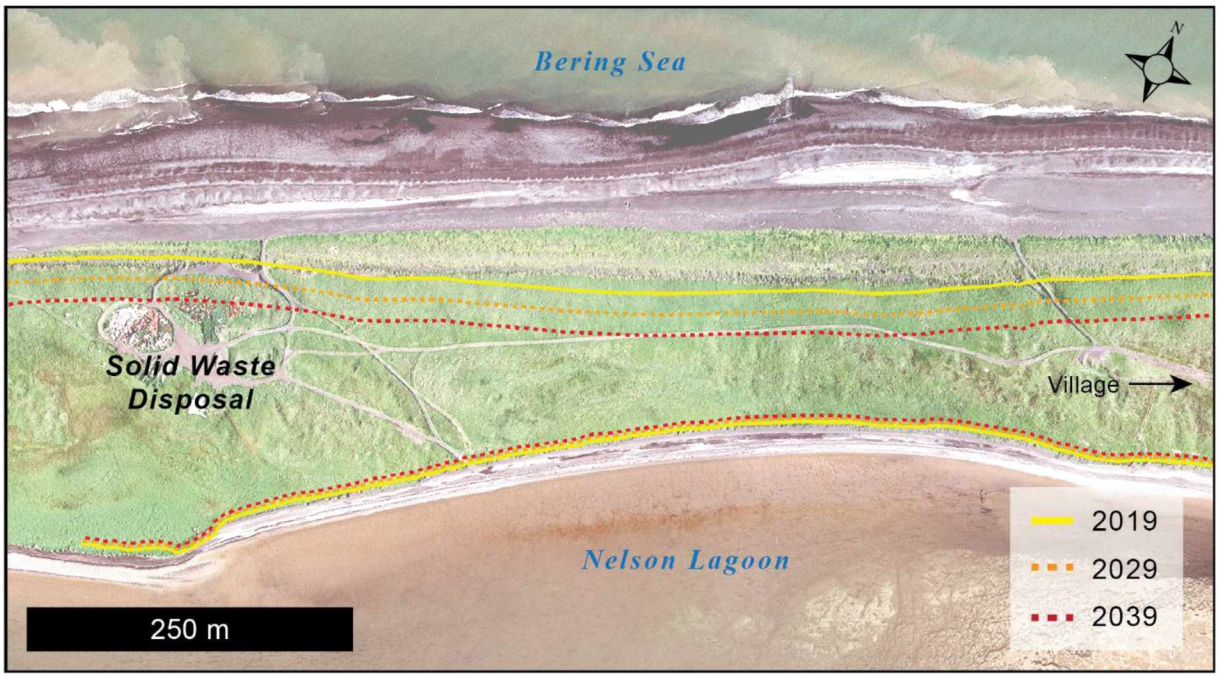

Figure 24. Map showing the projected shoreline positions (2029 and 2039) across section A from the 2019 shoreline. Notice that the road and solid waste disposal site is at risk of erosion.

The cross-shore elevation profiles along this section were taken in 2018 and 2019, and reveal wave undercutting and slumping of the incipient dune face (**Figure 25**). The *slope* of the dune face steepened, coinciding with its landward retreat due to surge and wave action. This process was captured during a site visit in 2018 and is discussed further in section 4.4.

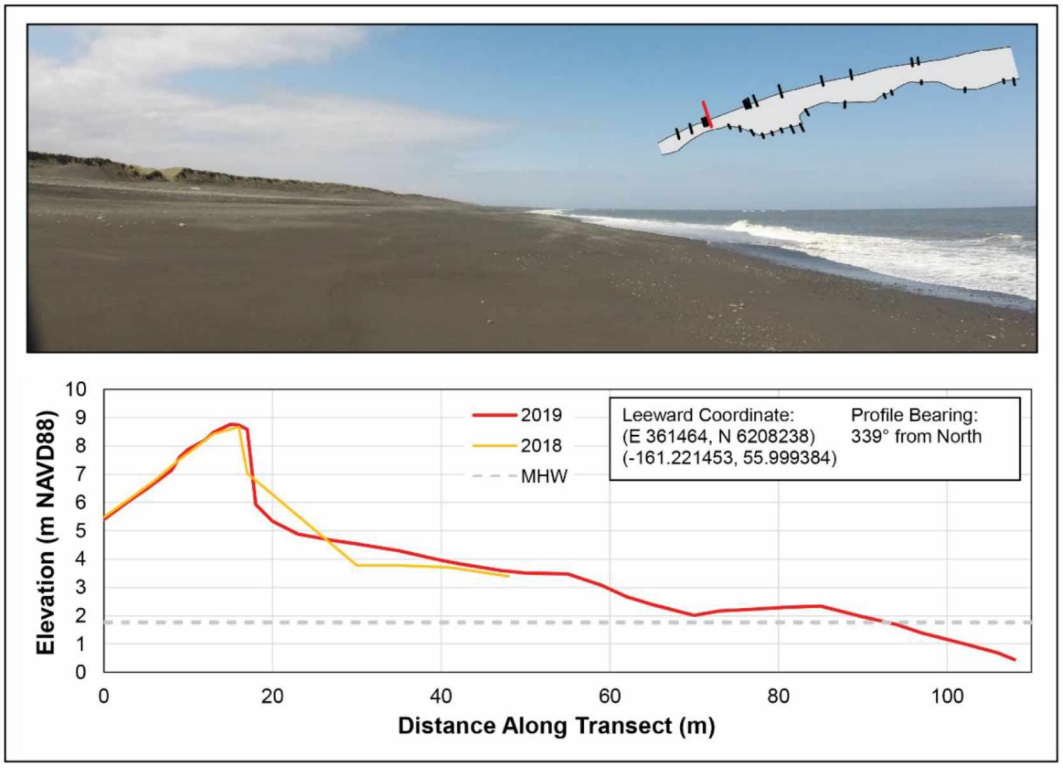

Figure 25. Cross-shore elevation profiles from 2018 and 2019 within section A. Notice the under-cutting of the dune face.

Section B – The lagoon-side of the community, which is the area of highest concern for residents, showed relatively smaller rates of change when compared to section A or D, but the proximity of the shoreline across section B is much closer to residential and commercial infrastructure (**Figure 26**). In fact, some buildings along this reach have already been undercut by wave action and abandoned. The average NSM was -6.30 m between 1983 and 2019, with a WLR of -0.19 ± 0.10 m/yr (90% confidence; WR2 = 0.76). Multiple buildings are intersected by the projected shoreline positions (*see 3.4*). The cross-shore elevation profiles along this section were taken in 2014, 2015, and 2019, and reveal the beach slope has decreased through time as the dune face retreats landward (**Figure 27**).

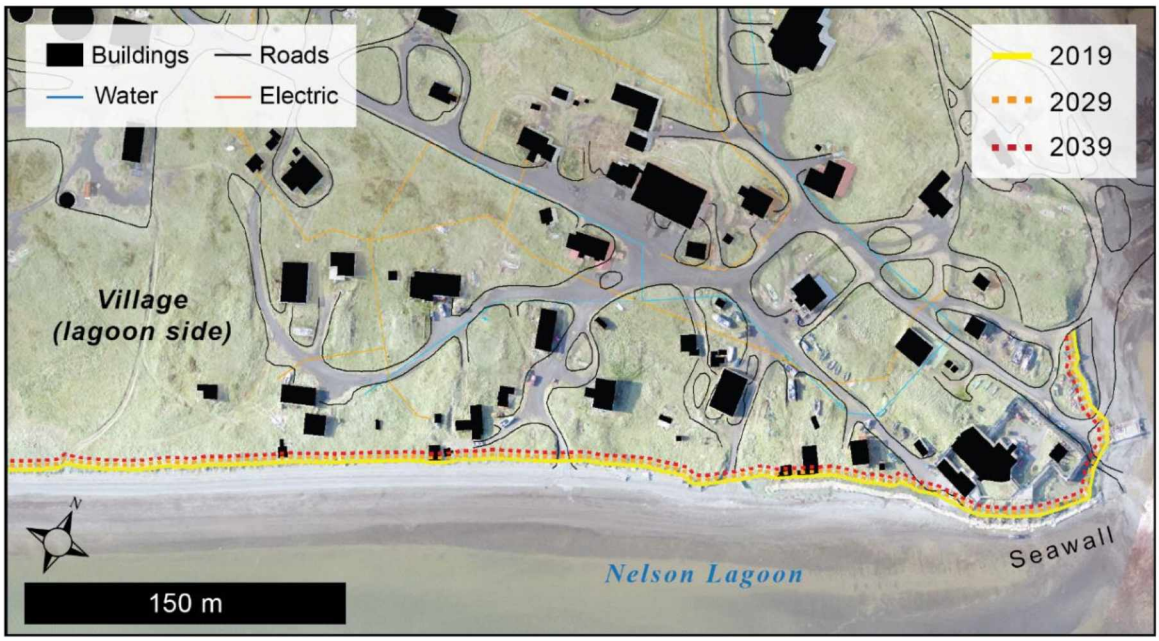

Figure 26. Map showing the projected shoreline positions (2029 and 2039) across section B from the 2019 shoreline. Projected shorelines intersect multiple buildings along the coast.

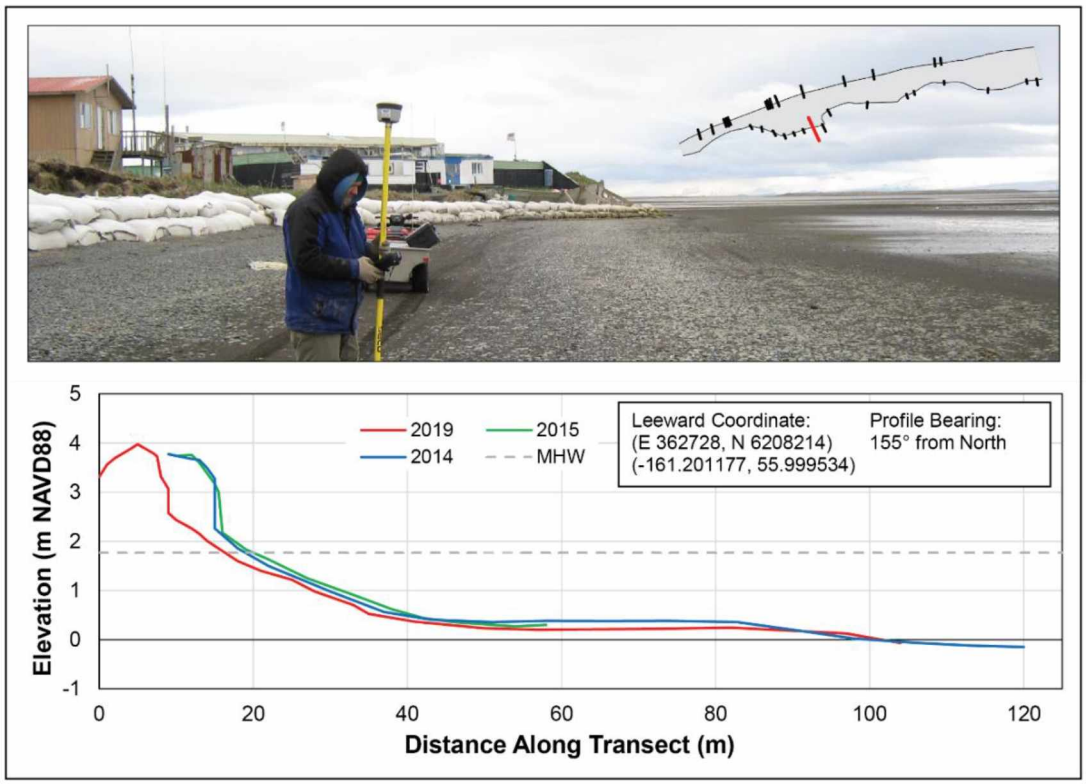

Figure 27. Cross-shore elevation profiles from 2014, 2015, 2018, and 2019 within section B. Notice how the slope of the beach face has decreased while the dune face has retreated landward.

Section C – The shoreline fronting the sea-side of the community is the only shoreline among the four sections that observed a positive average NSM between 1983 and 2019 (+2.31 m), with a negligible WLR. Though, this section is abutted by highly erosional stretches of coastline. Given such a low WLR, the projected shoreline positions show minimal changes to the shoreline positions over the next few decades (**Figure 28**). The cross-shore elevation profiles along this section were taken in 2018 and 2019 and show that storm berms were deposited along this reach in 2019 (**Figure 29**). The differences between the two profiles appear to be seasonally driven, with the 2018 (2019) profile representing a typical winter (summer) beach configurarion, although the position of the bluff face and crest did not migrate laterally between the two years.

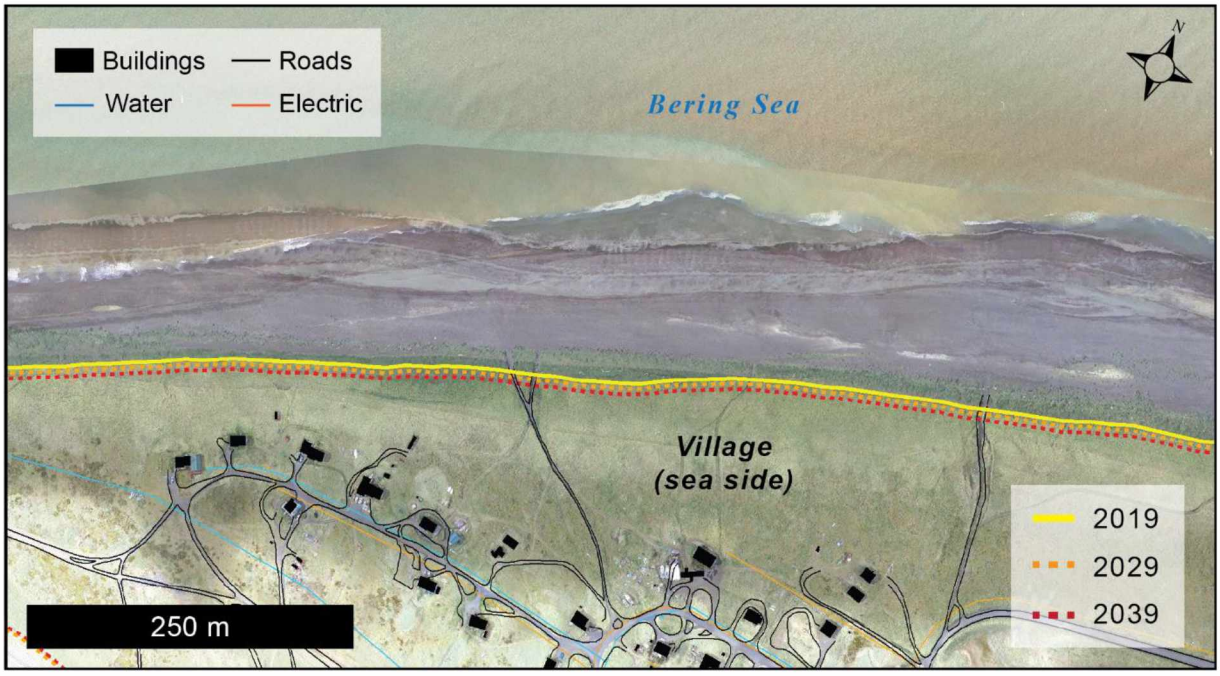

Figure 28. Map showing the projected shoreline positions (2029 and 2039) across section C from the 2019 shoreline.

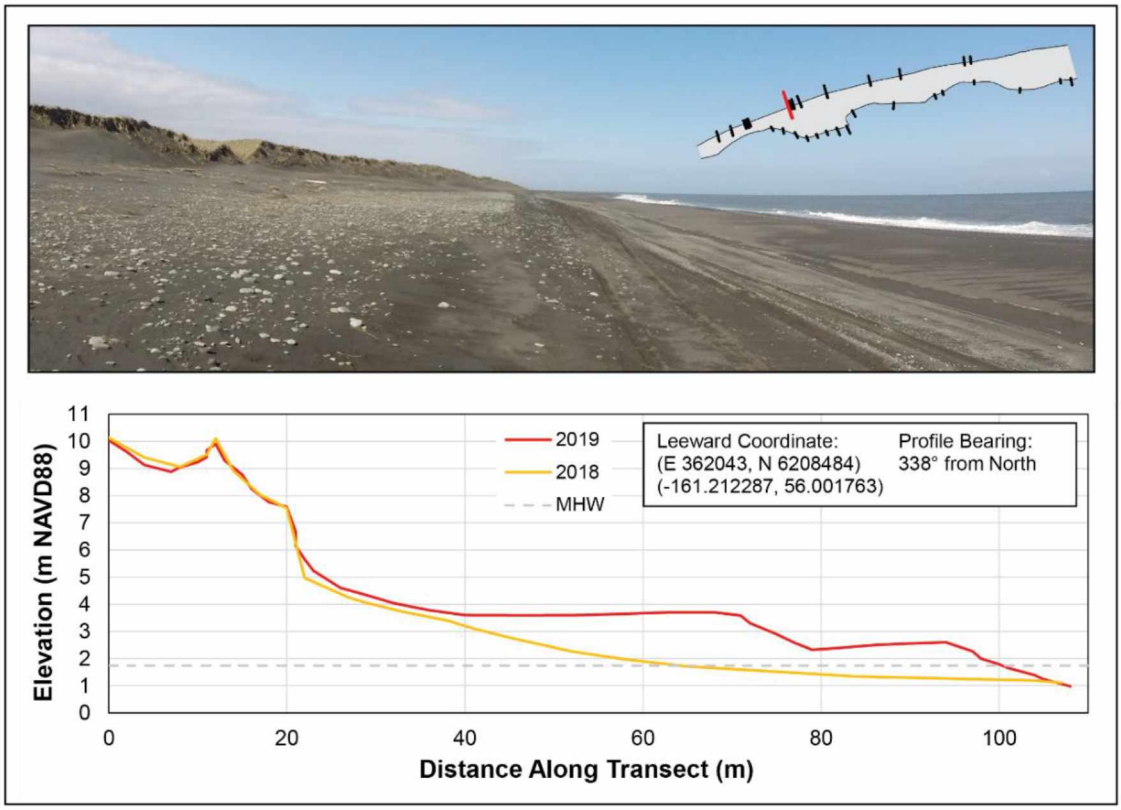

Figure 29. Cross-shore elevation profiles from the 2018 and 2019 within section C. Notice the storm berms deposited in 2019.

Section D – The shoreline fronting the airstrip exhibited the most pronounced erosion of all the survey units, with an average NSM of -55.8 m and a WLR of -1.53 ± 0.36 m/yr (90% confidence; WR2 = 0.98). The projected shoreline positions show the northern tip of the airstrip to be the most at-risk section to erosion, with the airstrip apron just 15 m from the 2019 shoreline (**Figure 30**). This portion of the shoreline contains dune-blowouts – lowering the elevation threshold for flooding – making it particularly vulnerable to both erosion and flooding. This is discussed further in section 4.2.2. This extreme shoreline retreat is also captured by the cross-shore elevation profiles, which were collected in 2014, 2015, and 2019 at this location. Between 2014 and 2019, the swash zone moved more than 50 m landward and observed more than 2 m of vertical erosion (**Figure 31**). This change is indicative of a sediment budget deficit (stronger wave erosion), with the width of the foreshore decreasing substantially. Given the accretion observed just down drift from this section (the tip of the spit), the eroded sediment from section D has significantly contributed to the lengthening of the spit over the last few decades.

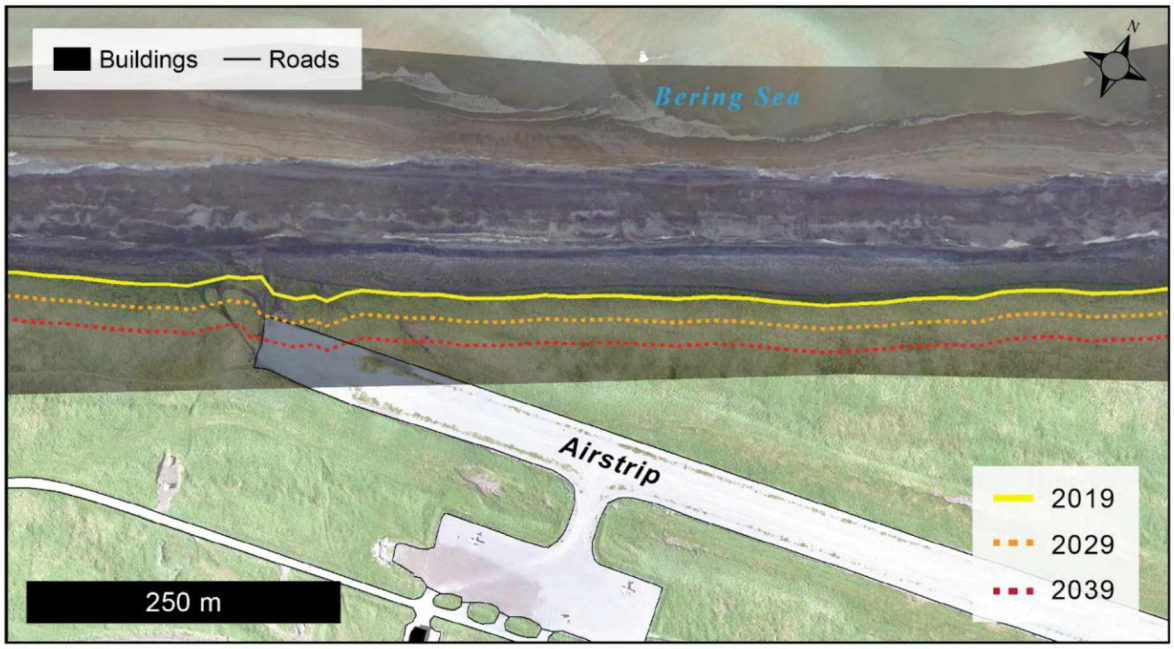

Figure 30. Map showing the projected shoreline positions (2029 and 2039) across section D from the 2019 shoreline. Notice how the projected shorelines intersect the northernmost section of the airstrip, which is only 15 m from the position of the 2019 shoreline.

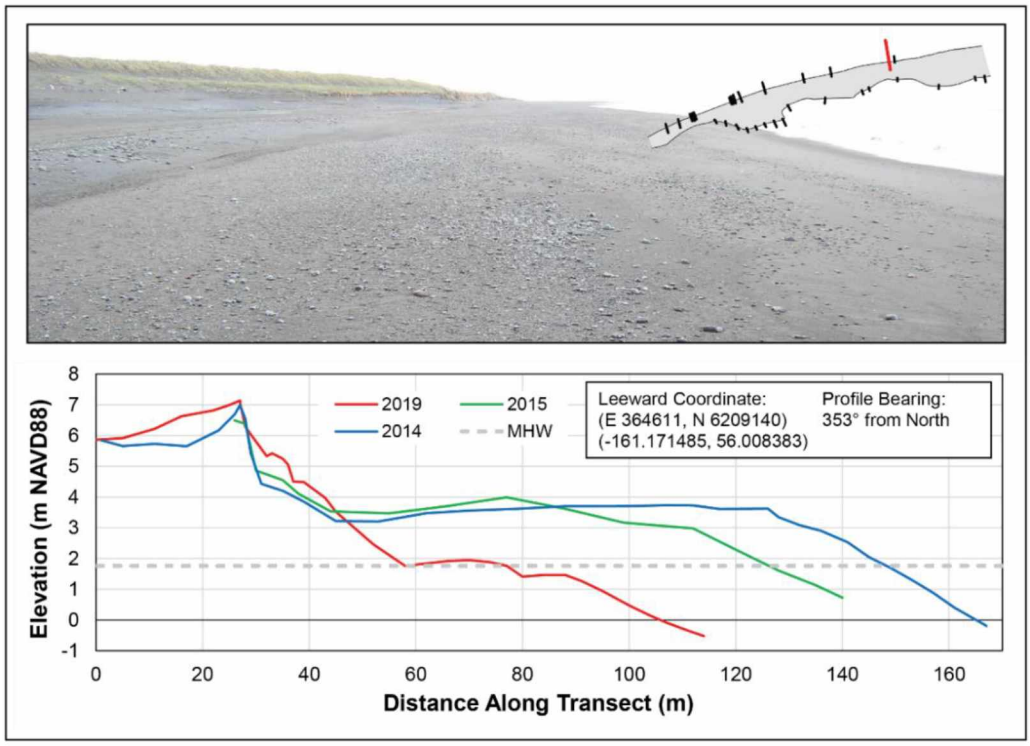

Figure 31. Cross-shore elevation profiles from 2014, 2015 2018, and 2019 within section D. Notice the swash zone moved more than 50 m landward and observed more than 2 m of vertical erosion**.**

3.3 Patterns of Flooding Vulnerability

3.3.1 Single Value Threshold Map

The SVTM identified areas of relatively high elevation most safe from flooding and that serve as natural levees to flooding. The foredune fronting the community provides a tenuous stopbank, protecting the area from sorm and tsunami flooding from this direction. Even so, section 4.4. discusses instances of breaching and overwash occuring along the spit on the ocean side during particualry high storm-tide events. The SVTM identified another dune ridge that runs diagnal (W to E) to the modern day incipient foredune ridge, along which the community is oriented. Besides these two ridges, most of the community lies on relatively low land with most properties below 3 m MHW (**Figure 32**). Of the 118 structures within the area of interest, 7% of all structures fell within the 0-1 m MHW elevation interval, 40% within the 1-2 m interval, 22% within the 2-3 m interval, and 31% fell above 3 m MHW (**Table 8**).

Table 8. Overview of the building elevations in Nelson Lagoon, organized by infrastructure class. Values are approximated and represent the percentage of each infrastructure class that fell in each flood hieght interval. Flood height intervals are in meters relative to Mean High Water (MHW).

Class	0-1 m	1-2 m	2-3 m	3+ m	Total
Residential (n = 34)	9%	29%	35%	26%	**100%**
Public (n = 12)	0%	75%	17%	8%	**100%**
Commercial (n = 8)	20%	35%	10%	35%	**100%**
Miscallaneous (n = 64)	6%	40%	18%	36%	**100%**
All (n = 118)	***7%***	***40%***	***22%***	***31%***	***100%***

A comparison of photographs documenting high storm-tide water levels and the SVTM corroborate the spatial patterns of flooding vulnerability identified by the model, but also provide a geodetically referenced elevation to the documented flood event (**Figure 33**) (i.e., Overbeck, 2017; Buzard et al., 2020). The safest areas of the community identified by the SVTM also match with the tsunami hazard map of Nelson Lagoon, produced by the Alaska Earthquake Center for the Alaska Department of Geologic and Geophysical Surveys (*see section 4.2.1.*) (Suleimani et al., 2020).

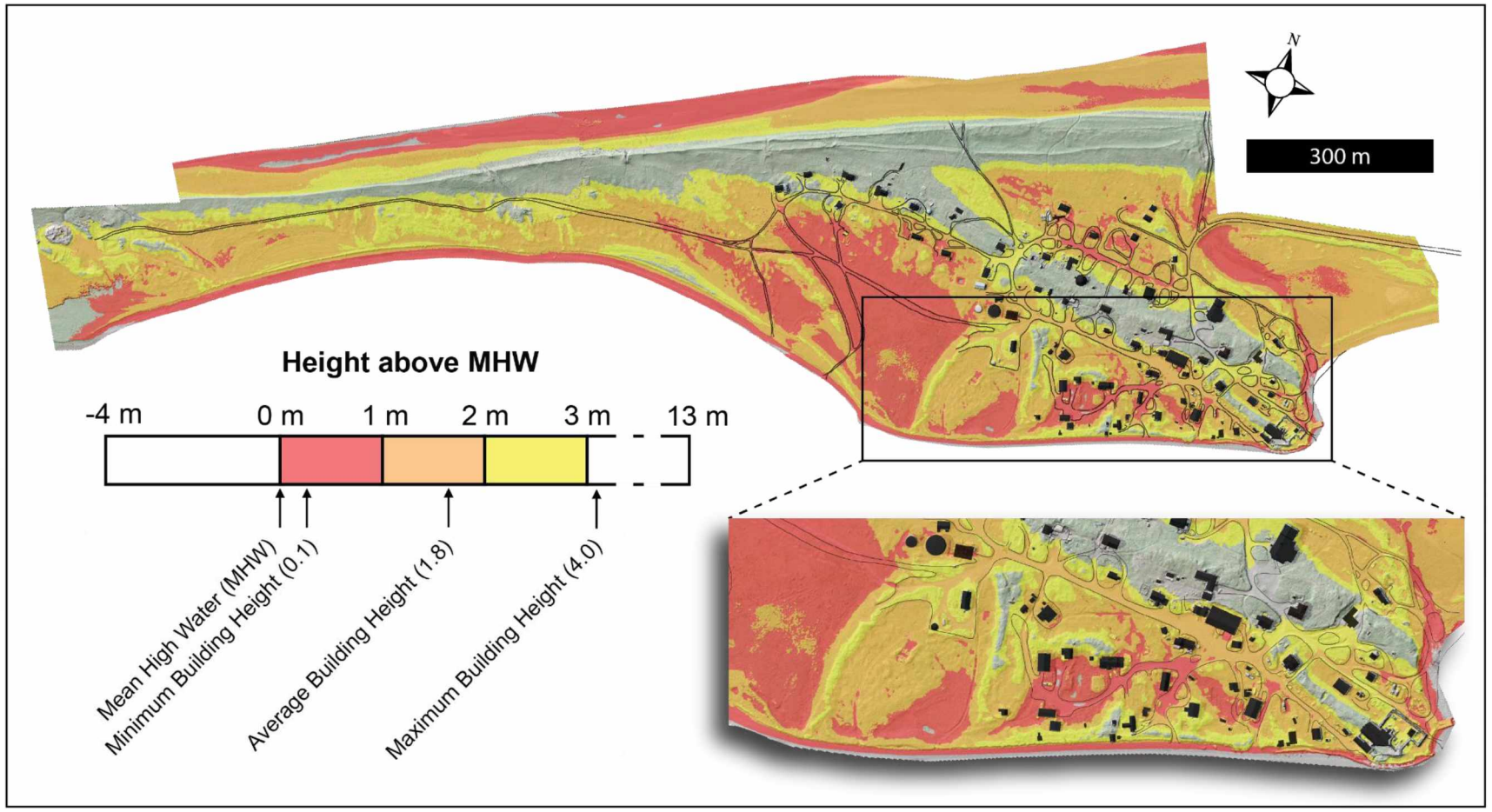

Figure 32. Single value threshold flood risk map of the Nelson Lagoon residential area, color coded based off elevation in meters above mean high water. Buildings and roads are symbolized in black. The minimum, average, and maximum building heights are provided. Elevations between -4 and 0 as well as elevations between 3 and 13 meters are transparent. Building height is the height of the ground level near the building, above which the building would be expected to be flooded, although first floor elevation surveys were not used in this analysis.

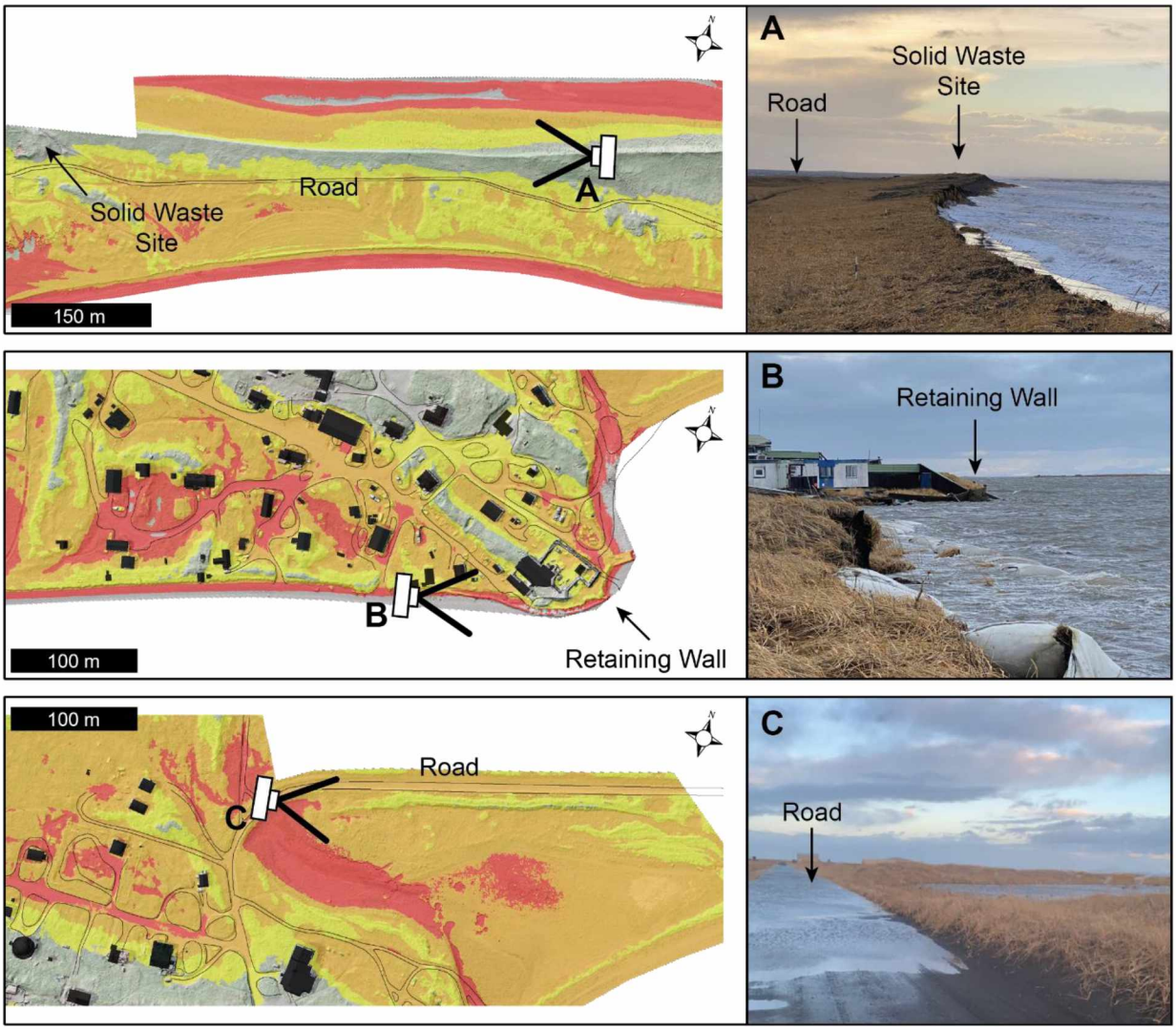

Figure 33. Graphic showing insets of the larger SVTM where photographs of high storm-tide events have been captured. Each letter on the map corresponds to the images on the right, with key features identified in each. Flooded areas captured by the images are areas identified by the SVTM as vulnerable. Images provided by Angela Johnson, November 2020.

3.3.2 Delft3D FM Computational Setup

The topobathymetric model covers an area of approximately 6,000 km^2 and spans 120 m in elevation. It represents the best available bathymetric and topographic datasets for the Nelson Lagoon and Port Moller area (**Figure 34**). The elevation surface produced by this project will be updated with the survey data collected by NOAA later this year (*see section 4.5*).

The Delft3D FM functionality test carried out over the elevation surface captured depth averaged horizontal current velocities forced with time varying water levels and wind fields. The results show the fastest moving water during actively ebbing or flooding tides concentrated in the main channels and constricted passages between hydraulic divides (i.e., Herendeen Bay, Port Moller, Nelson Lagoon) (**Figure 35**). During the ebb or flood of the tide, passages between hydraulic divides observed currents speeds of up to 3 m/s, whereas the main channels connecting the greater bay area to the Bering Sea observed current speeds of approximately 1-2 m/s. Though, by volume, most of the water column throughout the domain observed current speeds of roughly 0.5 m/s during each tide phase. This agrees with HDR's much smaller MIKE hydrodynamic model of non-storm conditions (velocity range of 0.5 – 2 m/s), which was validated via Acoustic Doppler Velocimeters (ADVs) (HDR, 2014a). As such, the elevation surface produced by the project will subsequently be included in a synoptic scale model in order to simulate surge events within Bristol Bay forced by time and space varying MSLP and wind fields (*section 4.4*).

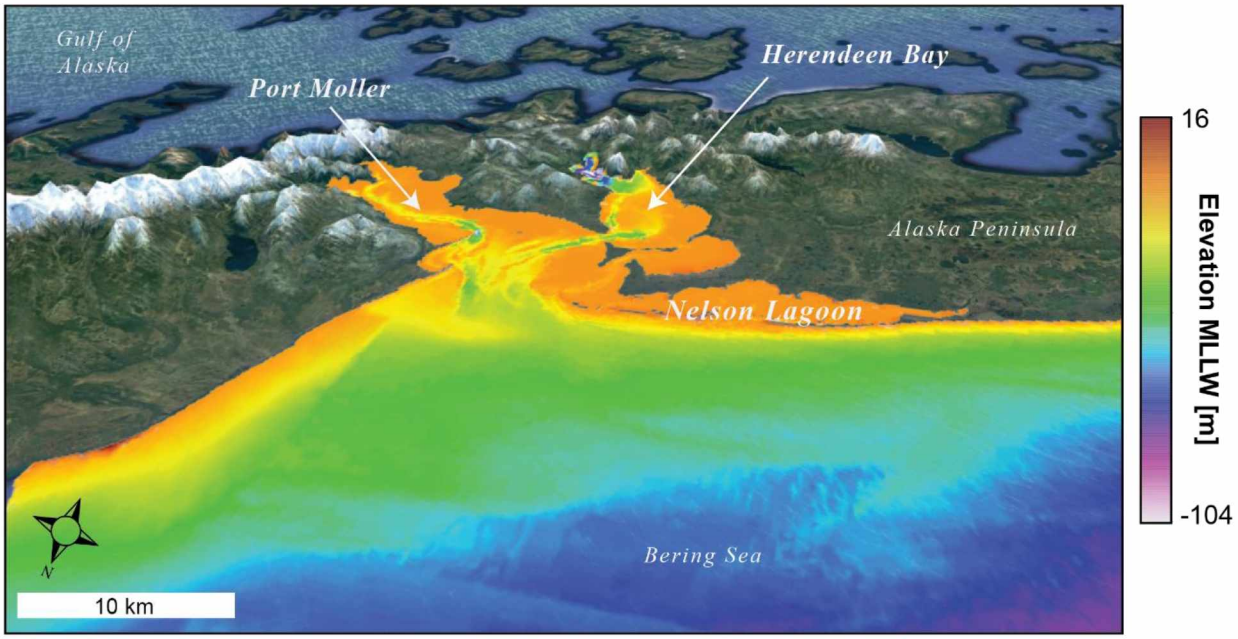

Figure 34. 3D rendering of the produced topobathymetric elevation model, shown in Google Earth.

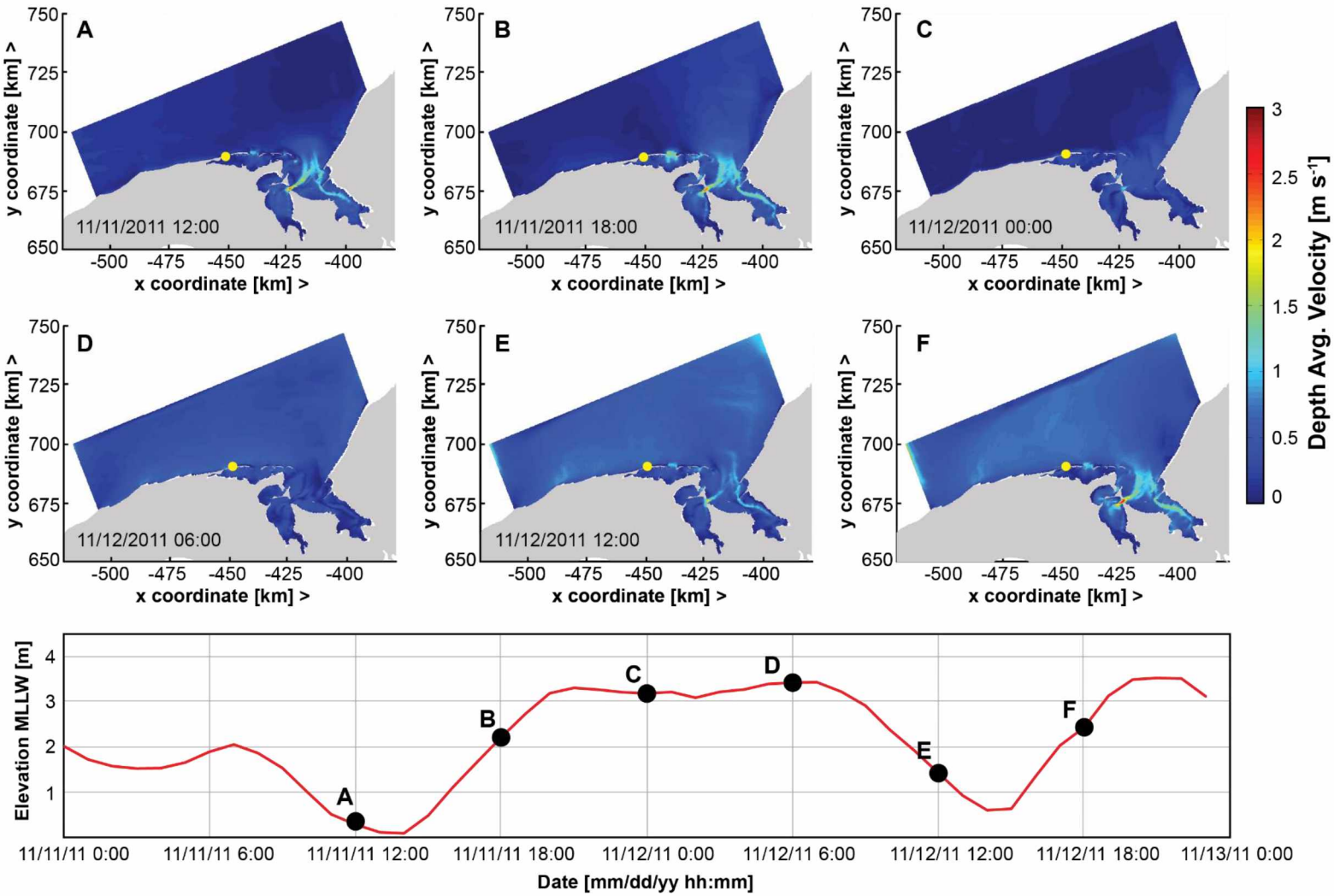

Figure 35. Diagrams showing the depth averaged velocity of the water column in six-hour increments over the temporal domain (11/11/11 0:00 to 11/13/11/ 0:00). The lower plot shows the water level fluctuations the model was forced with. Letters correspond to the water level height in each inset. Nelson Lagoon shown as yellow circle. Currents are quickest when the tide is actively rising or falling.

CHAPTER 4

DISCUSSION

4.1 Overview

By assessing erosion and flooding vulnerabilities for the Nelson Lagoon community, this study adds to an ever-growing database of such assessments statewide; which, ultimately, advance our understanding of regional coastal change in a shifting environment (Buzard, 2017; Overbeck et al., 2017; Bronen et al., 2020). The products produced for this project serve to substantiate anecdotal observations by local residents, with the ultimate goal of informing erosion mitigation efforts (i.e., Bronen, 2013; Birchall and Bonnett, 2019). Beyond this, the continued relationship with the community of Nelson Lagoon has led to the procurement of survey equipment as well as permanent oceanographic instrumentation at the community (*see section 4.4*). The areas identified as the most vulnerable are discussed in the subsequent sections, with an emphasis placed on distinguishing driving mechanisms as well as strategies for mitigation (i.e., Smith, 2014). Climate, oceanographic, and tectonic related factors that may compound the risks identified by this project are examined below as well (i.e., Lantz et al., 2020).

4.2 Spatial Patterns of Vulnerability and Implications

The non-linearity of the shoreline changes reflect the dynamic nature of the processes operating along the spit. Locations that were particularly dynamic include the accretional tip of the spit, and the two erosional lobes on the ocean side of the spit (solid waste disposal site and airstrip). The coastline fronting the community on the lagoon-side is also an area of interest, given the proximity of the erosional shoreline to the buildings there (1 to 15 m). It was found through the shoreline change analysis, elevation profiles, and time lapse photography from cameras installed by UAF ACGL that the erosion signal on both sides of the spit is

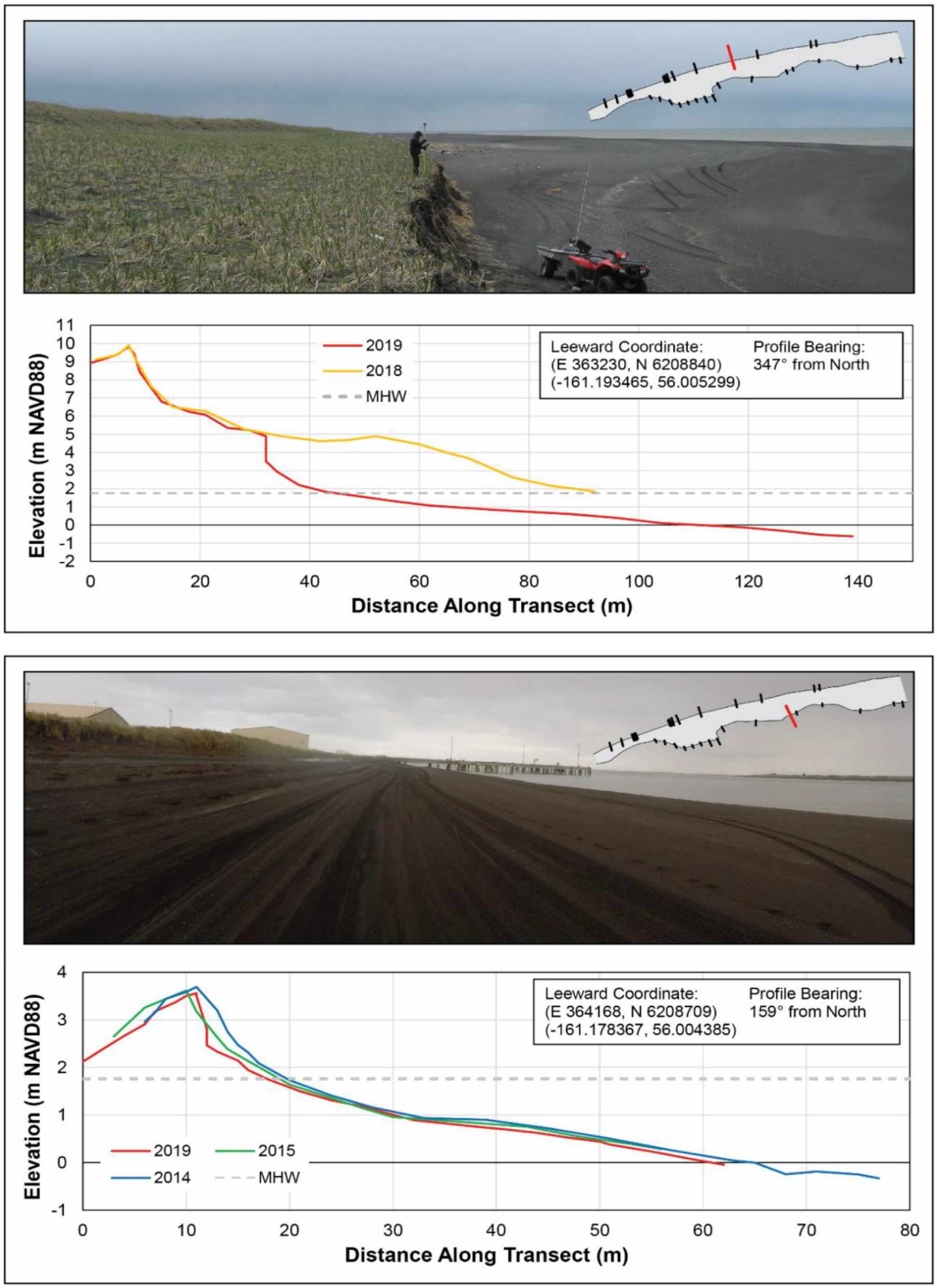

Figure 36. Cross-shore elevation profiles from the ocean side (top) and lagoon-side (bottom) of the Nelson Lagoon spit. Notice the increase in the slope of the dune face as it retreats landward on both sides of the spit

predominantly driven by high storm-tide events, coupled with significant wave action. This is especially the case along the ocean side shoreline. As such, the long-term erosion rates ultimately reflect the combined erosional impact of just a few, intermittent storms. The spatial variability in the beach's response to extreme storm events is probably caused by variability in the height and extent of the foredunes alongshore (Houser et al., 2008). The elevation profiles show that, for the most part, the morphological responses to storm events along beaches on both sides of the spit is erosion at the extreme upper edge of the intertidal zone; more precisely, erosion at or near the vegetation that steepens the slope of the pre-existing foredune as it retreats landward (**Figure 36**). UAV and time-lapse photography also reveal that overwash occurs frequently along the ocean shoreline during autumn months. Overwash deposits are easy to spot since they "bury" the vegetation 10s of meters inland of the incipient foredune (**Figure 37**).

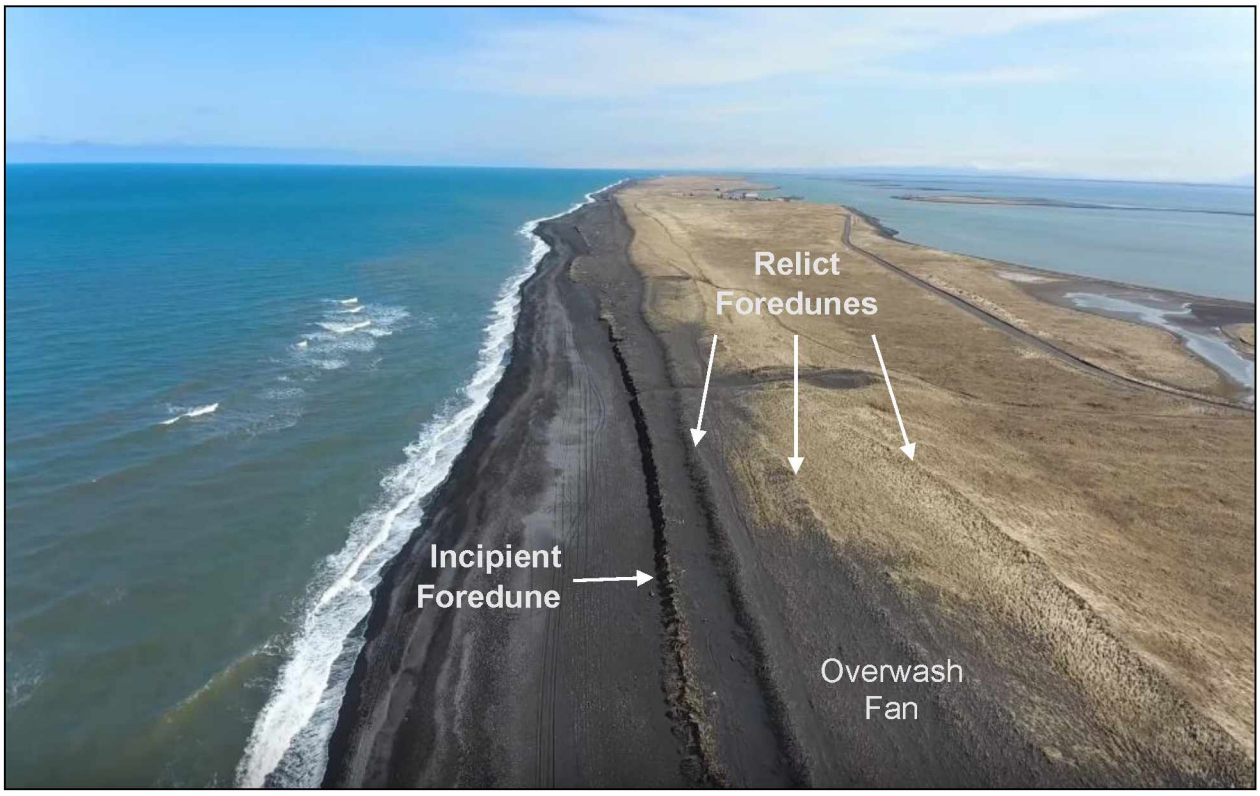

Figure 37. UAV imagery shoring the remnants of overwash deposits along the ocean side of the Nelson Lagoon spit. The road on the right goes from the community to the dock and airstrip. Notice how sand has blown over the outer foredune onto the older surfaces. April 2018.

While overwash events may appear to be catastrophic in the short-term, they can be considered a quasi-continuous process that has shaped the spit over longer timeframes (10^2 years) (Morton et al., 2000; Donnelly et al, 2006). On regional scales, factors controlling the frequency and magnitude of overwash include regional climate, wave and tidal conditions, the orientation of the coast relative to a storm, and nearshore bathymetry (Fletcher et al., 1995; Matias et al., 2010). On local scales, washover locations and dimensions are primarily influenced by nearshore bathymetry, beach topography, and back-beach elevations (Leatherman, 1977; Morton and Salleneger, 2003).

The implications associated with the spit getting longer and narrower is important to consider as well and alludes to the local regime being one of net marine transgression (*see section 4.3.1*) (FitzGerald et al., 2018). The long-term evolution of the spit will ultimately be driven by a complex interaction between distinct morphodynamic elements: erosion of the bluffs updrift of the spit that are the ultimate source of much of the sediment feeding the spit complex, the erosive "neck" (landward end), and the depositional "hook." Between the neck and the hook lies a downdrift-migrating "fulcrum point" which tends towards a steady-state trajectory set by the angle of maximum alongshore sediment transport. Ultimately, this means the spit's shape, orientation, and progradation rate (and, thus, habitability) will be decided by the interplay between relative sea level rise and the rate of headland retreat (sediment supply to the spit) (Ashton et al., 2016). If the supply of sediment is interrupted or when sea level rise outpaces sediment inputs, the sand at the neck of the spit may be moved towards the head, eventually turning Nelson Lagoon into an island (i.e., Evans, 1942; FitzGerald et al., 2018; Silva et al., 2020).

4.2.1 Study Limitations

Erosion detection through measurements of aerial imagery is often accompanied by high positional uncertainty (e.g., Crowell et al., 1993; Romine et al., 2009; da Silva et al., 2016). Though, this project used high resolution, orthorectified aerial imagery in an effort to minimize horizontal uncertainties associated with delineating the shoreline indicators. Shoreline projections are based simply on the linear movement of the shoreline over the study period, weighted by the uncertainty of each shoreline. Areas with consistent linear motion through time

exhibit a higher mean WR2 value than those with non-linear motion. When interpreting uncertainty of projections, it is important to keep in mind that the uncertainty is closely related to the statistical correlation of the linear regression (Buzard, 2017). Most shoreline sections showed a relatively high WR2 value (>0.70), with the exception being the lagoon shoreline fronting the community (0.18). This is likely due to little change in the horizontal position of the vegline over the study period along this stretch; a testament to the effectiveness of the in-place erosion mitigation structures along the south side of the community.

Pertaining to the limitations of the flood vulnerability assessment, the SVTM assumes that an area with an elevation less than a projected flood level will be flooded like a "bathtub." Flooding areas were determined through a simple calculation procedure in a GIS environment where the elevation in each cell of the DSM is compared against MHW and all cells with values lower than each elevation "table" (elevation interval) are considered flooded (i.e., Yunus et al., 2016). The "bathtub" can be filled in two ways: with and without hydrological connectivity (Van de Sande et al., 2012). Bathtub models that consider hydrological connectivity, e.g., the passage of water from one cell to another, require that in addition to being below the flood level, an area must be hydrologically connected to the source of the flooding (e.g., the ocean or river) for it to be inundated. Several studies have applied bathtub models to map coastal flood inundation around the globe using both non-connected and hydrologically connected methods (Titus and Richman, 2001; Strauss et al., 2012). The SVTM for Nelson Lagoon was produced without hydrological connectivity. Though, given that Nelson Lagoon is relatively devoid of significant elevation changes that would "block" water flow and the land's vertical proximity to the underlaying water table, the SVTM matches the tsunami hazard map of Nelson Lagoon, produced by the Alaska Earthquake Center for the Alaska Department of Geologic and Geophysical Surveys (**Figure 38**) (Suleimani et al., 2020). The Alaska Earthquake Center's map *did* consider hydrological connectivity and other hydrodynamic processes not accounted for in the SVTM produced by this project but used a much lower resolution elevation surface. As such, the SVTM produced by this project also informs community planning given its significantly higher resolution and vertical control. Its application is best suited to identifying infrastructure *vulnerable* to flooding, not necessarily identifying individual structures that *would* flood during a storm-tide of specific magnitude.

Figure 38. Tsunami hazard map of Nelson Lagoon, produced by the Alaska Earthquake Center for the Alaska Department of Geologic and Geophysical Surveys (from Suleimani et al., 2020). Information on this map is intended to permit state and local agencies to plan emergency evacuation and tsunami response actions. The map is not appropriate for site-specific use or for land-use regulation. Notice that the spatial pattern of vulnerability matches that of the SVTM produced by this project (see figure 32).

4.2.2 Areas of Greatest Concern

The Airstrip (Section C) - The most pronounced erosion over the study period was recorded along the community airstrip with an average NSM of -55.8 m and a WLR of -1.53 ± 0.36 m/yr (90% confidence; WR2 = 0.98). The projected shoreline positions show the northern tip of the airstrip as the most at-risk section to erosion, with the airstrip being just 15 m from the 2019 shoreline. Since our field work at Nelson Lagoon, a high storm-tide event in November 2020 breached the foredune fronting the airstrip, opening its gravel pad to further erosion and potential inundation during future storm events (**Figure 39**). It is highly likely that steps to mitigate erosion at this location will be needed if the airstrip is to stay operational during future extreme storm-tide events.

Figure 39. Foredune breach along the ocean shoreline fronting the community airstrip. Image provided by Angela Johnson, November 2020.

Lagoon-side of the Community (Section B) – This section has consistently been identified by residents as the area of highest concern and in need of bolstered erosion mitigation. This is because, despite this stretch of coastline showing relatively lower rates of change when compared to other aeras, the proximity of the shoreline is much closer to residential and commercial infrastructure (**Figure 26**). In fact, flooding impacts this stretch on a regular basis during high storm-tide events (**Figure 40**) and some buildings on the shore have already been undercut by wave action and abandoned (**Figure 1B**). The average NSM was -6.30 m between 1983 and 2019, with a WLR of -0.19 ± 0.10 m/yr (90% confidence; WR2 = 0.76).

A timber seawall is already in place on this side of the community, although it is in poor condition due to undermining and flanking. Despite its poor condition, this wall has been the primary protection for the community for almost three decades, making it, overall, a highly successful structure. In recent years, the community has installed the following major erosion protection measures along this stretch (USACE, 2007): (a) gabions along the seawall to anchor existing wood in the breakwater (**Figure 41A**), and (b) approximately 170 linear meters of sediment containers constructed with geotextile fabric (**Figure 41B**).

Figure 40. A flooded road near the retaining wall on the east side of the community. This stretch of coastline floods regularly during high storm-tides. Image provided by Angela Johnson, November 2020.

Figure 41. Seawall and sediment containers in place along the lagoon coastline of the community. A) the seawall and gabions, the geotextile containers can be seen on the left, and B) the geotextile containers fronting the community to the west of the seawall. May 2019.

HDR Alaska Inc. drafted plans to extend the mitigation structures to the west of the existing seawall, but also made clear that the seawall currently in place needs structural attention (HDR,

2015). Of the three potential plans compiled for this stretch (including additional geotextile containers, gabion mattress revetment, or a complete timber seawall), project cost estimates ranged between $700,000 and $1,500,000.

Solid Waste Disposal Site (Section A) – The shoreline fronting the solid waste disposal site showed among the highest average NSM across the spit, with a value of -29.6 m. The lagoon shoreline along this section observed significantly less change when compared to the seaward coastline (-7.6 m as opposed to -48.6 m avg. NSM). The average WLR across section A is -0.98 ± 0.36 m/yr (90% confidence; WR2 = 0.71). Given the morphology across this section of the spit, the seaward side is most vulnerable to erosion and overwash (**Figure 42**) and the lagoon-side is most vulnerable to inundation, considering it is very close to the water table. The foredune fronting the solid waste disposal site has been eroded by waves during high storm-tide events and, as a result, the north side of the disposal site has been flooded multiple times via the access road from the beach (**Figure 44**). Projected shoreline positions using the WLR rate shows that the solid waste disposal site will likely be eroded into the sea within the next three decades, depending on storm impact frequency and magnitude.

Figure 42. Photograph taken from the solid waste disposal site looking towards the community on the ocean side of the spit. As the bluff face erodes, sediment at or near the vegetation line is removed and there is an increase in the slope of the dune toe as it retreats landward. October 2018.

Figure 43. Photograph showing remnants of an overwash and flooding event at the access road from the beach to the solid waste disposal site, which can be seen to the left. October 2018.

4.3 Compounding Factors

4.3.1 Sea Level Rise

A large number of studies worldwide suggest that over the past 1,000 years global average (eustatic) sea level has risen at a rate of <2mm per year (Gornitz, 1995). Eustatic sea level has risen about 8–9 inches (21–24 centimeters) since 1880, with about a third of that coming in just the last two and a half decades. The rising water level is mostly due to a combination of meltwater from glaciers and ice sheets and thermal expansion of seawater as it warms. In 2019, global mean sea level was 3.4 inches (87.6 millimeters) above the 1993 average—the highest annual average in the satellite record (1993-present). From 2018 to 2019, global sea level rose 0.24 inches (6.1 millimeters) (Wuebbles et al., 2017; Cazenave et al., 2018; Davidson-Arnott et al., 2019).

Relative sea level rise (RSLR) is the combination of eustatic (global) sea level rise and local land subsidence (or in some cases, rise in land elevation). This local change in land elevation has a variety of causes, such as earthquake deformation cycles (section 4.3.2), groundwater reduction or increase, oil extraction, etc. RSLR in the Nelson Lagoon area seems to align with the global average rate, which means this signal is most likely not captured in the erosion rates measured

for this project. But, it is a factor that will accelerate erosion and flooding events over much longer timescales. The closest water level gauge to Nelson Lagoon that has recorded water level heights for any extended period had been NOAA's Port Moller, AK - Station ID: 9463502 (it has not been operational since ~2017) (NOAA, 2020). Average monthly water levels at Port Moller station over its entire operating period show a RSLR rate of 3.15 ± 1.94 mm/yr (**Figure 44**).

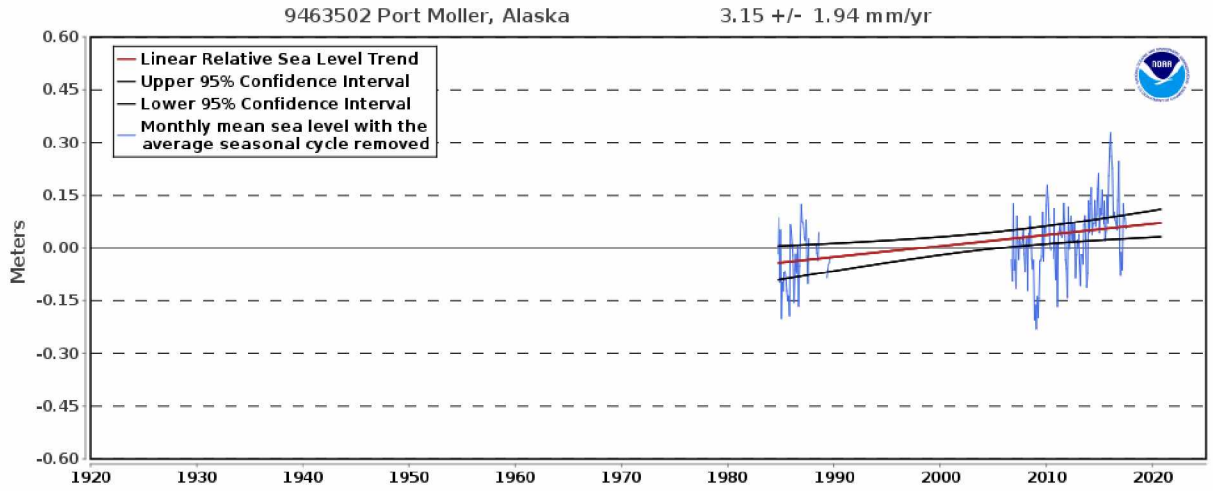

Figure 44. Plot showing the monthly mean sea level without the regular seasonal fluctuations due to coastal ocean temperatures, salinities, winds, atmospheric pressures, and ocean currents from Port Moller Station ID: 9463502. The long-term linear trend is also shown, including its 95% confidence interval. The plotted values are relative to the most recent Mean Sea Level datum established by CO-OPS. The relative sea level trend is 3.15 ± 1.94 mm/yr, based on monthly mean sea level data from 1984 to 2017 which is equivalent to a change of 1.03 feet in 100 years.

The next closest gauge is Sand Point, located approximately 80 km from Nelson Lagoon on the Pacific Ocean side of the Aleutian Islands. The reported RSLR at Sand Point is 0.92 mm/yr, equivalent to 0.3 feet/century, based on sea level data from 1972 to 2006 (NOAA, 2020). Estimates of eustatic sea level rise range from 90 mm to >240 mm per century (NOAA 2020).

One major challenge in predicting the response of beaches to increased mean sea level is their inherently dynamic character. This is due to the fact that their morphology responds relatively quickly to changes in sediment supply, as well as the hydrodynamic forces in action (including sea level but also waves, currents and river flows) in many ways. In addition, the morphological state of the beach itself affects the hydrodynamic conditions, leading to complex feedbacks

between coastal morphology and processes of deposition and erosion (Enríquez et al., 2019; Osswald et al., 2019). Since the spit fronts a lagoon with extensive tidal flats, Nelson Lagoon will most likely undergo increased erosion due to flood dominance within inlet channels and the creation of bay sediment sinks over long timescales (relevant to RSLR) (Dissanayake et al., 2012; Van Goor et al., 2003).

This is because the tidal prism of the entire back-barrier controls the size/number of tidal inlets along the barrier chain (Roos et al. 2013). Tidal prism can increase through the conversion of intertidal mudflats to open water and by decreasing frictional resistance of tidal exchange through channel enlargement and/or bay deepening (**Figure 45**) (FitzGerald et al., 2018). When barriers are breached during a storm, the sustainability of the new tidal inlet is dependent upon the inlet accessing a large enough tidal prism to keep it open (Tran et al., 2012; Roos et al., 2013; Escoffier, 2016). As the new inlet equilibrates to reversing tidal flow and wave conditions, sand is transported seaward and landward building ebb- and flood-tidal deltas, respectively. This represents a loss of sand from the barrier lithesome, which is the area that encompasses the depth of closure for a characteristic time interval (the most landward depth seaward of the beach for which there is no significant change in bottom elevation and no significant net sediment transport between the nearshore and the offshore) (Kraus et al., 1998).

However, given the most immediate and substantial driver of Nelson Lagoon's dynamism is its wave and storm climate, it is most useful to record the number and magnitude of storm events that impact the spit moving into the future. Dune erosion events caused by wave erosion alternate with prolonged periods of dune accretion caused by aeolian processes. Climate change may affect these processes too; changes in wind patterns and beach width can influence yearly aeolian supply to the foredunes (De Winter and Ruessink, 2017). This interconnectedness between the main mechanisms of morphodynamic change, exemplifies the complexity of coastal systems like that at Nelson Lagoon (*see sections 4.4-4.5*).

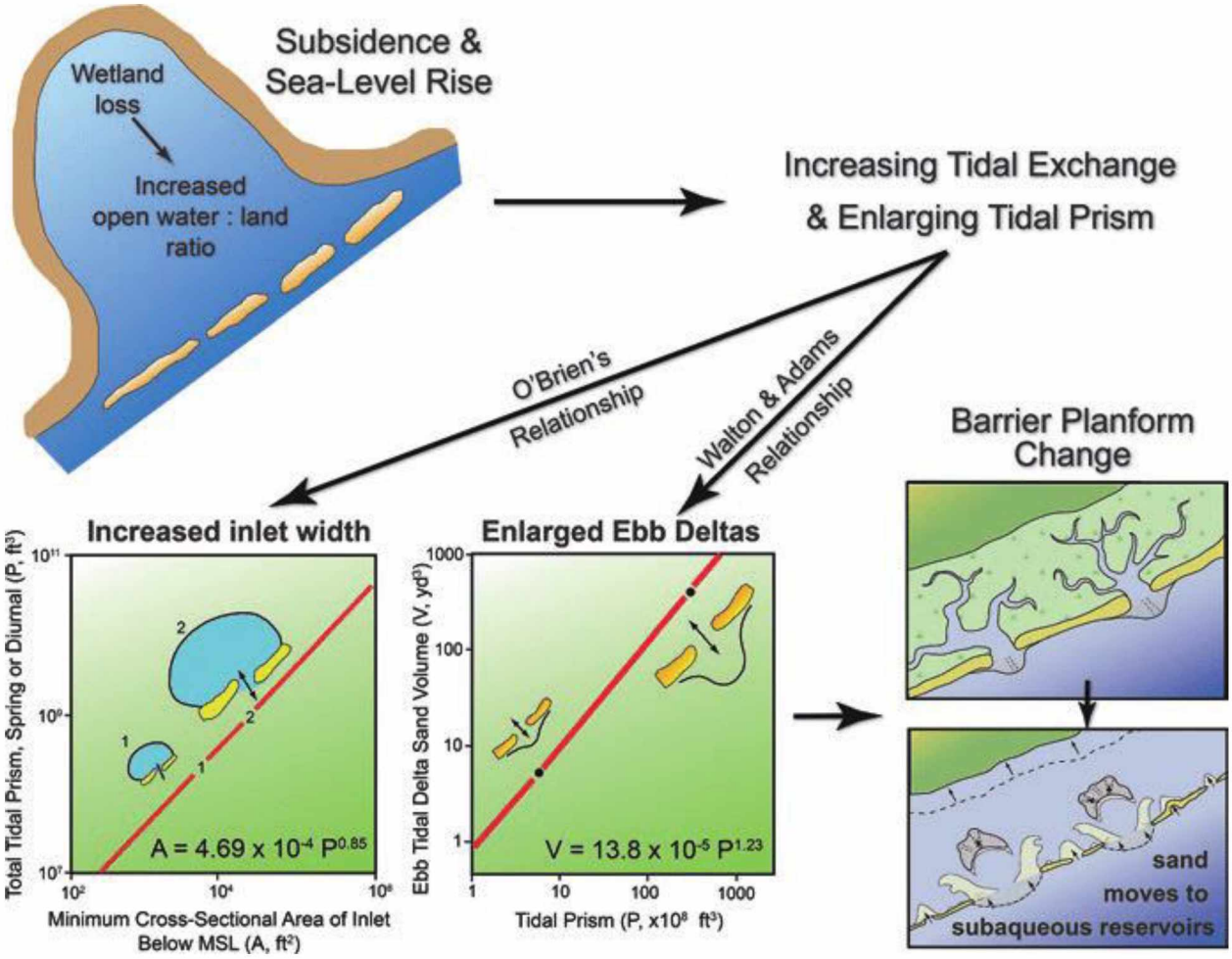

Figure 45. Flowchart illustrating how wetland loss leads to increasing tidal prism, larger tidal inlets, and enlarging ebb-tidal deltas. Ultimately, sand from barrier reservoirs is transferred to ebb- and flood-tidal deltas causing barrier transgression (from FitzGerald et al., 2018).

4.3.2 Coseismic and Interseismic Deformation

As stated above, global eustatic sea-levels driven by global distribution of water during climate fluctuations over millenial timescales play a major role in RSL's. But, over smaller spatiotemproal scales these broader eustaic trends can be damped or accentuated by regional seismicity and/or isostacy related deformation (Shugar et al., 2014; Maio et al., 2017). Earthquake deformation cycles (interseismic vs. coseismic) along the Aleutian megathrust subduction zone have had catastrophic impacts to coastal systems (Briggs et al., 2014; Kelsey et al., 2015). The deformation cycle's impact on RSL of a particular location is dependent on whether it is positioned landward or seaward of the locked zone (zone between the convergent

plates capable of generating earthquakes; the base of the seismogenic zone is the top of the more ductile asthenosphere) and at what part of the deformation cycle is occuring (Hamilton et al., 2005). Between earthquakes (refered to as interseismic), landward areas of the subduction zone are gradually up lifted, resulting in a drop in sea-level, while areas seaward experience gradual subsidence and a rise in sea level (Nelson, 2007). The opposite is true during an earthquake (refered to as coseismic); coseismic uplift occurs seaward (sea level drop) and coseismic subsidence (sea level rise) occurs landward of the locked zone. Unlike the more gradual interseismic changes in the land surface, coseismic changes occur simultaneously with an earthquake and can have catastrophic impacts to coastlines (Plafker, 1969; Shennan et al., 2014). As stated in section 3.3.3., the tectonic setting of Nelson Lagoon is unique in that it is located withing the Shumigan Gap, which is characterized by a lack of seismic activity (**Figure 46**) (Crowell and Melgar, 2020).

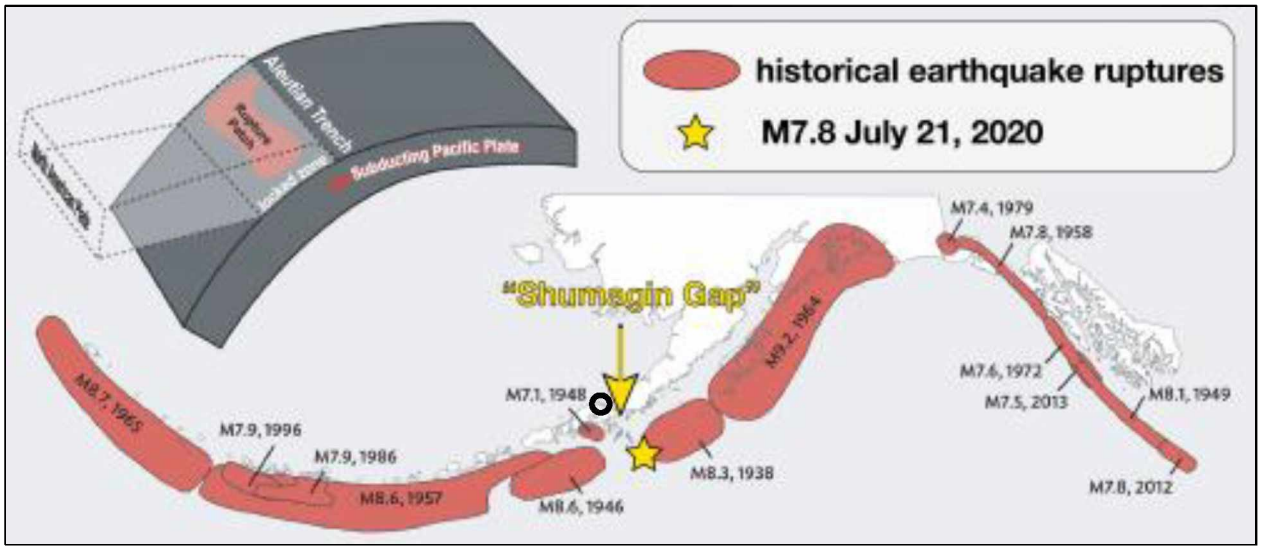

Figure 46. Map showing the location of the Shumigan Gap and all large recent earthquakes along the Aleutian Subduction Zone, including the magnitude 7.8 in the Shumagin Gap that occurred July 21, 2020. Graphic courtesy Alaska Earthquake Center. Nelson Lagoon is symbolized by the black circle.

However, in July 2020, a Mw 7.8 earthquake (first large earthquake in the area in more than a century) initiated directly to the east of Simeonof Island offshore of the Alaska Peninsula (**Figure 46**). The earthquake ruptured the eastern part of the Shumagin Gap. A study by Crowell and Melgar (2020) investigated the rupture kinematics of the earthquake using a joint inversion

of high-rate GNSS and strong-motion data. They found that the rupture was focused between depths of 30–45 km, starting east of the Shumagin Islands and rupturing downdip towards the northwest, with little slip west of 160°W. This means the 2020 earthquake ruptured mainly the unlocked portion of the subduction zone and did not rupture into regions that are highly locked. This peculiar pattern of slip was also seen previously in 1917, indicating that the structure of the fault zone in the area may be conducive to earthquakes and some interseismic locking is occurring to allow for M7.5–8 earthquakes roughly every century (Crowell and Melgar, 2020).

Since Nelson Lagoon is located in this seismic gap along the Aleutian megathrust subduction zone, GNSS velocity vector data closest to Nelson Lagoon (~40 km) shows little to no vertical interseismic deformation. CORS station AC41 located in Port Moller shows that the area is moving to the north (2.55 mm/yr) and west (-6.3 mm/yr), with net uplift (0.04 mm/yr). However, the variance of the vertical displacement data is larger than rate (σ = 0.09 mm/yr) and, thus, can be considered insignificant (**Figure 47**). This partially explains why the RSL rate computed from Port Moller reflects the global average rate so closely.

Coseismically, the GNSS velocity vector data would suggest that subduction occurred as a result of the July 2020 Mw 7.8 earthquake (**Figure 47**). This means, due to Nelson Lagoon's location in the Shumigan Gap, it observes negligble interseismic vertical displacemnt, but may expereince a coseismic subsidence event possibly every century (Crowell and Melgar, 2020). This is a very important caveat to the erosion and flooding vulnerability assessments. That is, abrupt coseismic subsidence can completely change the hydrodynamic and morphological setting of the entire area instantly (relative to geologic timescales).

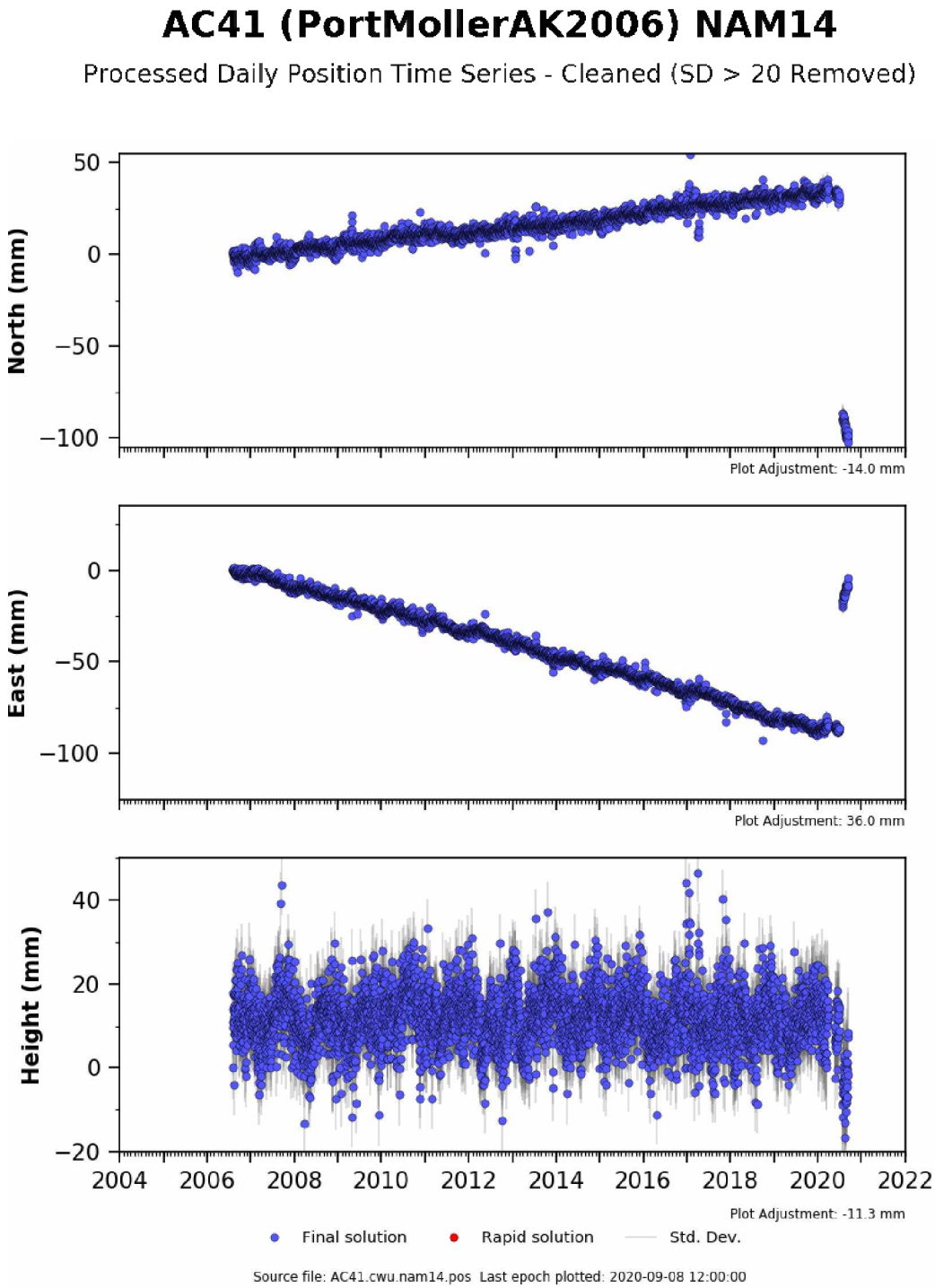

Figure 47. Processed daily position time series of GNSS station AC41 Port Moller, AK between 2006 and 2020, from the UNAVCO Data Center. Not including the Coseismic subsidence event evident in 2020, the timeseries reveals net north (2.55 mm/yr) and west (-6.3 mm/yr) lateral interseismic vectors, with negligible uplift (0.04 mm/yr).

4.4 Broader Impacts

This research provides quantitative measurements that can be applied to coastal decision making and engineering. In Alaska, these data are commonly limited to collections every 10–30 years, and even so, local observations and anecdotal accounts are seldom converted into consistent data metrics (Overbeck et al., 2017). Although in-depth analysis on a community-by-community basis is expensive, these analyses may save money by applying site-specific engineering designs to remedy such hazards. This form of analysis, if performed at all sites subject to hazardous conditions, would also give coastal managers and planners a prioritization system as to which hazards should be addressed immediately, and which hazards may be addressed over time, allocating state and federal funding based on community needs (Smith, 2014).

Thus, coastal vulnerability assessments such as this one are important for engineering decision making throughout all of western and northwest Alaska, in communities that experience similar geohazards (i.e., Smith, 2014). This work has generated datasets for scientists and engineers, visual aids for decision makers, and personal connections with community members. The results from this work have increased the capacity of Nelson Lagoon to respond to an ever-changing environment (Buzard, 2017).

For example, this project in collaboration with the UAF ACGL and State of Alaska DGGS, has leveraged:

- A permanent geodetically referenced water level gauge at Nelson Lagoon, which will maintain a tidal datum, predict tides, and record storm surges, all on a publicly accessible web interface in collaboration with the Alaska Ocean Observing System (AOOS),
- Two SOFAR Spotter V2 buoys for Nelson Lagoon through a FEMA QAPP in collaboration with the Native Village of Nelson Lagoon Environmental Coordinator, and
- A DJI Phantom 4 RTK UAV for Nelson Lagoon through a FEMA QAPP in collaboration with the Native Village of Nelson Lagoon Environmental Coordinator.

All data collected, compiled, and produced by this project have been accumulated into one source and include:

- survey grade GNSS data,
- orthorectified aerial imagery,
- current high-resolution DSMs,
- local tidal datum,
- historic wind, wave, temperature, water level timeseries,
- bathymetry,
- sediment grain size analyses,
- hydrodynamic modeling set up(s),
- delineated historic and modern shorelines,
- infrastructure GIS data,
- time-lapse photography,
- flood documentation photography, and
- SVTM(s).

In accordance with Objective 4 of the project objectives, the following outreach and data sharing has occurred:

- The UAV derived DSM has been included in an online inundation mapping interface through National Weather Service (NWS),
- The shoreline change analysis and GNSS cross-shore elevation profiles have been shared with firms such as LeMay Engineering & Consulting, Inc. and the Alaska Native Tribal Health Consortium (ANTHC),
- The bluff top edge shapefiles will be added to the DGGS Coastal Hazard Program's Shoreline Change Tool (http://maps.dggs.alaska.gov/shoreline), and the beach profiles added to the Alaska Coastal Profile Tool (http://maps.dggs.alaska.gov/acpt),
- The combined work of this project has contributed to a holistic coastal hazard assessment of the Native Village of Nelson Lagoon through the UAF ACGL. The workflows and templates produced by this project have also fed into as many as 14 other such assessments of communities around Bristol Bay and the Bering Sea region,

- The topobathymetric model produced of the greater Nelson Lagoon area will be included in a Bering Sea scale model to be produced for an Alaska Sea Grant project. The project will leverage permanent water level sensors in Nelson Lagoon as well as Dillingham and make use of an existing water level gauge in Naknek (*see section 4.5*) (https://joasurveys.com/rtwl/nak/), and
- The methods and results of this project has been publicly presented at the American Geophysical Union (AGU) 2019 conference in San Francisco, CA and will be presented in the 2021 Geological Society of America (GSA) Annual Conference as well as the 2021 Western Alaska Interdisciplinary Science Conference.

4.5 Future Work

Continued work is being carried out to improve the vulnerability assessment of Nelson Lagoon and another field work campaign is planned for autumn 2021. This will include repeat beach profiles and UAV surveys, along with continued correspondence with members of the community. These datasets will feed into the comprehensive coastal hazard assessment produced by ACGL and will be updated annually.

Once updated with the planned bathymetric survey NOAA is to carry out this year, the topobathymetric elevation model produced by this project will be incorporated into a Bering Sea sized Delft3D FM model in order to fill in documentation gaps of historic storm surge related TWLs within Bristol Bay. This is an Alaska Sea Grant Project that will use time and space varying MSLP and wind fields to simulate surge development and propagation, using planned geodetically referenced water level gauges in Dillingham and Nelson Lagoon as well as an established gauge in Naknek. This model will be shared with the NWS, DGGS, and will greatly benefit local residents and community decision makers. These efforts are also responsible for the acquisition and installation of real time wave buoys, which will be installed in Naknek, Dillingham, and Nelson Lagoon this year.

CHAPTER 5

CONCLUSION

5.1 Application of Surveyed & Remotely Sensed Data

Developing and maintaining GIS data layers of shoreline positions and elevation datasets (GNSS, DSMs, etc.) through time benefit not only community decision makers, but also scientists and engineers. Integrating such data with analogous datasets collected by state or private entities across multiple communities in the region will allow much more robust vulnerability assessments in the future, but also elucidate the greater response of Bristol Bay's coastlines to a changing environment across its gradient of wave and tide dominated settings.

5.2 Community Threat Assessment

There are multiple areas, buildings, and utilities in Nelson Lagoon that are in immediate risk of erosion and flooding related geohazards:

- The main water line to the community runs along the entire length of the spit, which now includes regions where there is <100 m of land between the lagoon and open ocean. This water line has been exposed before and will be exposed more frequently in the future since the spit is getting longer and narrower.
- The airstrip has been exposed to the open ocean side of the spit since this project identified it as an area of high concern due to erosion. It is inevitable the north portion of the airstrip will flood in the future.
- The current erosion mitigation structures along the lagoon-side of the community have been successful at dampening rates of erosion of their operational lifetimes, but they are structurally failing. This is a particularly important point to address moving forward, given that buildings and utilities are mere meters away from the shoreline at this location. Regular flooding occurs here during high storm-tides. Engineering options and project cost assessments for this stretch have been carried out by HDR Alaska, Inc., though the community has very limited available construction funds.

- The solid waste disposal site to the west of the community is at risk of flooding and erosion from the ocean side. Portions of the site have already flooded within the last few years. It is likely that further erosion and flooding will occur and may eventually erode material into the ocean within a few decades if no action is taken.

5.3 Coastal Resiliency of Nelson Lagoon

Nelson Lagoon faces many challenges related to coastal geohazards. The oceanographic setting means that any mitigation structures must withstand significant waves and currents, large tides, and ice. The geologic setting means that there are limited locally available construction materials and resources, which equates to most engineering solutions being expensive to undertake. The climatic setting means that there is a short (seasonal) construction window for any largescale projects. Also, the outdated and failing existing shoreline protection structures mean that there is limited time to procure funding and implement new or bolstered erosion defenses.

However, the strongest defense against coastal geohazards at Nelson Lagoon has been, and is, its extremely proactive and hard-working people. An overwhelming majority of the residents of Nelson Lagoon have lived there most of their lives. The community has ongoing erosion monitoring efforts and communication with state and private entities. Great strides have been made by the Nelson Lagoon Environmental Department in opening and maintaining funding channels for instrumentation and equipment to help address the community's changing coastline.

LITERATURE CITED

ADEC, Alaska Department of Environmental Conservation, 2004. Source water assessment, A hydrogeologic susceptibility and vulnerability assessment for Nelson Lagoon water system. Report PWSID#260804.001.

ADLWD, Alaska Department of Labor and Workforce Development., 2011. Alaska Local and Regional Information: Nelson Lagoon.

Agisoft, L.L.C. and St Petersburg, R., 2019. Agisoft Metashape User Manual: Professional Edition.

Amante, C. and B. W. Eakins, 2009: ETOPO1 1 Arc-Minute Global Relief Model: Procedures, Data Sources and Analysis. 24, NOAA Technical Memorandum NESDIS NGDC, 19 pp.

Anders, F.J. and Byrnes, M.R., 1991. Accuracy of shoreline change rates as determined from maps and aerial photographs. Shore and Beach, 59(1), pp.17-26.

Antunes, N.S.M., 2000. The Importance of the tidal datum in the definition of maritime limits and boundaries. Ibru.

AOOS, Alaska Ocean Observing System, 2014. Data from: Historical Sea Ice Atlas: Alaska Sea Ice, Mid-1800s to the Present. Fairbanks: University of Alaska.

Arnold, D.E., 2020. Seamless Digital Elevation Model (DEM) creation for the Mississippi River in Louisiana to support hydrologic modeling.

Ashton, A.D., Nienhuis, J. and Ells, K., 2016. On a neck, on a spit: controls on the shape of free spits. Earth Surface Dynamics, 4(1), pp.193-210.

ASOS, Automated Surface Observing System Users Guide, 1998. National Weather Service ASOS Program Office, 74 pp.

Atkinson, D.E., 2005. Observed storminess patterns and trends in the circum-Arctic coastal regime. Geo-Marine Letters, 25(2-3), pp.98-109.

Bader, J., Mesquita, M.D., Hodges, K.I., Keenlyside, N., Østerhus, S. and Miles, M., 2011. A review on Northern Hemisphere sea-ice, storminess and the North Atlantic Oscillation: Observations and projected changes. Atmospheric Research, 101(4), pp.809-834.

Barnhart, K.R., Overeem, I. and Anderson, R.S., 2014. The effect of changing sea-ice on the physical vulnerability of Arctic coasts. The Cryosphere, 8(5), pp.1777-1799.

Bengtsson, L., Hodges, K.I. and Roeckner, E., 2006. Storm tracks and climate change. Journal of Climate, 19(15), pp.3518-3543.

Bergillos, R.J., Masselink, G. and Ortega-Sánchez, M., 2017. Coupling cross-shore and longshore sediment transport to model storm response along a mixed sand-gravel coast under varying wave directions. Coastal Engineering, 129, pp.93-104.

Bernstein, L., Bosch, P., Canziani, O., Chen, Z., Christ, R. and Riahi, K., 2008. IPCC, 2007: climate change 2007: synthesis report.

Bheeroo, R.A., Chandrasekar, N., Kaliraj, S. and Magesh, N.S., 2016. Shoreline change rate and erosion risk assessment along the Trou Aux Biches–Mont Choisy beach on the northwest coast of Mauritius using GIS-DSAS technique. Environmental Earth Sciences, 75(5), p.444.

Birchall, S.J. and Bonnett, N., 2019. Local-scale climate change stressors and policy response: the case of Homer, Alaska. Journal of Environmental Planning and Management, 62(13), pp.2238-2254.

Boak, E.H. and Turner, I.L., 2005. Shoreline definition and detection: a review. Journal of coastal research, 21(4 (214)), pp.688-703.

Bogardus, R., Maio, C., Mason, O., Buzard, R., Mahoney, A. and de Wit, C., 2020. Mid-Winter Breakout of Landfast Sea Ice and Major Storm Leads to Significant Ice Push Event Along Chukchi Sea Coastline. Frontiers in Earth Science, 8, p.344.

Briggs, R.W., Engelhart, S.E., Nelson, A.R., Dura, T., Kemp, A.C., Haeussler, P.J., Corbett, D.R., Angster, S.J. and Bradley, L.A., 2014. Uplift and subsidence reveal a nonpersistent megathrust rupture boundary (Sitkinak Island, Alaska). Geophysical Research Letters, 41(7), pp.2289-2296.

Bronen, R., 2013. Climate-induced displacement of Alaska Native communities. Washington DC: Brookings Institution (US).

Bronen, R., Pollock, D., Overbeck, J., Stevens, D., Natali, S. and Maio, C., 2020. Usteq: integrating indigenous knowledge and social and physical sciences to coproduce knowledge and support community-based adaptation. Polar Geography, 43(2-3), pp.188-205.

Brower Jr, W.A., Diaz, H.F., Prechtel, A.S., Searby, H.W. and Wise, J.L., 1977. Climatic Atlas of the Outer Continental Shelf Waters and Coastal Regions of Alaska. Volume II. Bering Sea. alaska univ anchorage arctic environmental information and data center.

Burns, J.J., Shapiro, L.H. and Fay, F.H., 1981. Ice as marine mammal habitat in the Bering Sea. The eastern Bering Sea shelf: oceanography and resources, 2, pp.781-797.

Buzard, R., Maio, C.V., Kinsman, N., and Verbyla, D., 2020. Shoreline change analysis of Goodnews Bay, Alaska. Shore and Beach, 88(2), pp. 1-13.

Buzard, R.M., 2017. Spatiotemporal patterns of bluff erosion at Goodnews Bay, Alaska. University of Alaska Fairbanks. Master's thesis.

Cacchione, D.A. and Drake, D.E., 1979. A new instrument system to investigate sediment dynamics on continental shelves. Marine Geology, 30(3-4), pp.299-312.

Cazenave, A., Meyssignac, B., Ablain, M., Balmaseda, M., Bamber, J., Barletta, V., Beckley, B., Benveniste, J., Berthier, E., Blazquez, A. and Boyer, T., 2018. Global sea-level budget 1993-present. Earth System Science Data, 10(3), pp.1551-1590.

CE2 Engineers, Inc., 2002. Water system improvement plan, Nelson Lagoon, Alaska. Prepared for Nelson Lagoon Council.

Cooper, A.K., Marlow, M.S. and Scholl, D.W., 1976. Mesozoic magnetic lineations in the Bering Sea marginal basin. Journal of Geophysical Research, 81(11), pp.1916-1934.

Crowell, B.W. and Melgar, D., 2020. Slipping the Shumagin Gap: A kinematic coseismic and early afterslip model of the MW 7.8 Simeonof Island, Alaska, earthquake. Geophysical Research Letters, 47(19), p.e2020GL090308.

Crowell, M.; Leatherman, S.P., and Buckley, M.K., 1993. Shoreline change rate analysis: long term versus short term data. Shore and Beach, 61(2), 13–20.

da Silva, G.V., Muler, M., Prado, M.F., Short, A.D., da Fontoura Klein, A.H. and Toldo Jr, E.E., 2016. Shoreline change analysis and insight into the sediment transport path along Santa Catarina Island north shore, Brazil. Journal of Coastal Research, 32(4), pp.863-874.

Danielson, S., Curchitser, E., Hedstrom, K., Weingartner, T. and Stabeno, P., 2011. On ocean and sea-ice modes of variability in the Bering Sea. Journal of Geophysical Research: Oceans, 116(C12).

Davidson-Arnott, R., Bauer, B. and Houser, C., 2019. Introduction to coastal processes and geomorphology. Cambridge university press.

Davies, J., Sykes, L., House, L. and Jacob, K., 1981. Shumagin seismic gap, Alaska Peninsula: History of great earthquakes, tectonic setting, and evidence for high seismic potential. Journal of Geophysical Research: Solid Earth, 86(B5), pp.3821-3855.

Day, J.J. and Hodges, K.I., 2018. Growing land-sea temperature contrast and the intensification of Arctic cyclones. Geophysical Research Letters, 45(8), pp.3673-3681.

De Winter, R.C. and Ruessink, B.G., 2017. Sensitivity analysis of climate change impacts on dune erosion: case study for the Dutch Holland coast. Climatic Change, 141(4), pp.685-701.

Dean, B., Collins, I., Divoky, D., Hatheway, D. and Scheffner, C.N., 2005. FEMA Coastal Flood Hazard Analysis and Mapping Guidelines Focused Study Report.

Deltares, 2011. Tutorial SOBEK-Rural FLOW Module Workshop Ho Chi Minh City June 1-3, 2011. Deltares, Delft, The Netherlands.

Deltares, D., 2013. Delft3D-FLOW user manual.

Dissanayake, D.M.P.K., Ranasinghe, R.W.M.R.J.B. and Roelvink, J.A., 2012. The morphological response of large tidal inlet/basin systems to relative sea level rise. Climatic change, 113(2), pp.253-276.

Donnelly, C., Kraus, N. and Larson, M., 2006. State of knowledge on measurement and modeling of coastal overwash. Journal of coastal research, 22(4 (224)), pp.965-991.

Draper, S., Houlsby, G.T., Oldfield, M.L.G. and Borthwick, A.G.L., 2010. Modelling tidal energy extraction in a depth-averaged coastal domain. IET renewable power generation, 4(6), pp.545-554.

Dygas, J.A. and Burrell, D.C., 1976. Wind and current patterns in an arctic coast Lagoon. Ocean Engineering, 3(5), pp.317-327.

Elaksher, A., Kamtchang, F., Wegmann, C. and Guerrero, A., 2018. Assessing the quality of GEOID12B model through field surveys. Journal of Applied Geodesy, 12(1), pp.1-13.

Enríquez, A.R., Marcos, M., Falqués, A. and Roelvink, D., 2019. Assessing beach and dune erosion and vulnerability under sea level rise: a case study in the Mediterranean Sea. Frontiers in Marine Science, 6, p.4.

Erikson, L.H., Espejo, A., Barnard, P.L., Serafin, K.A., Hegermiller, C.A., O'Neill, A., Ruggiero, P., Limber, P.W. and Mendez, F.J., 2018. Identification of storm events and contiguous coastal sections for deterministic modeling of extreme coastal flood events in response to climate change. Coastal Engineering, 140, pp.316-330.

Erikson, L.H., McCall, R.T., Van Rooijen, A. and Norris, B., 2015. Hindcast storm events in the Bering Sea for the St. Lawrence Island and Unalakleet regions, Alaska (No. 2015-1193). US Geological Survey.

Escoffier, F.F., 2016. The stability of tidal inlets. United States Engineer Office Mobile United States.

Evans, O.F., 1942. The origin of spits, bars, and related structures. The Journal of Geology, 50(7), pp.846-865.

Farquharson, L.M., Mann, D.H., Swanson, D.K., Jones, B.M., Buzard, R.M. and Jordan, J.W., 2018. Temporal and spatial variability in coastline response to declining sea-ice in northwest Alaska. Marine Geology, 404, pp.71-83.

Fischer-Bruns, I., von Storch, H., González-Rouco, J.F. and Zorita, E., 2005. Modelling the variability of midlatitude storm activity on decadal to century time scales. Climate dynamics, 25(5), pp.461-476.

FitzGerald, D.M., Fenster, M.S., Argow, B.A. and Buynevich, I.V., 2008. Coastal impacts due to sea-level rise. Annual Review of Earth and Planetary Sciences, 36.

Fletcher, C.H., Richmond, B.M., Barnes, G.M. and Schroeder, T.A., 1995. Marine flooding on the coast of Kaua'i during Hurricane Iniki: hindcasting inundation components and delineating washover. Journal of Coastal Research, pp.188-204.

Fok, H.S., 2012. Ocean tides modeling using satellite altimetry (Doctoral dissertation, The Ohio State University).

Forbes, D.L., 2011. State of the Arctic coast 2010: scientific review and outlook. Land-Ocean Interactions in the Coastal Zone, Institute of Coastal Research.

Francis, J.A. and Vavrus, S.J., 2015. Evidence for a wavier jet stream in response to rapid Arctic warming. Environmental Research Letters, 10(1), p.014005.

Francis, J.A., Chen, Y., Miller, J.R. and Russell, G., 2011, December. Projected regime shift in arctic feedbacks. In AGU Fall Meeting Abstracts (Vol. 2011, pp. A31D-0107).

Frey, K.E., Moore, G.W.K., Cooper, L.W. and Grebmeier, J.M., 2015. Divergent patterns of recent sea-ice cover across the Bering, Chukchi, and Beaufort seas of the Pacific Arctic Region. Progress in Oceanography, 136, pp.32-49.

Fu, L.L. and Pihos, G., 1994. Determining the response of sea level to atmospheric pressure forcing using TOPEX/POSEIDON data. Journal of Geophysical Research: Oceans, 99(C12), pp.24633-24642.

Geng, Q. and Sugi, M., 2003. Possible change of extratropical cyclone activity due to enhanced greenhouse gases and sulfate aerosols—Study with a high-resolution AGCM. Journal of Climate, 16(13), pp.2262-2274.

Genz, A.S., Fletcher, C.H., Dunn, R.A., Frazer, L.N., and Rooney, J.J., 2007. The predictive accuracy of shoreline change rate methods and alongshore beach variation on Maui, Hawaii. Journal of Coastal Research, 23(1), 87–105.

Gesch, D. and Wilson, R., 2001. Development of a seamless multisource topographic/bathymetric elevation model of Tampa Bay. Marine Technology Society Journal, 35(4), pp.58-64.

Gibbs, A.E. and Richmond, B.M., 2015. National Assessment of Shoreline Change: Historical Shoreline Change along the North Coast of Alaska, US-Canadian Border to Icy Cape (p. 96). US Department of the Interior, US Geological Survey.

Gindraux, S., Boesch, R. and Farinotti, D., 2017. Accuracy assessment of digital surface models from unmanned aerial vehicles' imagery on glaciers. Remote Sensing, 9(2), p.186.

Glaeser, J.D., 1978. Global distribution of barrier islands in terms of tectonic setting. The Journal of Geology, 86(3), pp.283-297.

Gornitz, V., 1995. Sea-level rise: A review of recent past and near-future trends. Earth surface processes and landforms, 20(1), pp.7-20.

Graham, N.E. and Diaz, H.F., 2001. Evidence for intensification of North Pacific winter cyclones since 1948. Bulletin of the American Meteorological Society, 82(9), pp.1869-1894.

Green, M.O. and Coco, G., 2014. Review of wave-driven sediment resuspension and transport in estuaries. Reviews of Geophysics, 52(1), pp.77-117.

Gross, R.S., 2007. Earth rotation variations-long period. Treatise on geophysics, 3, pp.239-294.

Grow, J.A. and Atwater, T., 1970. Mid-Tertiary tectonic transition in the Aleutian arc. Geological Society of America Bulletin, 81(12), pp.3715-3722.

Haigh, I.D., Pickering, M.D., Green, J.M., Arbic, B.K., Arns, A., Dangendorf, S., Hill, D.F., Horsburgh, K., Howard, T., Idier, D. and Jay, D.A., 2020. The tides they are a-Changin': A comprehensive review of past and future nonastronomical changes in tides, their driving mechanisms, and future implications. Reviews of Geophysics, 58(1), p.e2018RG000636.

Hamilton, S. and Shennan, I., 2005. Late Holocene relative sea-level changes and the earthquake deformation cycle around upper Cook Inlet, Alaska. Quaternary Science Reviews, 24(12-13), pp. 1479-1498.

HDR, 2011. Nelson Lagoon Hazard Impact Study, Prepared for the Aleutians East Borough.

HDR, 2014a. Nelson Lagoon Coastal Erosion Study Numerical Hydrodynamic Model Technical Memorandum, Prepared for the Aleutians East Borough.

HDR, 2014b. Nelson Lagoon Coastal Erosion Study Numerical Wave Model Technical Memorandum, Prepared for the Aleutians East Borough.

HDR, 2014c. Nelson Lagoon Coastal Erosion Study Historical Shoreline Map Report, Prepared for the Aleutians East Borough.

HDR, 2015. Nelson Lagoon Shoreline Protection 20% Preliminary Design. Project No. 213165. Prepared for the Aleutians East Borough.

Herring, S.C., Christidis, N., Hoell, A., Kossin, J.P., Schreck III, C.J. and Stott, P.A., 2018. Explaining extreme events of 2016 from a climate perspective. Bulletin of the American Meteorological Society, 99(1), pp. S1-S157.

Himmelstoss, E.A., Henderson, R.E., Kratzmann, M.G. and Farris, A.S., 2018. Digital Shoreline Analysis System (DSAS) version 5.0 user guide (No. 2018-1179). US Geological Survey.

Hoskins, B.J. and Hodges, K.I., 2002. New perspectives on the Northern Hemisphere winter storm tracks. Journal of the Atmospheric Sciences, 59(6), pp.1041-1061.

Houser, C., Hapke, C. and Hamilton, S., 2008. Controls on coastal dune morphology, shoreline erosion and barrier island response to extreme storms. Geomorphology, 100(3-4), pp.223-240.

Hoyt, J.H., 1967. Barrier island formation. Geological Society of America Bulletin, 78(9), pp.1125-1136.

Hubertz, J.M., 1992. A users guide to the WIS wave model, Version 2.0, WIS report 27, U.S. Army Engineer Waterways Experiment Station, Vicksburg, MS.

Hume, J.D. and Schalk, M., 1967. Shoreline processes near Barrow, Alaska: a comparison of the normal and the catastrophic. Arctic, pp.86-103.

James, M.R., Robson, S. and Smith, M.W., 2017. 3-D uncertainty-based topographic change detection with structure-from-motion photogrammetry: precision maps for ground control and directly georeferenced surveys. Earth Surface Processes and Landforms, 42(12), pp.1769-1788.

Johnson, E.A., 1983. Textural and compositional sediment characteristics of the southeastern Bristol Bay continental shelf, Alaska (Doctoral dissertation, California State University, Northridge).

Jones, B.M., Arp, C.D., Jorgenson, M.T., Hinkel, K.M., Schmutz, J.A. and Flint, P.L., 2009. Increase in the rate and uniformity of coastline erosion in Arctic Alaska. Geophysical Research Letters, 36(3).

Jones, M.C., Berkelhammer, M., Keller, K.J., Yoshimura, K. and Wooller, M.J., 2020. High sensitivity of Bering Sea winter sea-ice to winter insolation and carbon dioxide over the last 5500 years. Science advances, 6(36), pp. 10.

Jones, S.C., Harr, P.A., Abraham, J., Bosart, L.F., Bowyer, P.J., Evans, J.L., Hanley, D.E., Hanstrum, B.N., Hart, R.E., Lalaurette, F. and Sinclair, M.R., 2003. The extratropical transition of tropical cyclones: Forecast challenges, current understanding, and future directions. Weather and Forecasting, 18(6), pp.1052-1092.

Jordan, J.W., 2001. Late Quaternary sea level change in Southern Beringia: postglacial emergence of the Western Alaska Peninsula. Quaternary Science Reviews, 20(1-3), pp.509-523.

Keegan, T.J., 1958. Arctic synoptic activity in winter. Journal of Atmospheric Sciences, 15(6), pp.513-521.

Kelly, J.T. and Gontz, A.M., 2018. Using GPS-surveyed intertidal zones to determine the validity of shorelines automatically mapped by Landsat water indices. International journal of applied earth observation and geoinformation, 65, pp.92-104.

Kelsey, H.M., Witter, R.C., Engelhart, S.E., Briggs, R., Nelson, A., Haeussler, P. and Corbett, D.R., 2015. Beach ridges as paleoseismic indicators of abrupt coastal subsidence during subduction zone earthquakes, and implications for Alaska-Aleutian subduction zone paleoseismology, southeast coast of the Kenai Peninsula, Alaska. Quaternary Science Reviews, 113, pp.147-158.

Kinder, T.H. and Schumacher, J.D., 1981. Circulation Over the Continental Shelf. The eastern Bering Sea shelf: oceanography and resources, 1, p.53.

Kinsman, N.E. and DeRaps, M.R., 2012. Coastal hazard field investigations in response to the November 2011 Bering Sea storm, Norton Sound, Alaska. Report of Investigations, p.2.

Kinsman, N.E. and Gould, A., 2014. Contemporary shoreline retreat rates at Meshik in Port Heiden, Alaska. State of Alaska, Department of Natural Resources, Division of Geological & Geophysical Surveys.

Kinsman, N.E., DeRaps, M.R. and Smith, J.R., 2013. Preliminary Evaluation of Coastal Geomorphology and Geohazards on" Kigiqtam Iglua," an Island Northeast of Shishmaref, Alaska. Alaska: Alaska Department of Natural Resources, Division of Geological & Geophysical Surveys.

Kraus, N.C., Larson, M. and Wise, R.A., 1998. Depth of closure in beach-fill design. Army engineer waterways experiment station coastal and hydraulics lab, Vicksburg, MS.

Laan, S., 2019. Understanding coastal dynamics at an ebb-tidal delta in the Wadden Sea: A case study of Schiermonnikoog NW with Delft3D Flexible Mesh. (Master's thesis).

Lantz, T.C., Moffat, N.D., Jones, B.M., Chen, Q. and Tweedie, C.E., 2020. Mapping exposure to flooding in three coastal communities on the North slope of Alaska using Airborne LiDAR. Coastal Management, 48(2), pp.96-117.

Laporte-Fauret, Q., Marieu, V., Castelle, B., Michalet, R., Bujan, S. and Rosebery, D., 2019. Low-cost UAV for high-resolution and large-scale coastal dune change monitoring using photogrammetry. Journal of Marine Science and Engineering, 7(3), p.63.

Leatherman, S.P., 1977. Barrier island dynamics: overwash processes and eolian transport. In Coastal Engineering 1976 (pp. 1958-1974).

Lesser, G.R., Roelvink, J.V., Van Kester, J.A.T.M. and Stelling, G.S., 2004. Development and validation of a three-dimensional morphological model. Coastal engineering, 51(8-9), pp.883-915.

Luijendijk, A.P., 2001. Validation, calibration and evaluation of Delft3D-FLOW model with ferry measurements. (Master's thesis).

Maio, C., Sullivan, R., Buzard, R., Bogardus, R., and Whitley, M., 2017. Protecting Cultural Resources through Geomorphological and Archeological Investigations in Kenai Fjords National Park, Geology Field Component Final Report. Kenai Fjords National Park, Seward, AK, p 83.

Mancini, F., Dubbini, M., Gattelli, M., Stecchi, F., Fabbri, S. and Gabbianelli, G., 2013. Using unmanned aerial vehicles (UAV) for high-resolution reconstruction of topography: The structure from motion approach on coastal environments. Remote sensing, 5(12), pp.6880-6898.

Marlow, M.S., Scholl, D.W., Cooper, A.K. and Buffington, E.C., 1976. Structure and evolution of Bering Sea shelf south of St. Lawrence Island. AAPG Bulletin, 60(2), pp.161-183.

Mason, O.K. and Jordan, J.W., 1993. Heightened North Pacific storminess during synchronous late Holocene erosion of Northwest Alaska beach ridges. Quaternary Research, 40(1), pp.55-69.

Mason, O.K., Salmon, D.K. and Ludwig, S.L., 1996. The periodicity of storm surges in the Bering Sea from 1898 to 1993, based on newspaper accounts. Climatic Change, 34(1), pp.109-123.

Matias, A., Ferreira, Ó., Vila-Concejo, A., Morris, B. and Dias, J.A., 2010. Short-term morphodynamics of non-storm overwash. Marine Geology, 274(1-4), pp.69-84.

McCabe, G.J., Clark, M.P. and Serreze, M.C., 2001. Trends in Northern Hemisphere surface cyclone frequency and intensity. Journal of Climate, 14(12), pp.2763-2768.

Mesquita, M.S., 2009. Characteristics and variability of storm tracks in the North Pacific, Bering Sea and Alaska (Doctoral dissertation).

Mesquita, M.S., Atkinson, D.E. and Hodges, K.I., 2010. Characteristics and variability of storm tracks in the North Pacific, Bering Sea, and Alaska. Journal of Climate, 23(2), pp.294-311.

Moritz, H., White, K., Gouldby, B., Sweet, W., Ruggiero, P., Gravens, M., O'Brien, P., Moritz, H., Wahl, T., Nadal-Caraballo, N.C. and Veatch, W., 2015, September. USACE adaptation approach for future coastal climate conditions. In Proceedings of the Institution of Civil Engineers-Maritime Engineering (Vol. 168, No. 3, pp. 111-117). Thomas Telford Ltd.

Morton, R.A. and Sallenger Jr, A.H., 2003. Morphological impacts of extreme storms on sandy beaches and barriers. Journal of Coastal Research, pp.560-573.

Morton, R.A., Ward, G.H. and White, W.A., 2000. Rates of sediment supply and sea-level rise in a large coastal lagoon. Marine Geology, 167(3-4), pp.261-284.

Muench, R.D. and Ahlnas, K., 1976. Ice movement and distribution in the Bering Sea from March to June 1974. Journal of Geophysical Research, 81(24), pp.4467-4476.

Nelson Lagoon SECD, Strategic economic plan, 2001. Prepared for the Native Village of Nelson Lagoon by Stadium Group, pp. 1-56

Nelson, A.R., 2007. Tectonics and relative sea-level change: tectonic locations. In: Elias, S.A. (Ed.), Encyclopedia of Quaternary Science, Elsevier, pp. 3072e3087

NOAA, National Oceanic and Atmospheric Administration, 2020. Data from: Water Levels - NOAA Tides, and Currents. Silver Spring, MD: NOAA.

Osswald, F., Dolch, T. and Reise, K., 2019. Remobilizing stabilized island dunes for keeping up with sea level rise?. Journal of Coastal Conservation, 23(3), pp.675-687.

Overbeck, J., Buzard, R. and Maio, C., 2017, September. Storm impacts in western alaska documenting shoreline change and flooding through remote sensing and community-based monitoring. In Oceans 2017-Anchorage (pp. 1-6). IEEE.

Overbeck, J.R., 2017. Storm Water Level Feature Extraction from Digital Elevation Models Using Intra-storm Photographs. Report of Investigations, p.6.

Overbeck, J.R., Buzard, R.M., Turner, M.M., Miller, K.Y., and Glenn, R.J., 2020, Shoreline change at Alaska coastal communities: Alaska Division of Geological & Geophysical Surveys Report of Investigation 2020-10, 29 p., 47 sheets.

Overbeck, J.R., ed., 2018, Alaska coastal mapping gaps & priorities: Alaska Division of Geological & Geophysical Surveys Information Circular 72, 34 p.

Overeem, I., Anderson, R.S., Wobus, C.W., Clow, G.D., Urban, F.E. and Matell, N., 2011. Sea-ice loss enhances wave action at the Arctic coast. Geophysical Research Letters, 38(17).

Overland, J.E. and Pease, C.H., 1982. Cyclone climatology of the Bering Sea and its relation to sea-ice extent. Monthly Weather Review, 110(1), pp.5-13.

Overland, J.E. and Wang, M., 2019. Impact of the winter polar vortex on greater North America. International Journal of Climatology, 39(15), pp.5815-5821.

Overland, J.E., Adams, J.M. and Bond, N.A., 1999. Decadal variability of the Aleutian low and its relation to high-latitude circulation. Journal of Climate, 12(5), pp.1542-1548.

Overland, J.E., Wood, K.R. and Wang, M., 2011. Warm Arctic—cold continents: climate impacts of the newly open Arctic Sea. Polar Research, 30(1), p.15787.

Pajak, M.J. and Leatherman, S., 2002. The high water line as shoreline indicator. Journal of Coastal Research, pp.329-337.

Plafker, G., 1969. Tectonics of the March 27, 1964, Alaska earthquake: Chapter I in The Alaska earthquake, March 27, 1964: regional effects (No. 543-I). US Government Printing Office.

Rachold, V., Are, F.E., Atkinson, D.E., Cherkashov, G. and Solomon, S.M., 2005. Arctic coastal dynamics (ACD): An introduction. Geo-Marine Letters, 25(2-3), pp.63-68.

Reimnitz, E. and Maurer, D.K., 1979. Effects of storm surges on the Beaufort Sea coast, northern Alaska. Arctic, pp.329-344.

Reimnitz, E., Dethleff, D. and Nürnberg, D., 1994. Contrasts in Arctic shelf sea-ice regimes and some implications: Beaufort Sea versus Laptev Sea. Marine Geology, 119(3-4), pp.215-225.

Rinke, A. and Dethloff, K., 2008. Simulated circum-Arctic climate changes by the end of the 21st century. Global and Planetary Change, 62(1-2), pp.173-186.

Rodionov, S.N., Bond, N.A. and Overland, J.E., 2007. The Aleutian Low, storm tracks, and winter climate variability in the Bering Sea. Deep Sea Research Part II: Topical Studies in Oceanography, 54(23-26), pp.2560-2577.

Rodionov, S.N., Overland, J.E. and Bond, N.A., 2005. The Aleutian low and winter climatic conditions in the Bering Sea. Part I: Classification. Journal of Climate, 18(1), pp.160-177.

Romine, B.M.; Fletcher, C.H.; Frazer, L.N.; Genz, A.S.; Barbee, M.M., and Lim, S.-C., 2009. Historical shoreline change, southeast Oahu, Hawaii; applying polynomial models to calculate shoreline change rates. Journal of Coastal Research, 25(6), 1236–1253.

Roos, P.C., Schuttelaars, H.M. and Brouwer, R.L., 2013. Observations of barrier island length explained using an exploratory morphodynamic model. Geophysical research letters, 40(16), pp.4338-4343.

Ruggiero, P., Holman, R.A. and Beach, R.A., 2004. Wave run-up on a high-energy dissipative beach. Journal of Geophysical Research: Oceans, 109(C6).

Ruggiero, P., Komar, P.D., McDougal, W.G., Marra, J.J. and Beach, R.A., 2001. Wave run-up, extreme water levels and the erosion of properties backing beaches. Journal of coastal research, pp.407-419.

Ruggiero, P., Kratzmann, M.G., Himmelstoss, E.A., Reid, D., Allan, J. and Kaminsky, G., 2013. National assessment of shoreline change: historical shoreline change along the Pacific Northwest coast. US Geological Survey.

Sallenger Jr, A.H., 2000. Storm impact scale for barrier islands. Journal of Coastal Research, pp.890-895.

Sallenger Jr, A.H., Howard, P.C., Fletcher III, C.H. and Howd, P.A., 1983. A system for measuring bottom profile, waves and currents in the high-energy nearshore environment. Marine Geology, 51(1-2), pp.63-76.

Schuenemann, K.C. and Cassano, J.J., 2010. Changes in synoptic weather patterns and Greenland precipitation in the 20th and 21st centuries: 2. Analysis of 21st century atmospheric changes using self-organizing maps. Journal of Geophysical Research: Atmospheres, 115(D5).

Sepp, M. and Jaagus, J., 2011. Changes in the activity and tracks of Arctic cyclones. Climatic Change, 105(3), pp.577-595.

Serreze, M.C., 1995. Climatological aspects of cyclone development and decay in the Arctic. Atmosphere-Ocean, 33(1), pp.1-23.

Shapiro, L.H. and Burns, J.J., 1975. Satellite observations of sea-ice movement in the Bering Strait region. Climate of the Arctic, pp.379-386.

Sharma, G.D., Naidu, A.S. and Hood, D.W., 1972. Bristol Bay: model contemporary graded shelf. AAPG Bulletin, 56(10), pp.2000-2012.

Shennan, I., Barlow, N., Carver, G., Davies, F., Garrett, E. and Hocking, E., 2014. Great tsunamigenic earthquakes during the past 1000 yr on the Alaska megathrust. Geology, 42(8), pp.687-690.

Shugar, D.H., Walker, I.J., Lian, O.B., Eamer, J.B., Neudorf, C., McLaren, D. and Fedje, D., 2014. Post-glacial sea-level change along the Pacific coast of North America. Quaternary Science Reviews, 97, pp.170-192.

Silva, R.A.G., Gallo, M.N., Rosman, P.C.C. and Nogueira, I.C.M., 2020. Tidal inlet short-term morphodynamics analysed trough the tidal prism-longshore sediment transport ratio criterion. Geomorphology, 351, p.106918.

Smith, J.R., 2014. Patterns and potential solutions to coastal geohazards at Golovin, Alaska (Master's thesis).

Soler, T., Weston, N.D. and Foote, R.H., 2011. The "Online Positioning User Service" Suite. CORS and OPUS for Engineers: Tools for Surveying and Mapping Applications, p.17.

Sorteberg, A. and Walsh, J.E., 2008. Seasonal cyclone variability at 70 N and its impact on moisture transport into the Arctic. Tellus A: Dynamic Meteorology and Oceanography, 60(3), pp.570-586.

Spargo, E., Hess, K., Myers, E., Yang, Z. and Wong, A., 2006. Tidal datum modeling in support of NOAA's vertical datum transformation tool. In Estuarine and Coastal Modeling (2005) (pp. 523-536).

Stabeno, P.J., Bond, N.A. and Salo, S.A., 2007. On the recent warming of the southeastern Bering Sea shelf. Deep Sea Research Part II: Topical Studies in Oceanography, 54(23-26), pp.2599-2618.

Stabeno, P.J., Bond, N.A., Kachel, N.B., Salo, S.A. and Schumacher, J.D., 2001. On the temporal variability of the physical environment over the south-eastern Bering Sea. Fisheries Oceanography, 10(1), pp.81-98.

Stabeno, P.J., Farley Jr, E.V., Kachel, N.B., Moore, S., Mordy, C.W., Napp, J.M., Overland, J.E., Pinchuk, A.I. and Sigler, M.F., 2012. A comparison of the physics of the northern and southern shelves of the eastern Bering Sea and some implications for the ecosystem. Deep Sea Research Part II: Topical Studies in Oceanography, 65, pp.14-30.

Stabeno, P.J., Schumacher, J.D. and Ohtani, K., 1999. The physical oceanography of the Bering Sea. Dynamics of the Bering Sea, pp.1-28.

Stockdon, H.F., Holman, R.A., Howd, P.A. and Sallenger Jr, A.H., 2006. Empirical parameterization of setup, swash, and run-up. Coastal engineering, 53(7), pp.573-588.

Strauss, B.H., Ziemlinski, R., Weiss, J.L. and Overpeck, J.T., 2012. Tidally adjusted estimates of topographic vulnerability to sea level rise and flooding for the contiguous United States. Environmental Research Letters, 7(1), p.014033.

Suleimani, E.N., Nicolsky, D.J., and Salisbury, J.B., 2020, Regional tsunami hazard assessment for communities of Bristol Bay and the Pribilof Islands, Alaska: Alaska Division of Geological & Geophysical Surveys Report of Investigation 2020-1, 32 p., 6 sheets.

Terenzi, J., Jorgenson, M.T., Ely, C.R. and Giguère, N., 2014. Storm-surge flooding on the Yukon-Kuskokwim delta, Alaska. Arctic, pp.360-374.

Thoman, R. & J. E. Walsh., 2019. Alaska's changing environment: documenting Alaska's physical and biological changes through observations. H. R. McFarland, Ed. International Arctic Research Center, University of Alaska Fairbanks.

Thoman, R.L., Bhatt, U.S., Bieniek, P.A., Brettschneider, B.R., Brubaker, M., Danielson, S., Labe, Z., Lader, R., Meier, W.N., Sheffield, G. and Walsh, J.E., 2020. The record low Bering sea-ice extent in 2018: context, impacts, and an assessment of the role of anthropogenic climate change.

Thomson, J. and Rogers, W.E., 2014. Swell and sea in the emerging Arctic Ocean. Geophysical Research Letters, 41(9), pp.3136-3140.

Thomson, J., Fan, Y., Stammerjohn, S., Stopa, J., Rogers, W.E., Girard-Ardhuin, F., Ardhuin, F., Shen, H., Perrie, W., Shen, H. and Ackley, S., 2016. Emerging trends in the sea state of the Beaufort and Chukchi seas. Ocean Modelling, 105, pp.1-12.

Titus, J.G. and Richman, C., 2001. Maps of lands vulnerable to sea level rise: modeled elevations along the US Atlantic and Gulf coasts. Climate Research, 18(3), pp.205-228.

Tran, T.T., van de Kreeke, J., Stive, M.J. and Walstra, D.J.R., 2012. Cross-sectional stability of tidal inlets: A comparison between numerical and empirical approaches. Coastal Engineering, 60, pp.21-29.

Trenberth, K.E. and Hurrell, J.W., 1994. Decadal atmosphere-ocean variations in the Pacific. Climate Dynamics, 9(6), pp.303-319.

Tschetter, T., Kinsman, N.E. and Fish, A., 2014. Color-indexed elevation maps for flood-vulnerable coastal communities in western Alaska. State of Alaska, Department of Natural Resources, Division of Geological & Geophysical Surveys.

U.S. General Accounting Office (GAO), 2003. Alaska Native villages—Most are affected by flooding and erosion, but few qualify for federal assistance. U.S. General Accounting Office Report GAO-04-142, 82p.

USACE, United States Army Corps of Engineers., 2007. Alaska baseline erosion assessment, erosion information paper – Nelson Lagoon, Alaska.

USACE, United States Army Corps of Engineers., 2019. Statewide threat assessment: identification of threats from erosion, flooding, and thawing permafrost in remote Alaska communities. Report #INE 19.03. Prepared for the Denali Commission, pp.1-99

Van de Sande, B., Lansen, J. and Hoyng, C., 2012. Sensitivity of coastal flood risk assessments to digital elevation models. Water, 4(3), pp.568-579.

Van Goor, M.A., Zitman, T.J., Wang, Z.B. and Stive, M.J.F., 2003. Impact of sea-level rise on the morphological equilibrium state of tidal inlets. Marine Geology, 202(3-4), pp.211-227.

Vermaire, J.C., Pisaric, M.F., Thienpont, J.R., Courtney Mustaphi, C.J., Kokelj, S.V. and Smol, J.P., 2013. Arctic climate warming and sea-ice declines lead to increased storm surge activity. Geophysical Research Letters, 40(7), pp.1386-1390.

Wallace, J.M. and Hobbs, P.V., 1979. Atmospheric Science (Book Review). Astrophysical Letters, 20, p.28.

Watanabe, Y. and Kawahara, Y., 2016. UAV photogrammetry for monitoring changes in river topography and vegetation. Procedia Engineering, 154, pp.317-325.

WEAR, Waste Erosion Assessment and Review., 2015. Detailed action plan Nelson Lagoon landfill, 6 p.

Weaver, R.J., 2008. Storm surge: influence of bathymetric fluctuations and barrier islands on coastal water levels. University of Florida.

Weeks, W.F. and Weller, G., 1984. Offshore oil in the Alaskan Arctic. Science, 225(4660), pp.371-378.

Wendler, G., Moore, B. and Galloway, K., 2014. Strong temperature increase and shrinking sea-ice in Arctic Alaska. The Open Atmospheric Science Journal, 8(1).

Whittaker, L.M. and Horn, L.H., 1984. Northern Hemisphere extratropical cyclone activity for four mid-season months. Journal of Climatology, 4(3), pp.297-310.

Wilson, F.H., Hults, C.P., Mull, C.G, and Karl, S.M, comps., 2015, Geologic map of Alaska: U.S. Geological Survey Scientific Investigations Map 3340, pamphlet 196 p., 2 sheets, scale 1:1,584,000, http://dx.doi.org/10.3133/sim3340.

WMO, World Meteorological Organization. Commission for Maritime Meteorology, 1970. The Beaufort Scale of Wind Force: (technical and operational Aspects) (No. 3).

Wuebbles, D.J., Fahey, D.W., Hibbard, K.A., Arnold, J.R., DeAngelo, B., Doherty, S., Easterling, D.R., Edmonds, J., Edmonds, T., Hall, T. and Hayhoe, K., 2017. Climate science special report: Fourth national climate assessment (NCA4), Volume I.

Yin, J.H., 2005. A consistent poleward shift of the storm tracks in simulations of 21st century climate. Geophysical Research Letters, 32(18).

Yunus, A.P., Avtar, R., Kraines, S., Yamamuro, M., Lindberg, F. and Grimmond, C.S.B., 2016. Uncertainties in tidally adjusted estimates of sea level rise flooding (bathtub model) for the greater London. Remote Sensing, 8(5), p.366.

Zhang, J., Woodgate, R. and Moritz, R., 2010. Sea-ice response to atmospheric and oceanic forcing in the Bering Sea. Journal of physical oceanography, 40(8), pp.1729-1747.

Zhang, X., Walsh, J.E., Zhang, J., Bhatt, U.S. and Ikeda, M., 2004. Climatology and interannual variability of Arctic cyclone activity: 1948–2002. Journal of climate, 17(12), pp.2300-2317.

APPENDICES

Appendix A: GCP Processing Report

Table A.1 Error between GCPs and the point cloud in the X, Y, and Z dimensions. Point name, total error, and pixel error is also provided.

Label	X error (m)	Y error (m)	Z error (m)	Total (m)	Image (pix)
NLG_GC_001	2.87136	0.627778	-0.096154	2.94076	0.656 (12)
NLG_GC_002	1.63429	-0.281545	-0.294264	1.68427	0.751 (40)
NLG_GC_004	-0.545085	-0.755136	-0.190233	0.950545	0.914 (39)
NLG_GC_006	-1.27792	-0.0179133	-0.515791	1.3782	0.983 (23)
NLG_GC_007	-1.1133	-0.168067	-0.238398	1.15088	1.342 (20)
NLG_GC_008	-1.39254	1.28103	-0.423217	1.9389	0.560 (23)
NLG_GC_009	-0.648167	1.42262	-0.00420786	1.56332	0.973 (36)
NLG_GC_011	-0.243307	1.70735	0.483551	1.79111	0.594 (15)
NLG_GC_012	-1.03612	0.481132	0.20311	1.1603	0.954 (54)
NLG_GC_013	-0.726173	-0.377883	0.263213	0.859886	0.985 (16)
NLG_GC_014	-0.558008	-0.562501	-0.159447	0.80821	0.909 (24)
NLG_GC_015	-0.397006	-0.778102	-0.144446	0.885393	1.198 (51)
NLG_GC_017	-0.145057	-1.02121	-0.27186	1.06668	1.807 (44)
NLG_GC_018	0.535957	-0.585354	-0.0734059	0.797043	0.901 (44)
NLG_GC_038	0.110013	-0.063411	0.219826	0.253865	0.467 (21)
NLG_GC_039	-0.052635	-0.276661	0.25976	0.383128	0.530 (23)
NLG_GC_040	-0.568387	-0.0922461	0.529937	0.782564	0.590 (23)
NLG_GC_041	-1.3535	0.652286	-0.23818	1.52124	0.507 (22)
NLG_GC_043	-0.681542	0.297485	0.325688	0.811831	1.312 (19)
NLG_GC_044	-0.555055	0.132356	0.551449	0.793536	1.328 (16)
NLG_GC_045	-0.255524	-0.294691	0.289908	0.485985	0.500 (24)
NLG_GC_046	-0.0473445	-0.280154	0.0801976	0.295228	0.529 (24)
NLG_GC_047	0.0130674	-0.243196	0.0184071	0.244242	0.451 (20)
NLG_GC_048	-0.0364909	-0.188514	0.0572314	0.200361	0.507 (18)
NLG_GC_049	0.511117	-0.16466	-0.326967	0.628697	0.497 (21)
NLG_GC_050	0.634706	-0.189081	-0.553427	0.863067	0.537 (18)
NLG_GC_052	-0.698422	0.932266	0.0791105	1.16755	1.560 (20)
NLG_GC_054	-0.806031	0.645788	0.615371	1.20225	1.407 (29)
NLG_GC_056	-0.546853	0.141941	-0.326256	0.65241	1.108 (18)
NLG_GC_057	-0.213667	-0.160088	-0.350147	0.440324	0.892 (31)
NLG_GC_058	-0.231556	0.118354	-0.0834628	0.273115	0.895 (27)

Table A.1 continued…

Label	X error (m)	Y error (m)	Z error (m)	Total (m)	Image (pix)
NLG_GC_060	0.273341	0.677332	0.36903	0.818338	0.264 (8)
NLG_GC_066	-0.476301	0.0849091	-0.173627	0.514022	0.839 (25)
NLG_GC_093	-0.12654	0.0875162	0.154432	0.217992	0.576 (19)
NLG_GC_094	-0.234288	0.316792	-0.0706572	0.4003	0.286 (22)
NLG_GC_096	-0.278112	0.314699	0.0487025	0.422793	0.293 (23)
NLG_GC_097	-0.319636	0.230781	-0.035885	0.395872	0.316 (27)
NLG_GC_098	0.260936	-0.229526	-0.0785094	0.356277	0.458 (18)
NLG_GC_20	-0.300611	-0.569262	0.00628376	0.64379	1.980 (56)
NLG_GC_21	-0.327259	-0.568332	0.285813	0.715394	0.935 (52)
NLG_GC_23	-0.41361	-0.265568	0.397908	0.6324	0.914 (24)
NLG_GC_24	-0.266254	0.637728	0.363614	0.780899	0.761 (46)
NLG_GC_25	-0.741958	0.183332	0.261547	0.807787	0.927 (35)
NLG_GC_27	0.654317	0.0243246	0.0194399	0.655057	0.061 (14)
NLG_GC_28	0.0131823	-0.139495	-0.370184	0.395814	0.563 (4)
NLG_GC_29	-0.043368	-0.0847966	0.15631	0.183042	0.820 (32)
NLG_GC_30	0.0478856	0.0579007	0.224894	0.237113	1.070 (30)
NLG_GC_31	-0.185669	-0.178709	-0.0570022	0.26393	0.966 (31)
NLG_GC_33	0.954042	0.191998	0.0893006	0.977258	0.128 (22)
NLG_GC_34	0.775132	0.0579623	-0.0610291	0.779688	0.150 (18)
NLG_GC_35	0.422822	-0.185246	-0.181717	0.4961	0.252 (23)
NLG_GC_36	0.187289	-0.214215	0.0494512	0.288809	0.340 (16)
NLG_GC_37	0.119834	-0.0975434	-0.0182691	0.155591	0.210 (17)
NLG_GC_38	-0.32113	-0.230111	-0.290117	0.490146	0.085 (25)
NLG_GC_39	-0.293527	-0.382291	-0.484851	0.683656	0.538 (23)
NLG_GC_40	-0.36074	-0.051801	-0.226127	0.428894	0.520 (30)
NLG_GC_67	-0.692809	0.152923	0.00884316	0.709541	0.290 (17)
NLG_GC_69	-0.708819	0.136931	0.165055	0.740552	0.059 (12)
NLG_GC_70	-0.592681	-0.0240074	-0.0333185	0.594102	0.029 (16)
NLG_GC_71	-0.270649	-0.206823	0.0554486	0.34511	0.015 (14)
NLG_GC_72	0.35727	-0.207784	-0.10773	0.427108	0.119 (21)
NLG_GC_73	0.475988	-0.132246	-0.107996	0.505684	0.096 (22)
NLG_GC_74	0.0187829	-0.288565	0.0635186	0.296069	0.141 (20)

Table A.1 continued…

Label	X error (m)	Y error (m)	Z error (m)	Total (m)	Image (pix)
NLG_GC_75	-0.407086	-0.0786513	0.0672464	0.420032	0.024 (22)
NLG_GC_76	-0.344384	0.00885545	0.0351433	0.346286	0.252 (16)
NLG_GC_77	-0.0054483	-0.266966	-0.102844	0.286143	0.179 (18)
NLG_GC_78	0.143733	-0.336031	0.0979399	0.378375	0.366 (24)
NLG_GC_79	0.0970996	-0.413119	-0.0973825	0.435407	0.324 (17)
NLG_GC_80	0.214321	-0.666811	-0.266404	0.749361	0.228 (15)
NLG_GC_81	0.21159	-0.378992	-0.0549931	0.437527	0.397 (23)
NLG_GC_82	0.112012	-0.0569398	-0.0996454	0.160368	0.337 (22)
NLG_GC_83	0.267112	-0.0190785	0.0769947	0.278642	0.935 (21)
NLG_GC_85	0.0433244	0.0554841	0.0779556	0.105036	0.609 (21)
NLG_GC_86	0.0546418	0.163283	0.162554	0.236793	0.651 (17)
NLG_GC_87	-0.2796	0.167409	0.108692	0.343534	0.663 (19)
NLG_GC_88	0.0720456	0.265683	0.0881588	0.28905	0.733 (21)
NLG_GC_89	-0.370641	0.46809	-0.131399	0.61135	0.324 (12)
NLG_GC_90	0.0825449	-0.0851793	0.0624564	0.134052	0.448 (24)
NLG_GC_101	-0.0546845	0.100256	-0.105519	0.155487	0.251 (14)
NLG_GC_104	-0.227287	0.0791158	-0.0331089	0.24293	0.375 (19)
NLG_GC_105	-0.0399521	-0.03955	-0.0841839	0.101229	0.296 (30)
NLG_GC_106	0.0557696	0.0684406	0.087754	0.124479	0.276 (30)
NLG_GC_107	0.102059	-0.13553	-0.113651	0.204208	0.356 (24)
NLG_GC_108	0.313387	0.00551084	0.111222	0.332584	0.437 (18)
NLG_GC_109	0.079847	0.203882	-0.0108404	0.219228	0.131 (12)
NLG_GC_110	-0.086501	0.0542828	0.0539612	0.115503	0.124 (15)
NLG_GC_111	-0.0398576	-0.0622562	0.00494288	0.0740871	0.085 (19)
NLG_GC_112	0.0459899	0.0599415	-0.0293629	0.081057	0.087 (20)
NLG_GC_117	-0.00566544	-0.330014	0.00590492	0.330115	0.022 (4)
NLG_GC_118	-0.0118011	0.0723172	-0.0412734	0.0840983	0.296 (20)
NLG_GC_119	0.00597044	0.123399	-0.0992785	0.15849	0.517 (18)
NLG_GC_120	0.0111868	0.312085	0.137955	0.3414	0.204 (17)
NLG_GC_121	-0.0744705	0.135332	0.00715069	0.154634	0.385 (17)
NLG_GC_122	-0.0566826	0.0278	0.114763	0.130982	0.517 (16)
NLG_GC_123	0.130783	-0.341601	-0.12655	0.387053	0.219 (19)

Table A.1 continued…

Label	X error (m)	Y error (m)	Z error (m)	Total (m)	Image (pix)
NLG_GC_125	-0.376106	-0.254985	0.0857891	0.462421	0.281 (10)
NLG_GC_126	0.414644	-0.406826	0.0517228	0.583191	0.478 (16)
NLG_GC_129	0.427855	-0.307363	-0.0994559	0.536119	0.522 (25)
NLG_GC_130	-0.915409	-0.238352	-0.0480606	0.947151	0.273 (27)
NLG_GCP18_0006	0.171584	1.02388	-0.385291	1.10735	1.412 (17)
NLG_GCP18_0007	0.169104	0.459509	0.438772	0.657469	1.401 (18)
NLG_GCP18_0009	0.102475	-0.654119	0.312221	0.732021	3.178 (52)
NLG_GCP18_0010	-0.2175	-0.280787	0.348103	0.497316	2.273 (17)
NLG_GCP18_0012	-0.0795184	-0.303274	-0.00231036	0.313534	1.028 (18)
NLG_GCP18_0020	1.90286	-0.966662	-0.105383	2.13692	0.977 (32)
NLG_GCP18_030	-0.140795	0.878796	-0.118043	0.897797	0.778 (21)
NLG_GCP18_039	0.0608653	-0.128649	0.55239	0.57043	1.248 (26)
NLG_GCP18_042	0.226913	0.209812	0.0683977	0.316526	1.058 (16)
NLG_GCP18_062	-0.950789	0.884484	0.224662	1.31787	1.865 (29)
NLG_GCP18_0004	0.793715	1.23037	-0.242605	1.48414	1.979 (20)
NLG_GCP18_0005	0.833403	1.13503	-0.0593223	1.40939	0.960 (24)
NLG_GCP18_0008	0.684033	0.100088	0.0916576	0.697366	3.028 (37)
NLG_GCP18_049	7.92614	-2.85636	-0.165342	8.42674	14.899 (31)
A001	-0.587065	0.142947	-0.293229	0.671612	1.304 (32)
A002	-0.208709	0.0756795	-0.471975	0.521581	1.227 (26)
A003	-0.523492	0.0941736	-0.723515	0.89799	0.844 (30)
A004	-0.2154	0.229936	-0.294748	0.431444	0.960 (34)
A005	0.678111	-0.265295	0.8097	1.08896	0.733 (26)
Total	**0.933214**	**0.527753**	**0.250227**	**1.10092**	**1.881**

Appendix B: Cross-shore Elevation Profiles

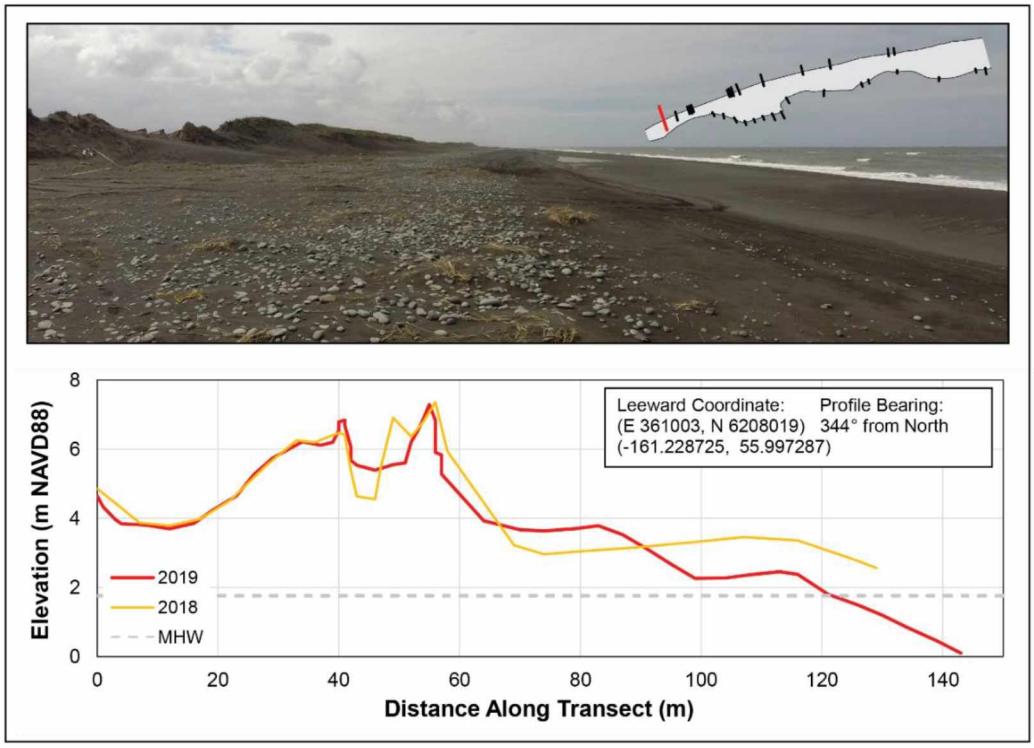

Figure B.1 Elevation profile A. Inset map denotes transect location.

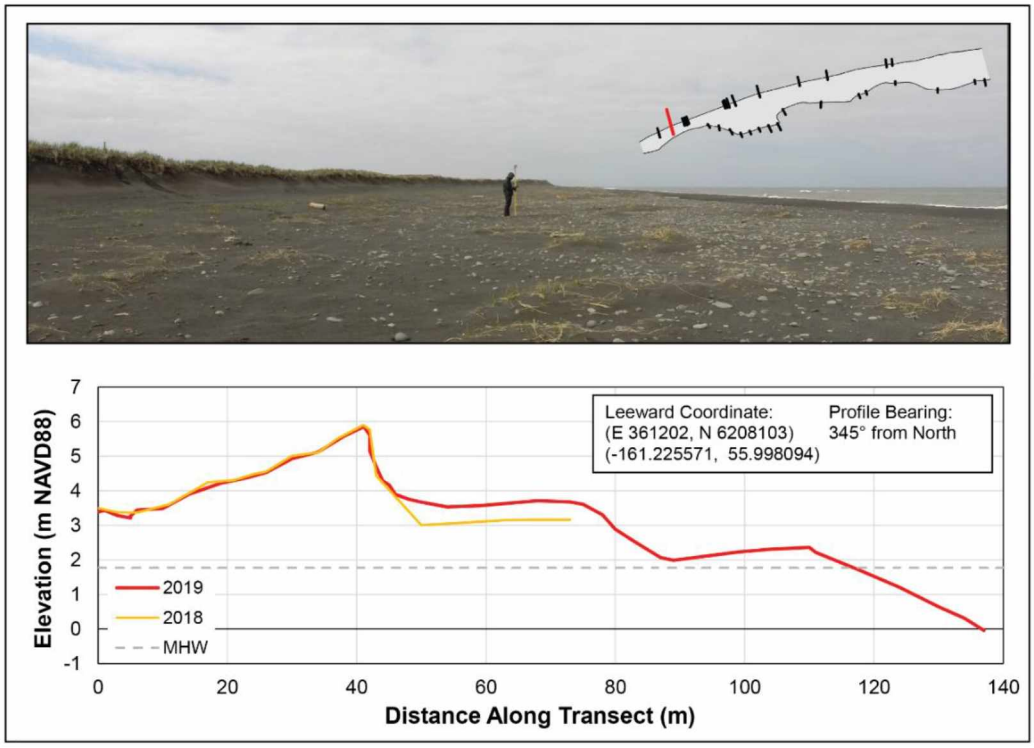

Figure B.2 Elevation profile B. Inset map denotes transect location.

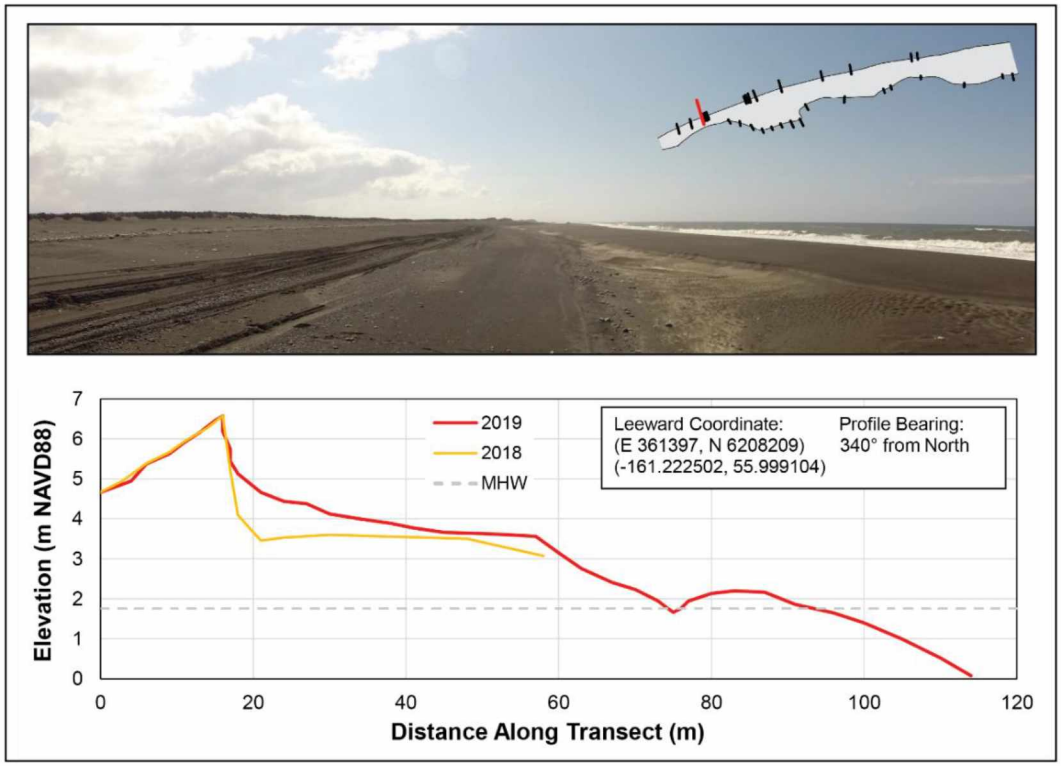

Figure B.3 Elevation profile C. Inset map denotes transect location.

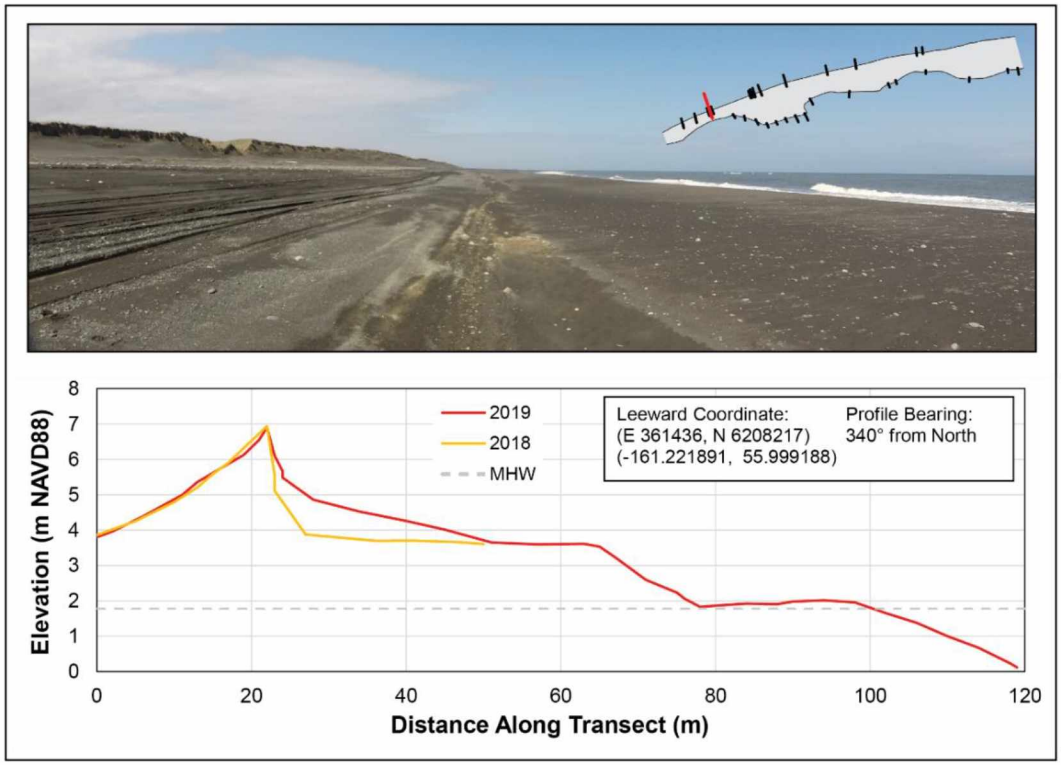

Figure B.4 Elevation profile D. Inset map denotes transect location.

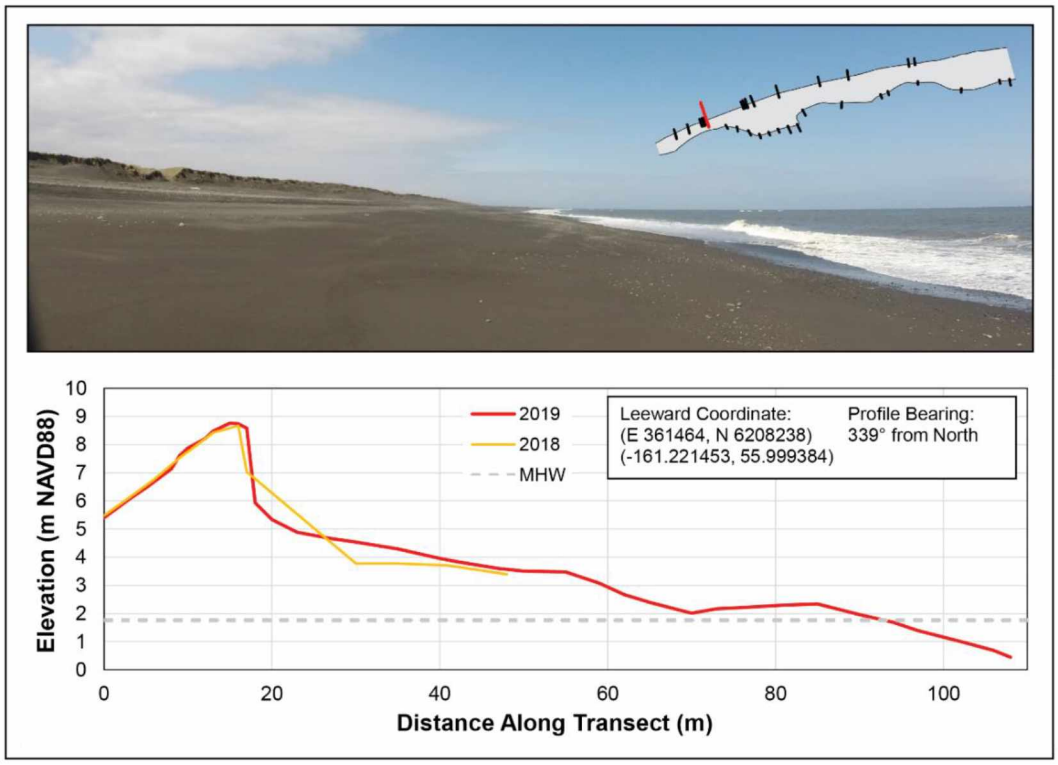

Figure B.5 Elevation profile E. Inset map denotes transect location.

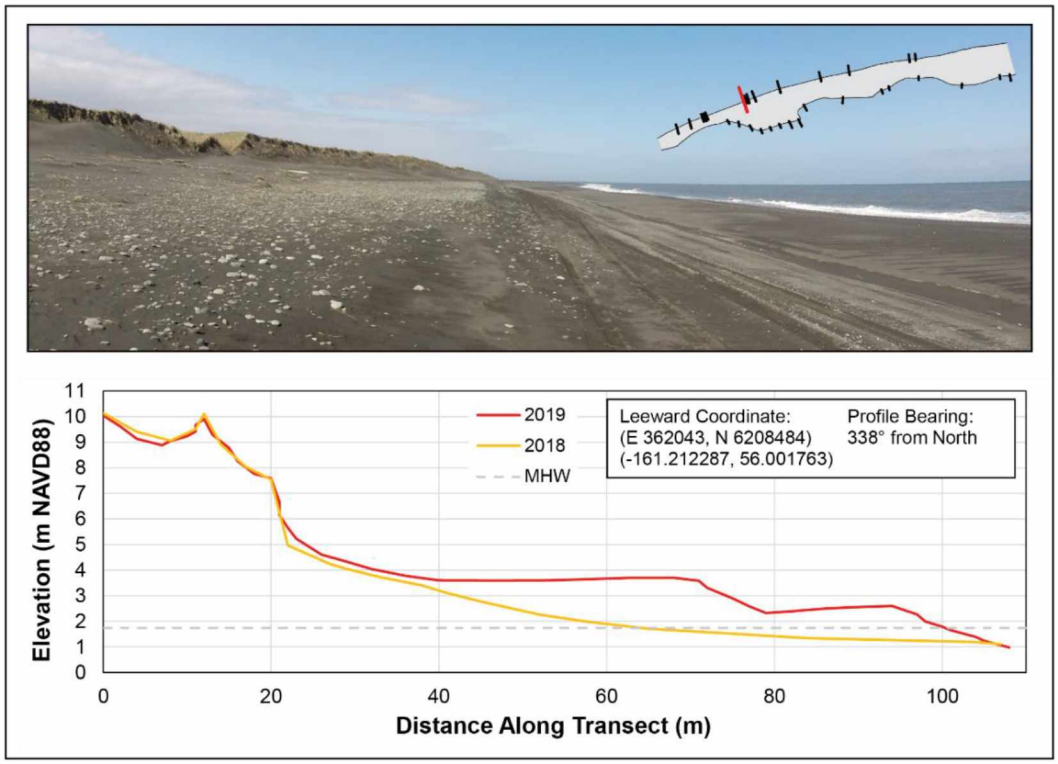

Figure B.6 Elevation profile F. Inset map denotes transect location.

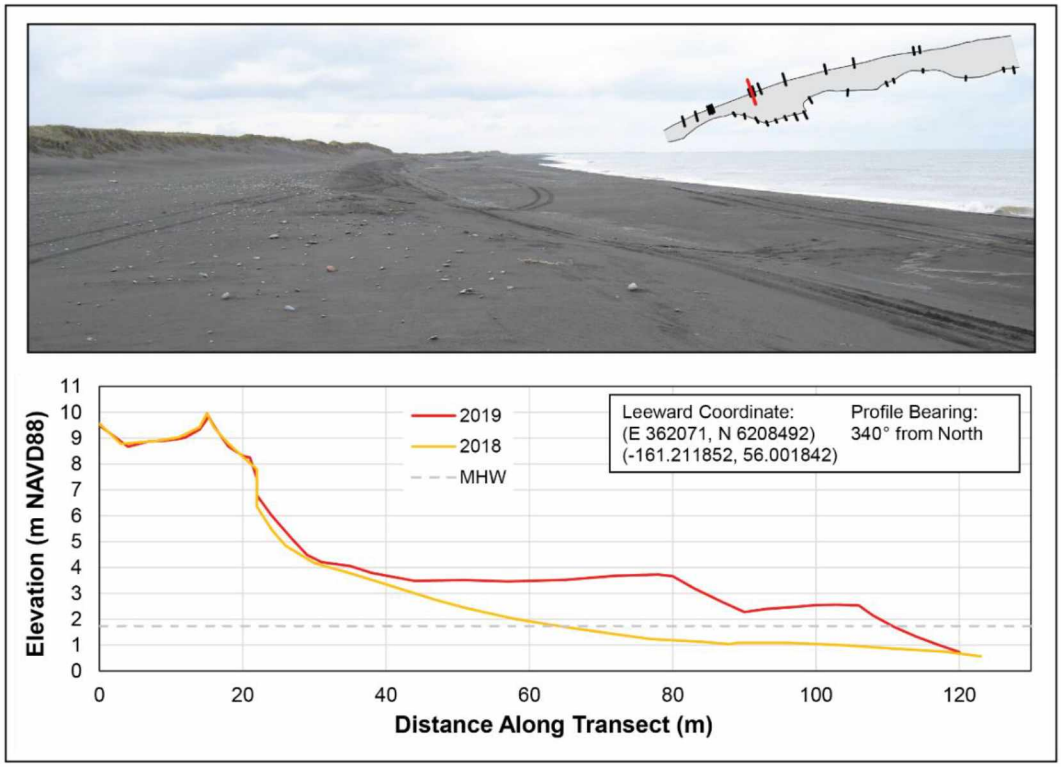

Figure B.7 Elevation profile G. Inset map denotes transect location.

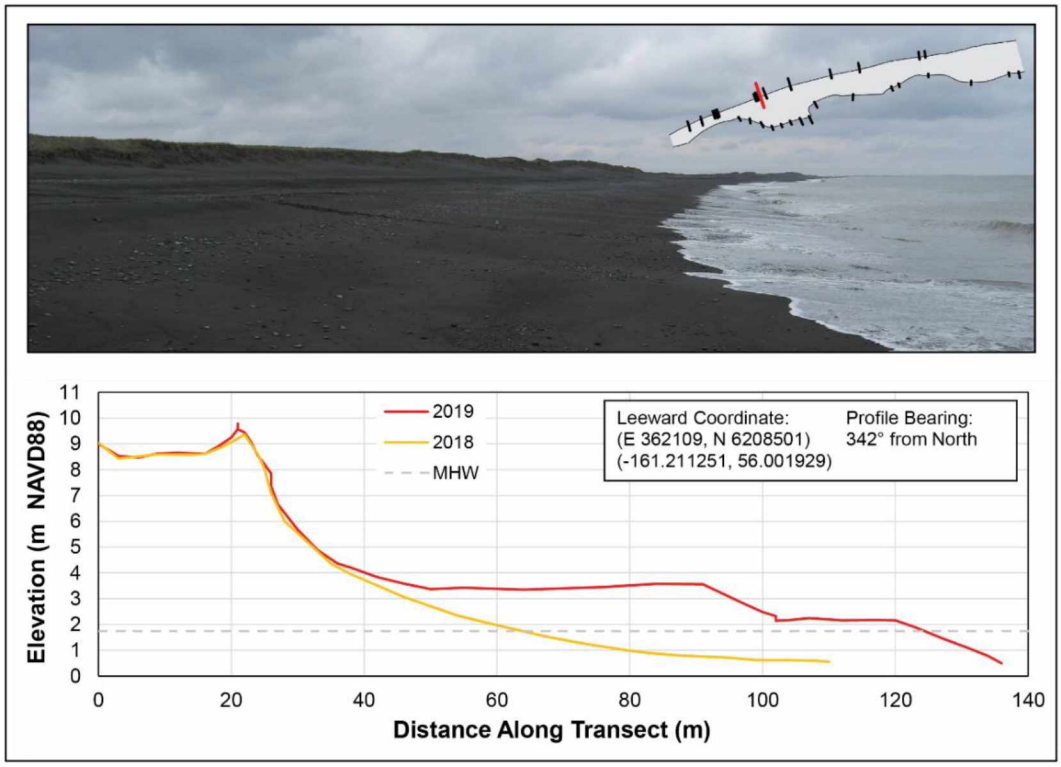

Figure B.8 Elevation profile H. Inset map denotes transect location.

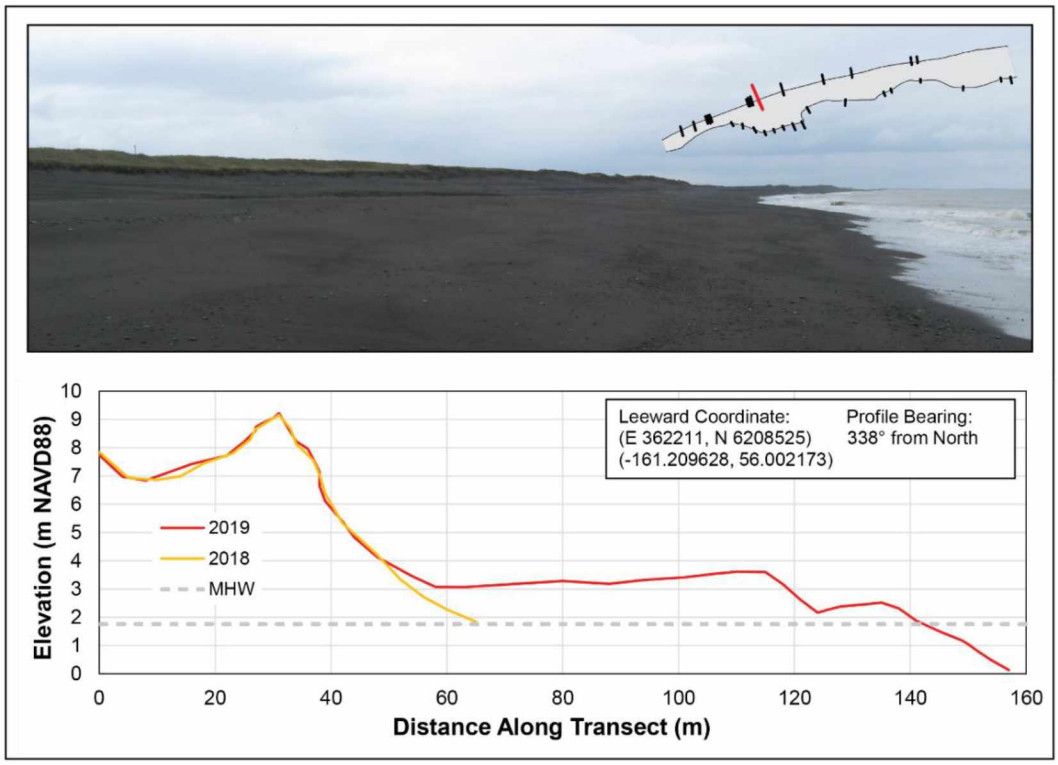

Figure B.9 Elevation profile I. Inset map denotes transect location.

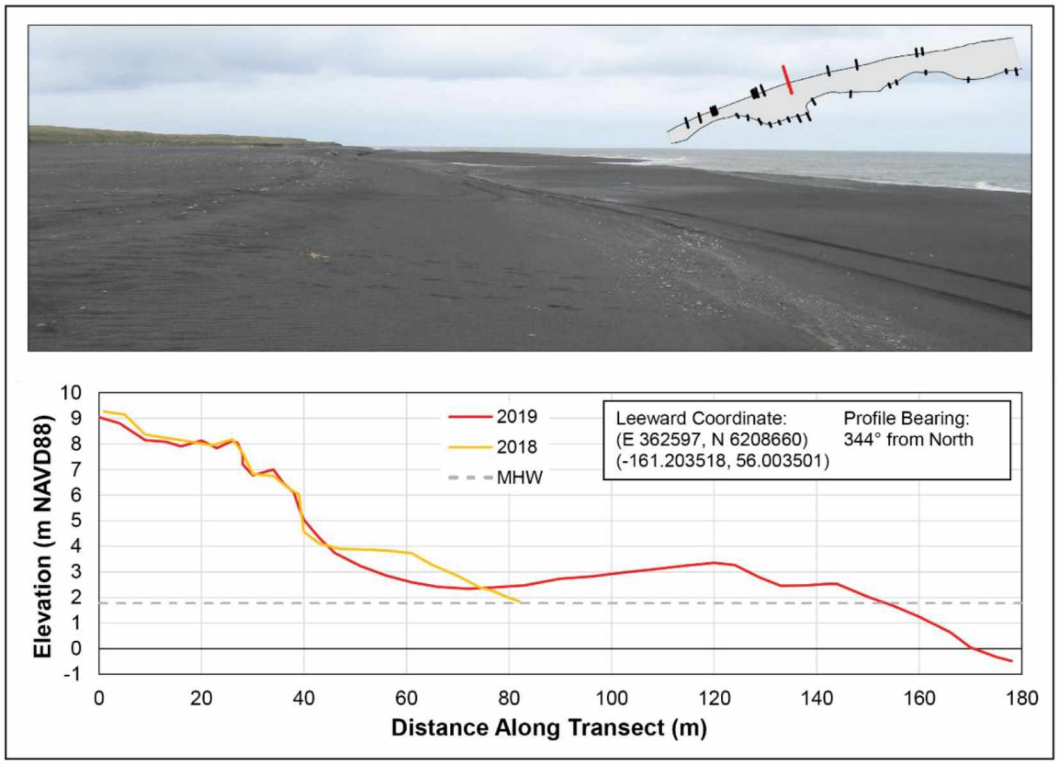

Figure B.10 Elevation profile J. Inset map denotes transect location.

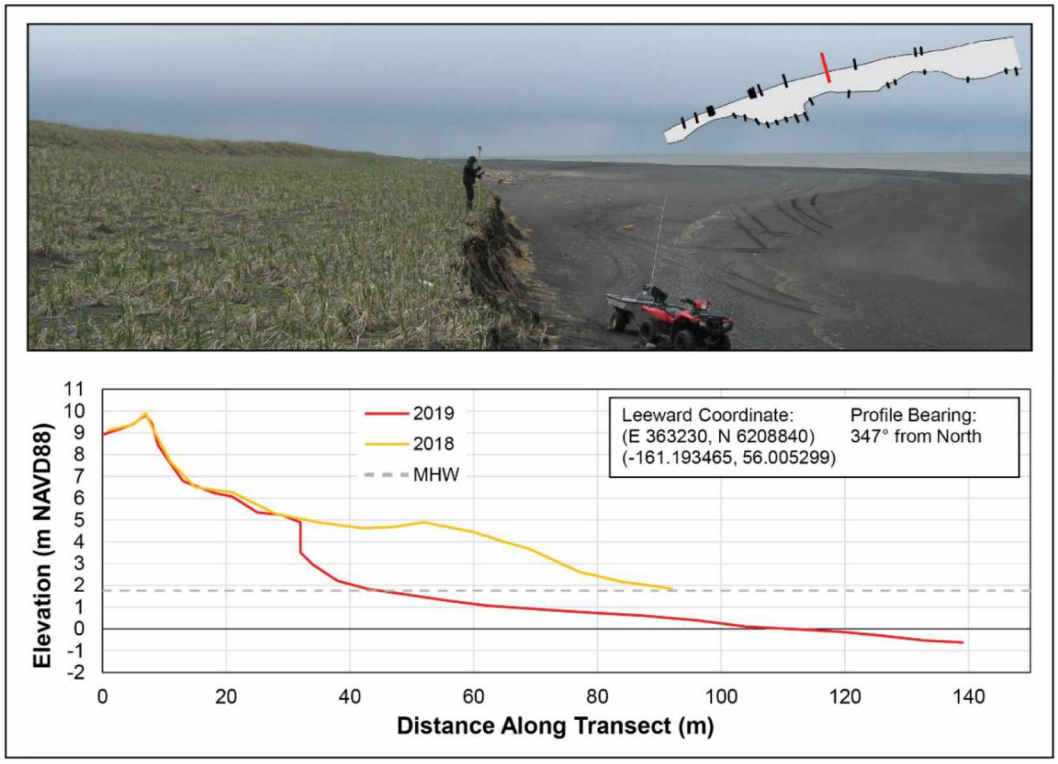

Figure B.11 Elevation profile K. Inset map denotes transect location.

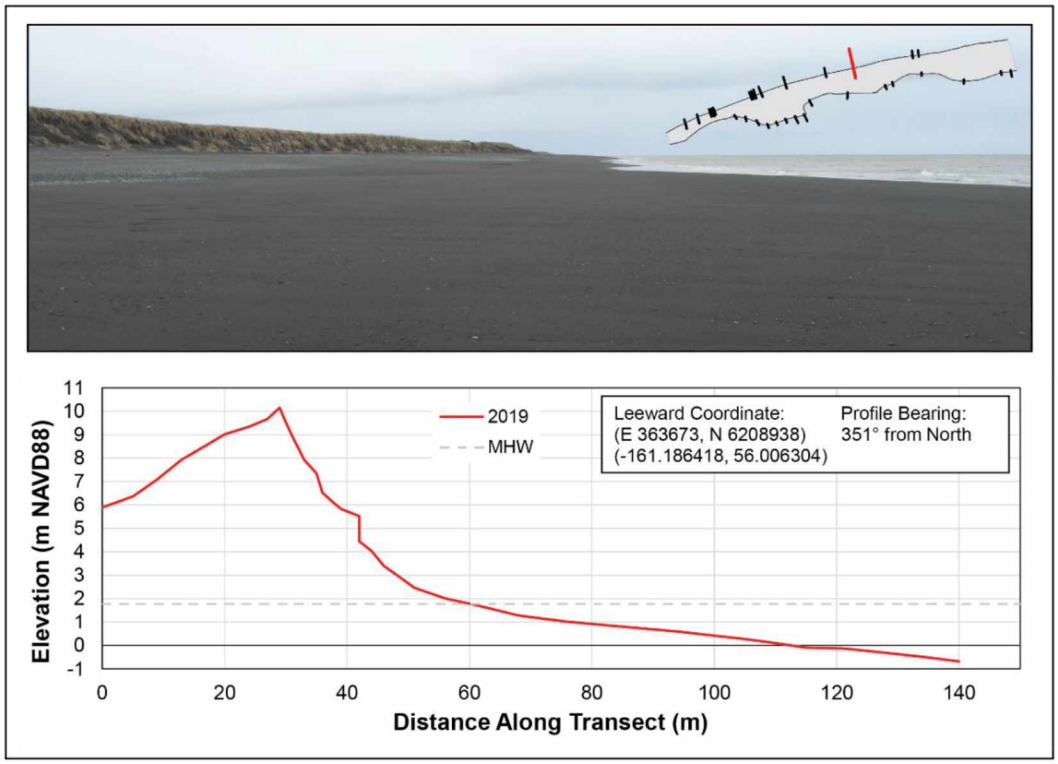

Figure B.12 Elevation profile L. Inset map denotes transect location.

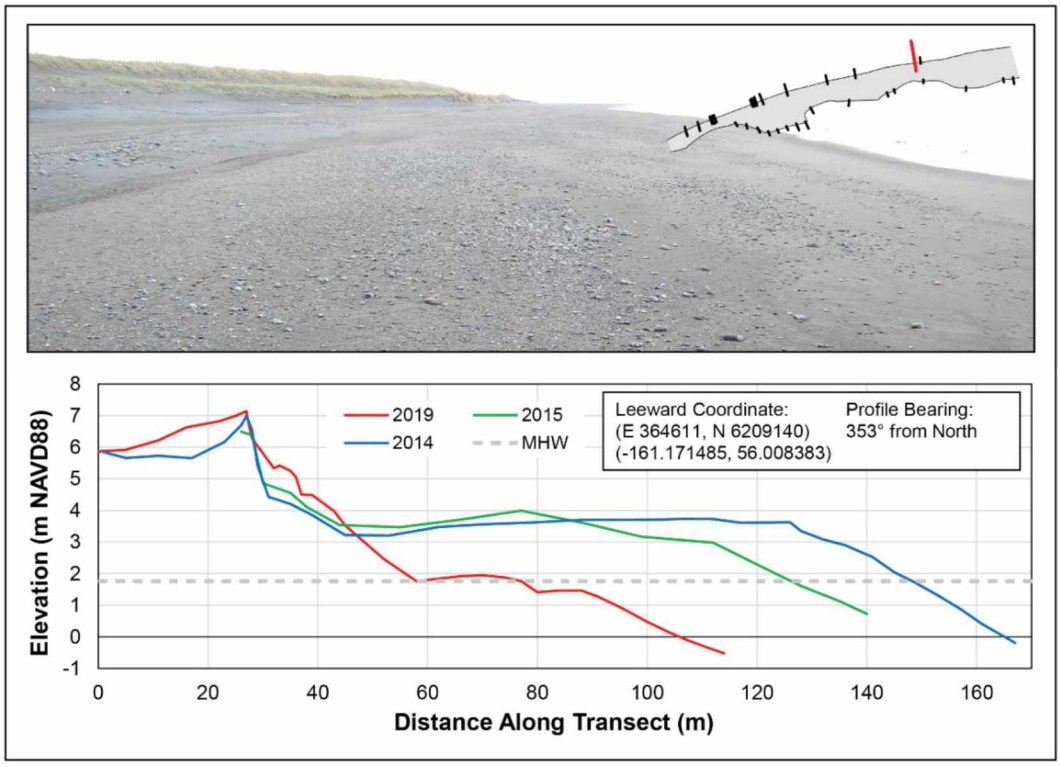

Figure B.13 Elevation profile M. Inset map denotes transect location.

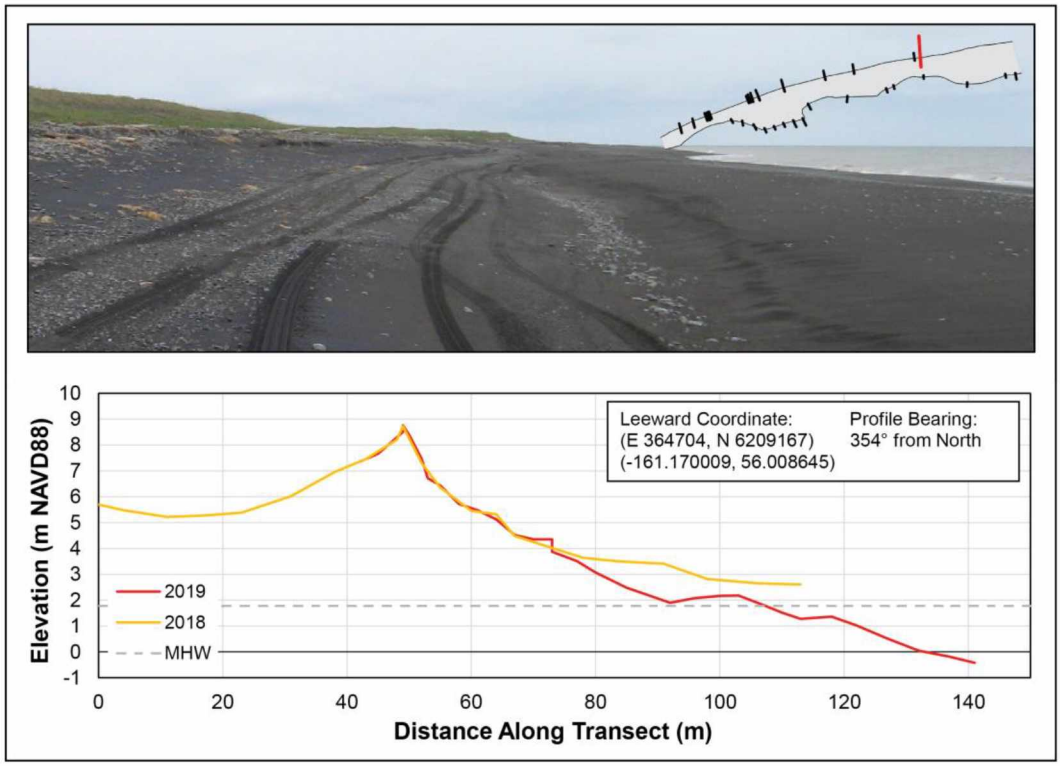

Figure B.14 Elevation profile N. Inset map denotes transect location.

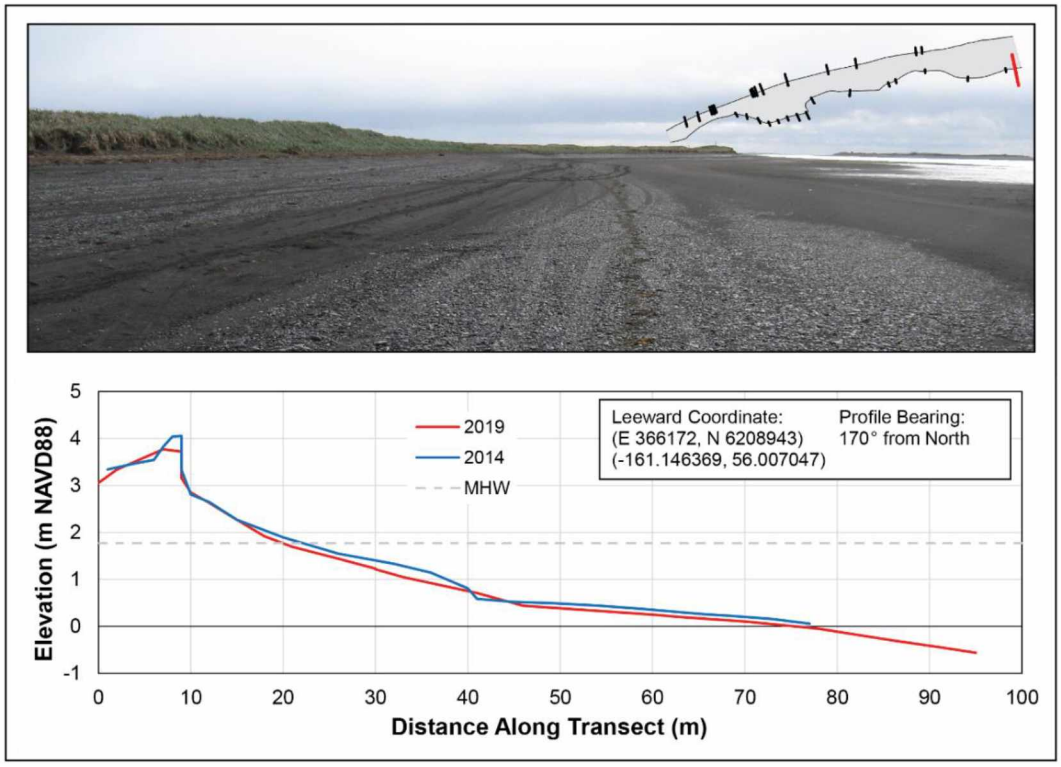

Figure B.15 Elevation profile O. Inset map denotes transect location.

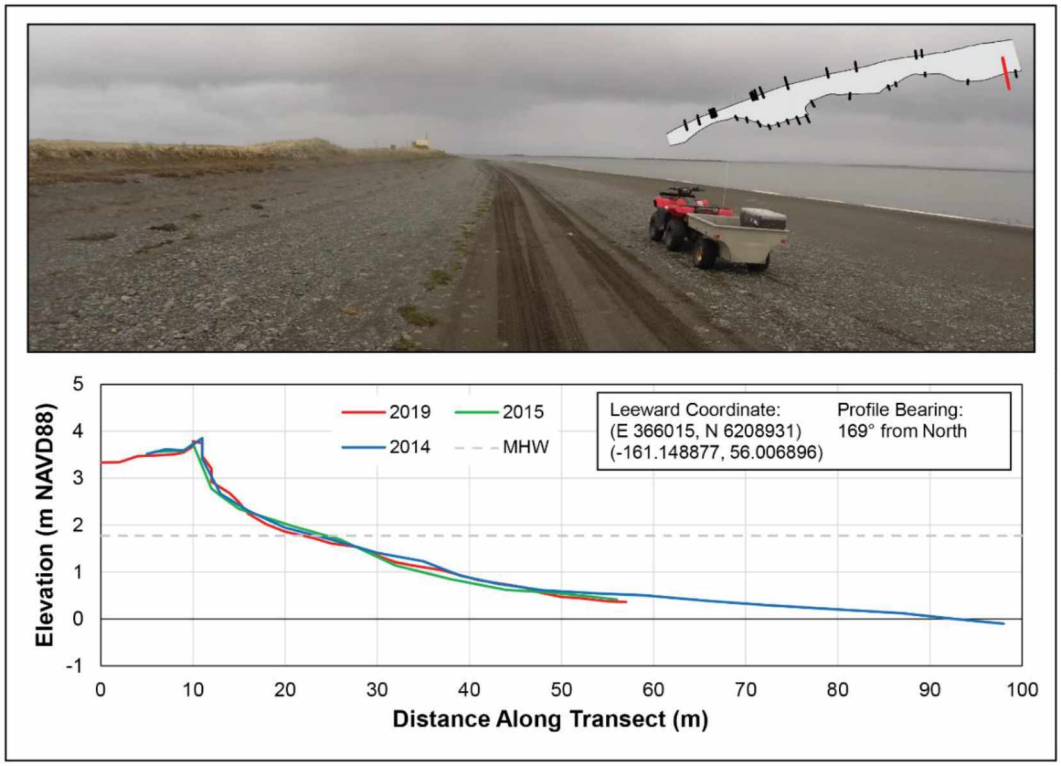

Figure B.16 Elevation profile P. Inset map denotes transect location.

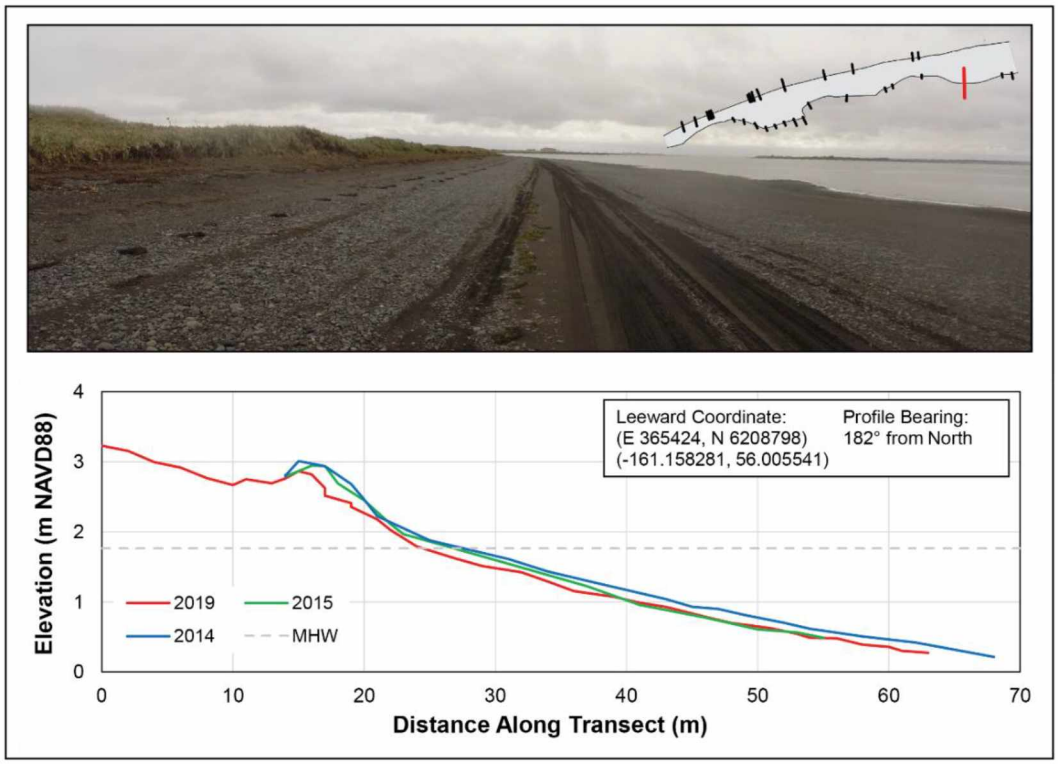

Figure B.17 Elevation profile Q. Inset map denotes transect location.

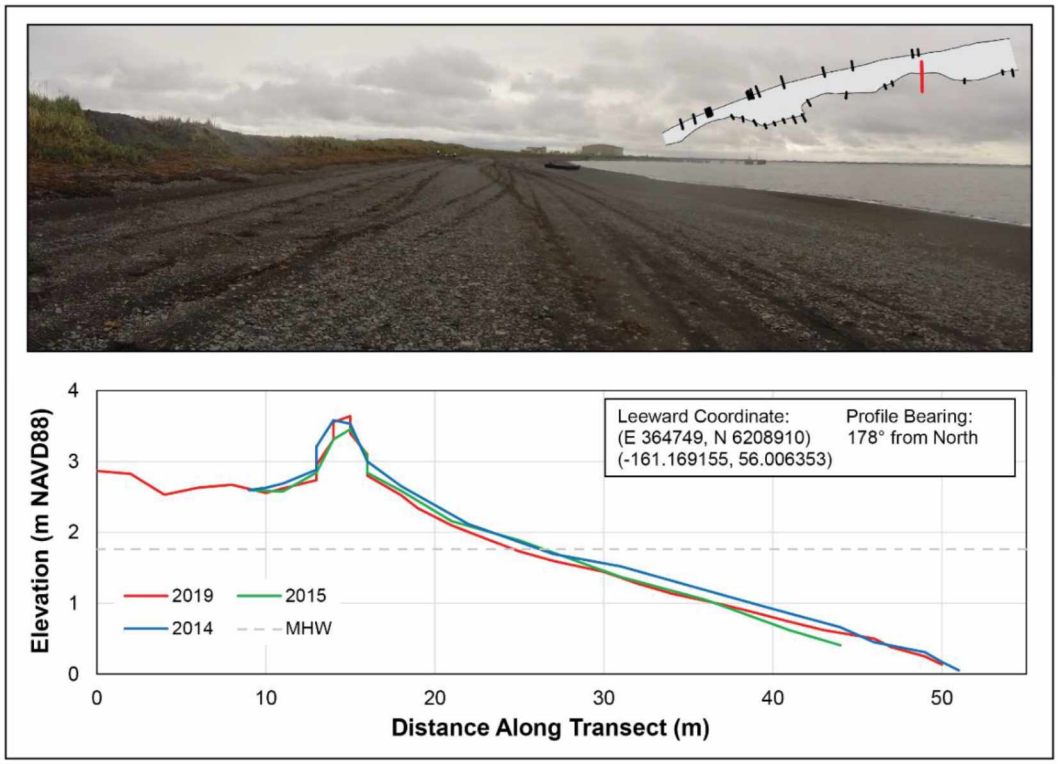

Figure B.18 Elevation profile R. Inset map denotes transect location.

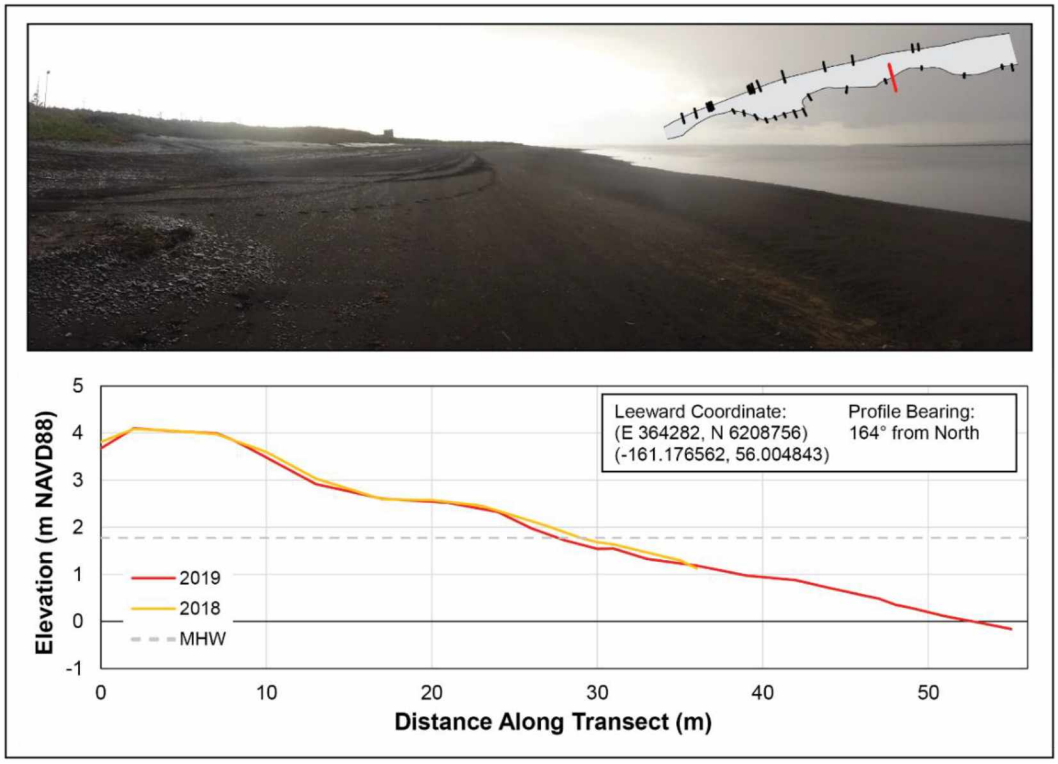

Figure B.19 Elevation profile S. Inset map denotes transect location.

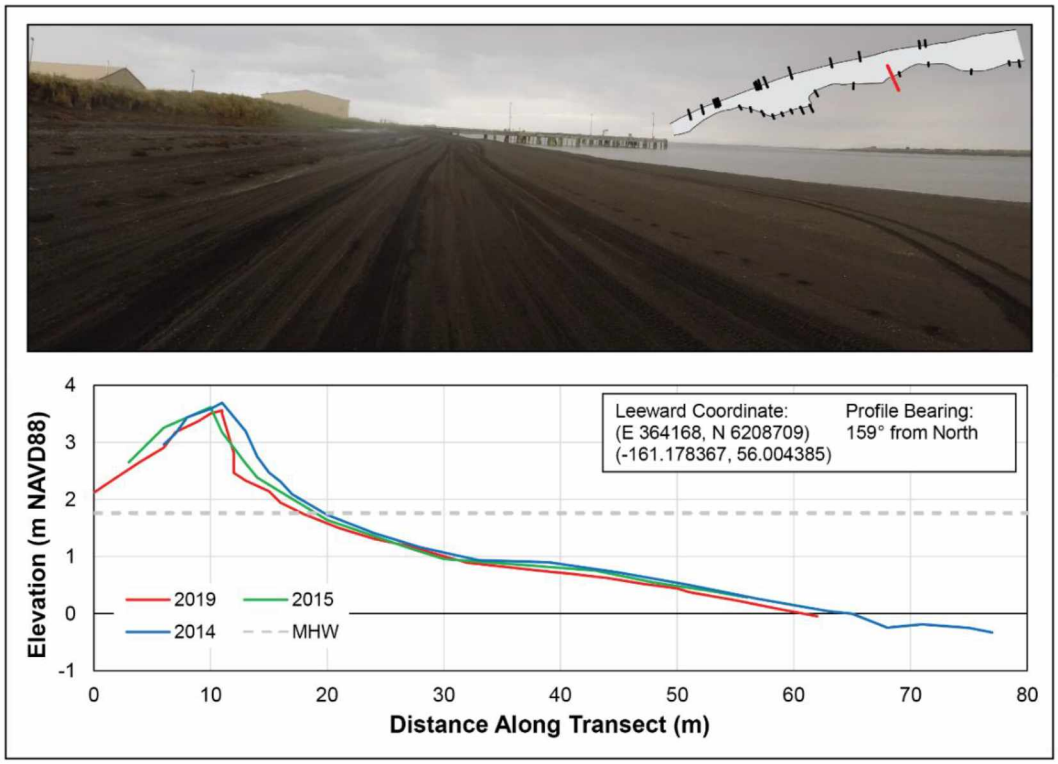

Figure B.20 Elevation profile T. Inset map denotes transect location.

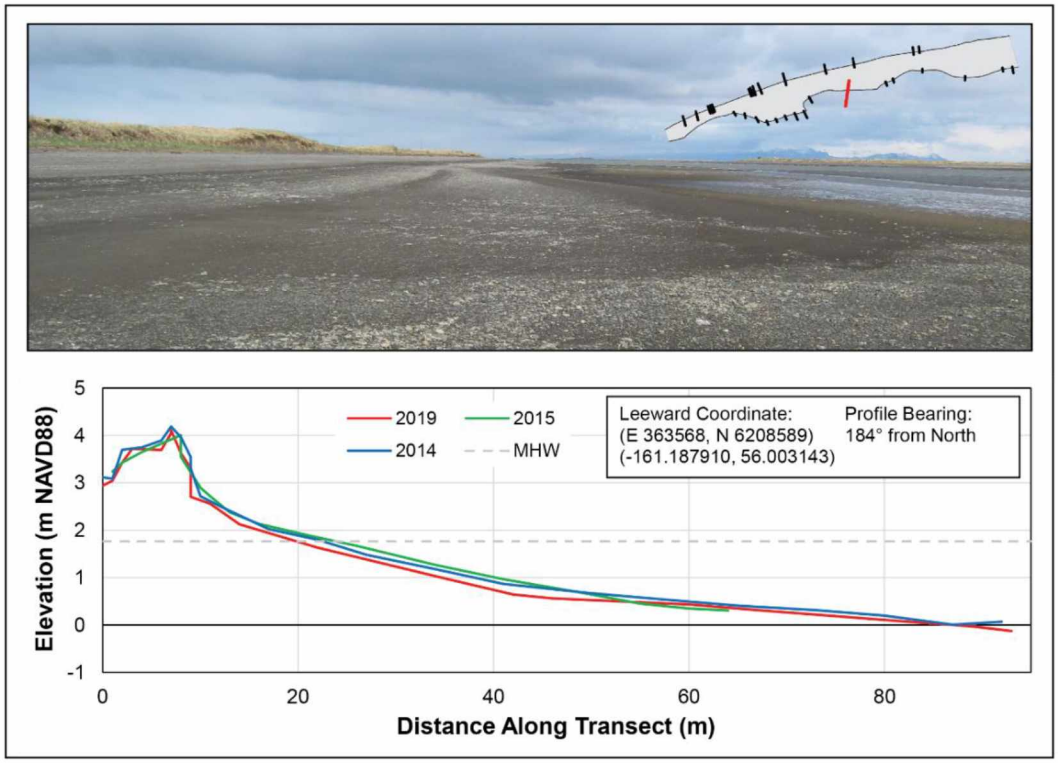

Figure B.21 Elevation profile U. Inset map denotes transect location.

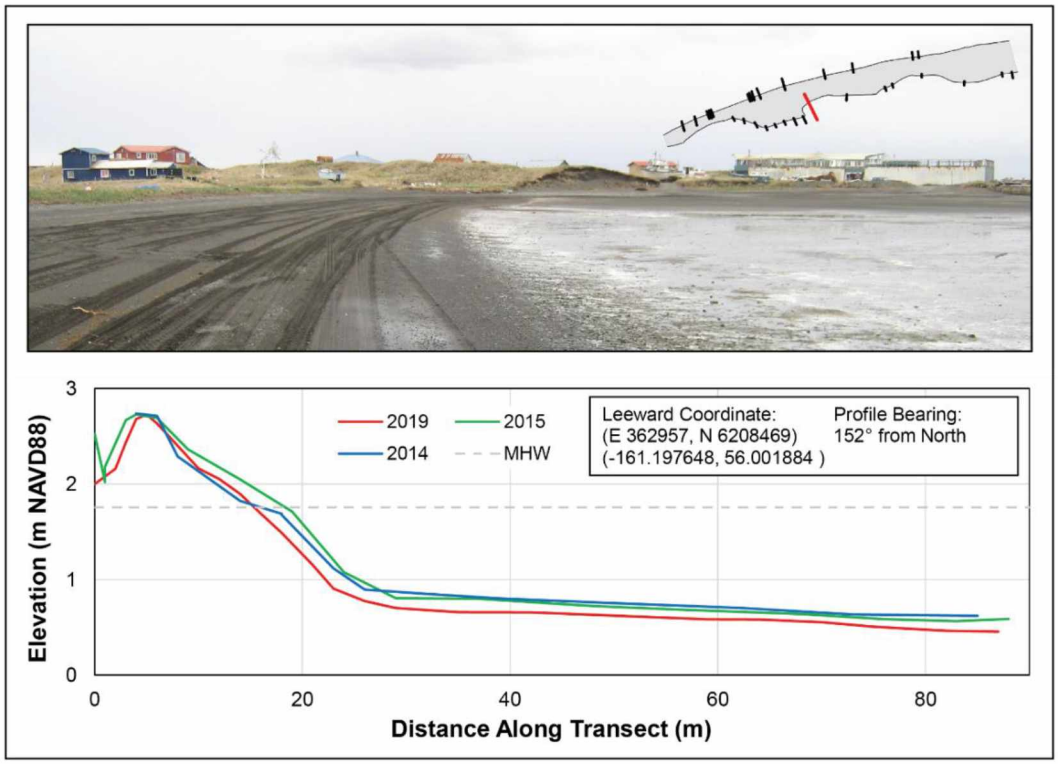

Figure B.22 Elevation profile V. Inset map denotes transect location

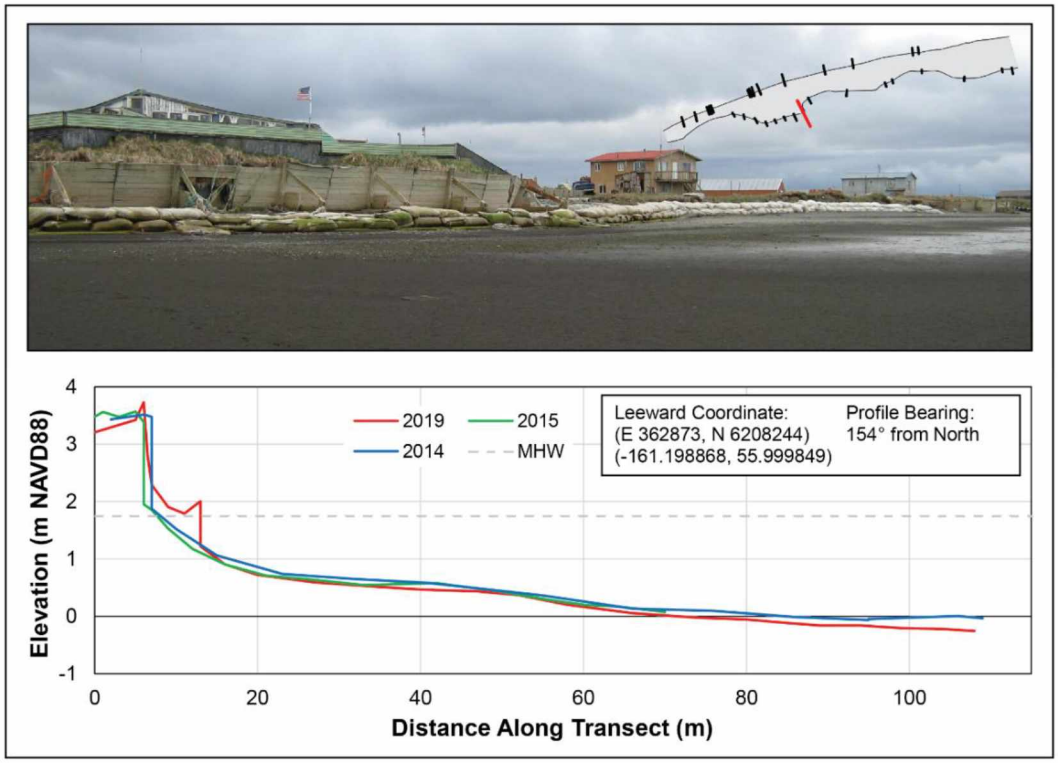

Figure B.23 Elevation profile W. Inset map denotes transect location.

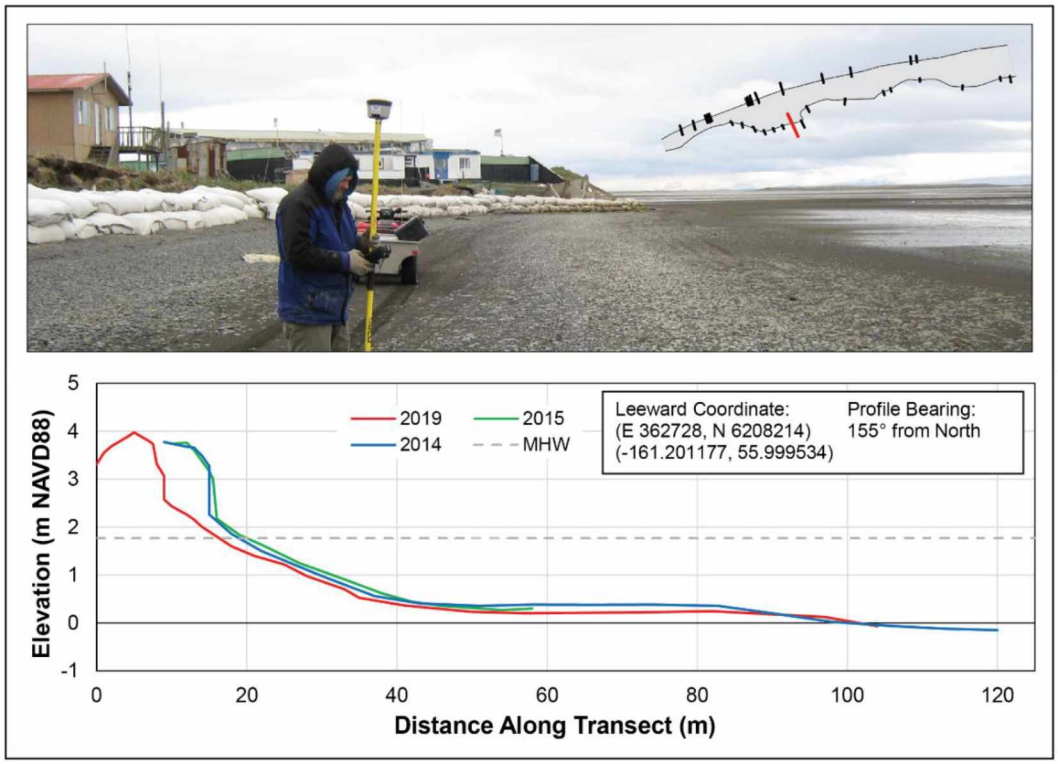

Figure B.24 Elevation profile X. Inset map denotes transect location.

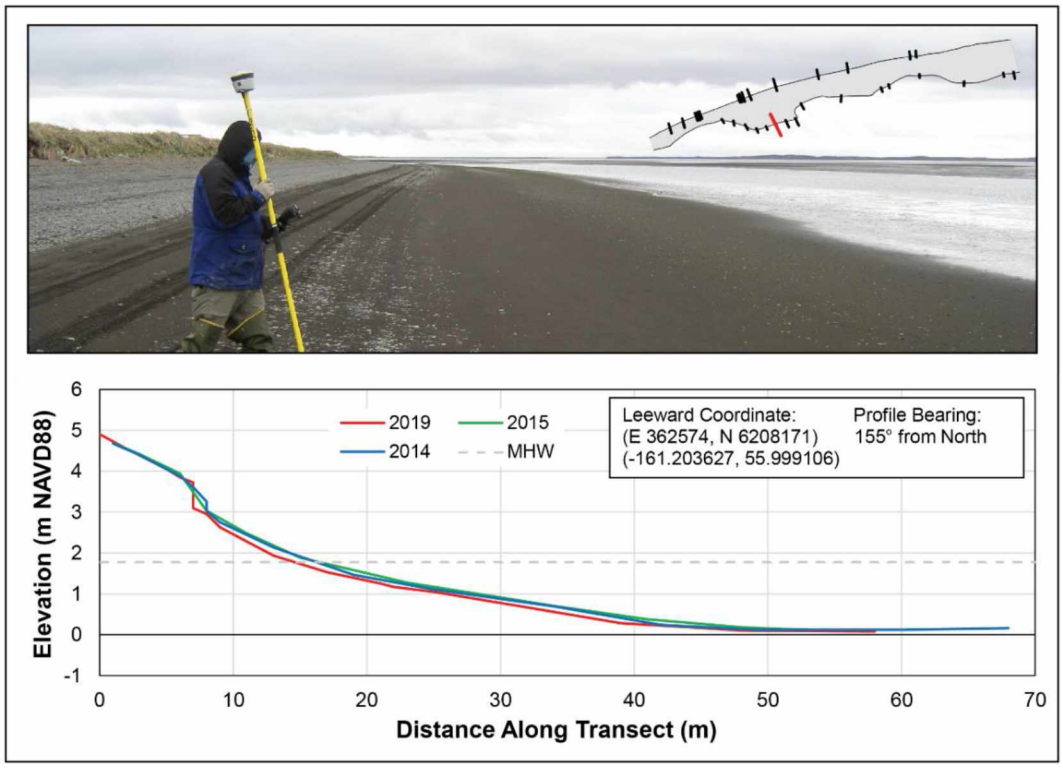

Figure B.25 Elevation profile Y. Inset map denotes transect location.

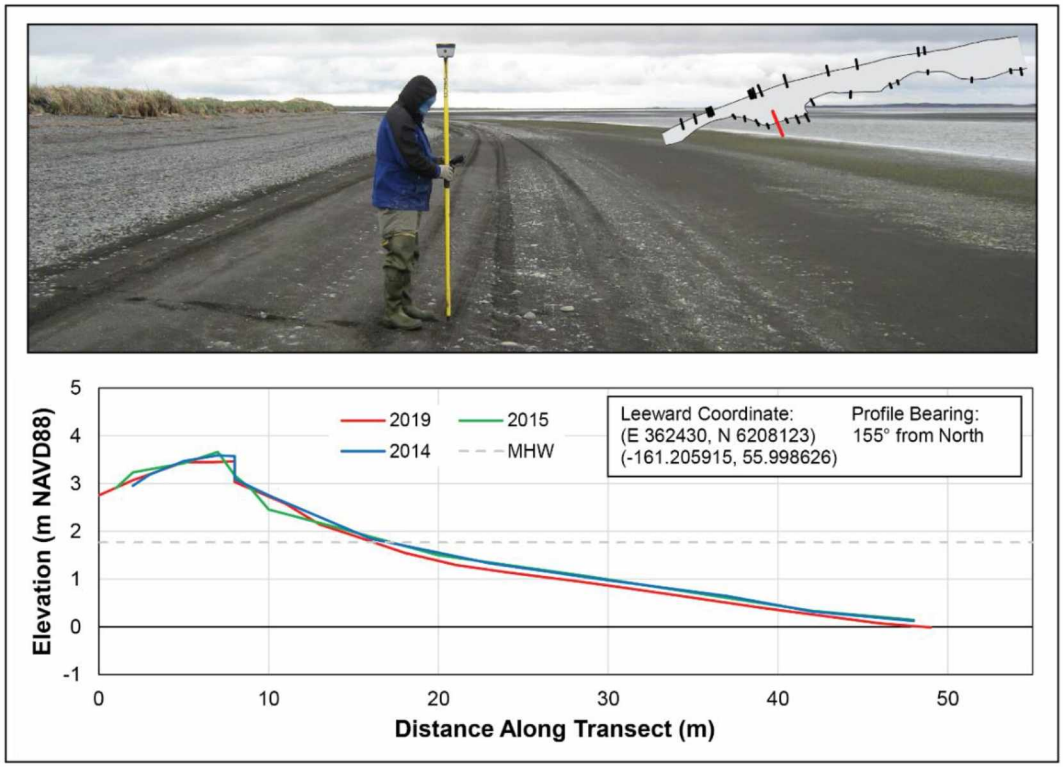

Figure B.26 Elevation profile Z. Inset map denotes transect location.

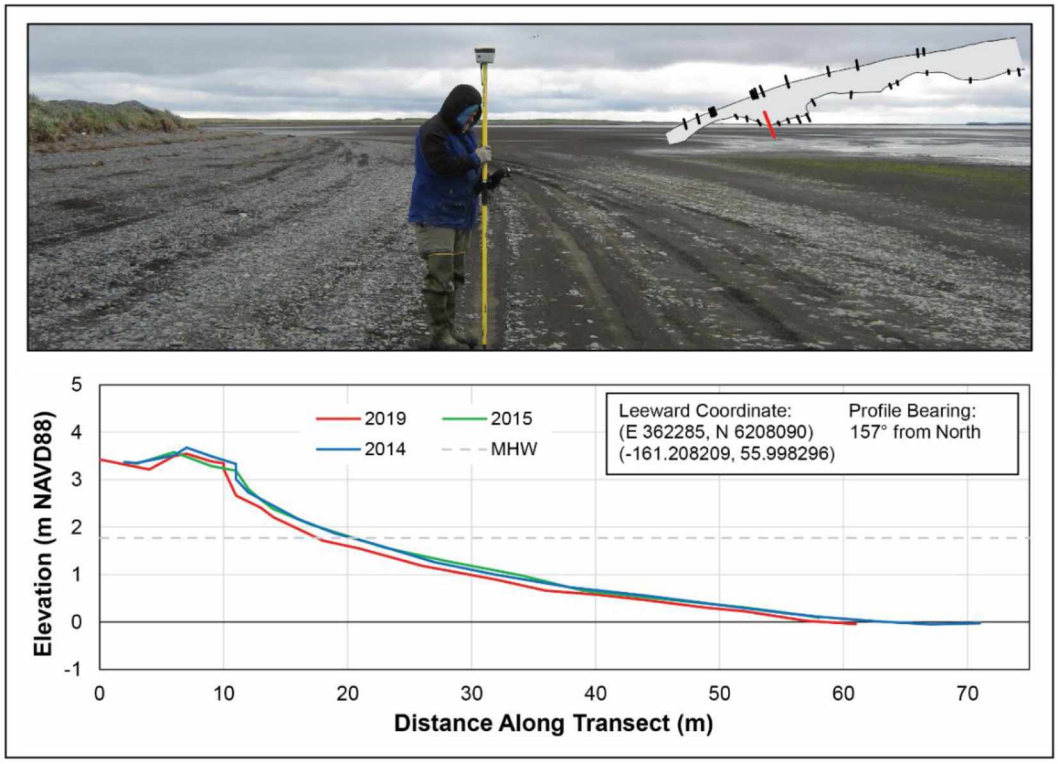

Figure B.27 Elevation profile Aa. Inset map denotes transect location.

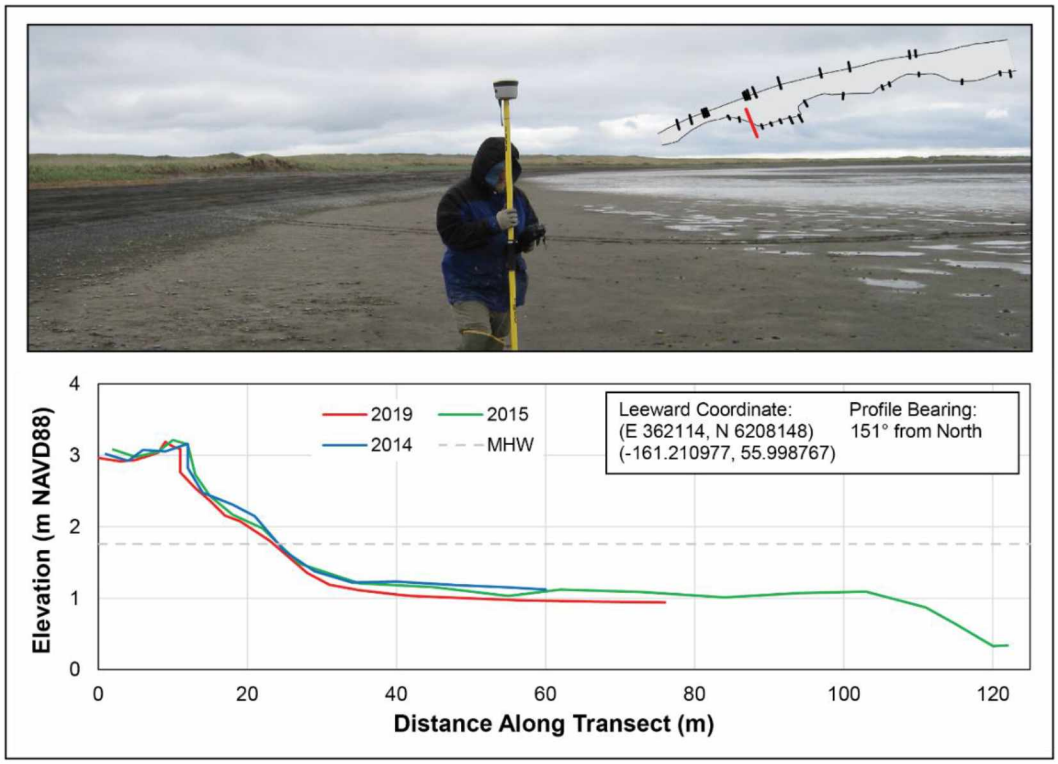

Figure B.28 Elevation profile Bb. Inset map denotes transect location.

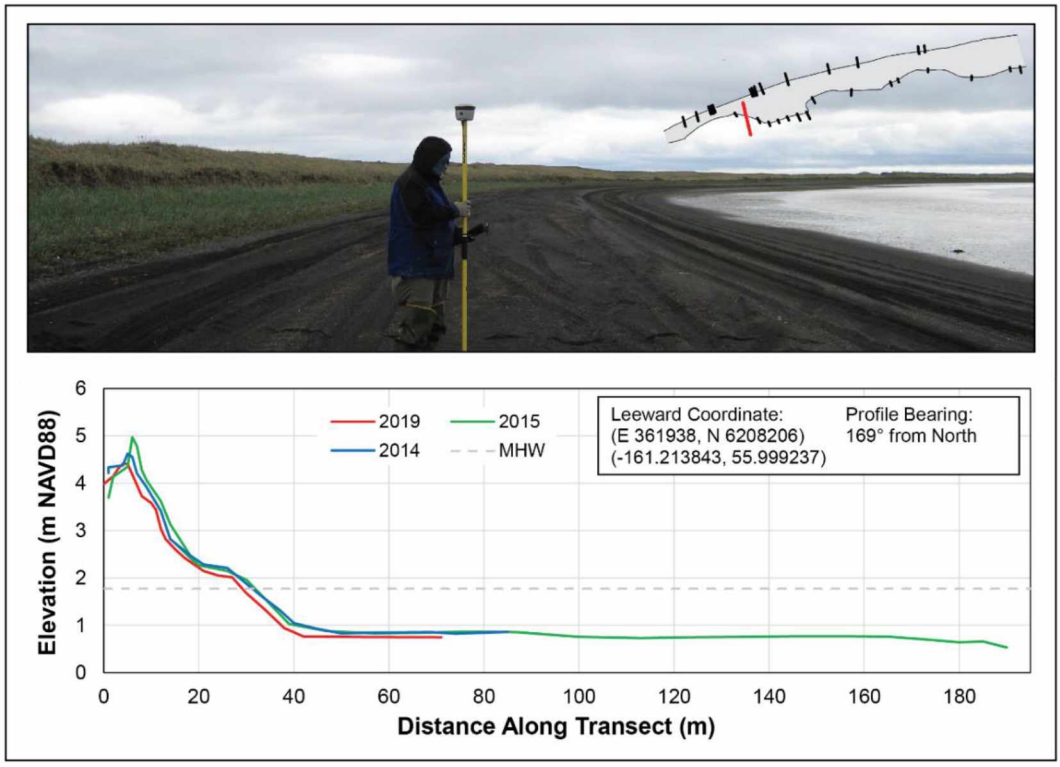

Figure B.29 Elevation profile Cc. Inset map denotes transect location.

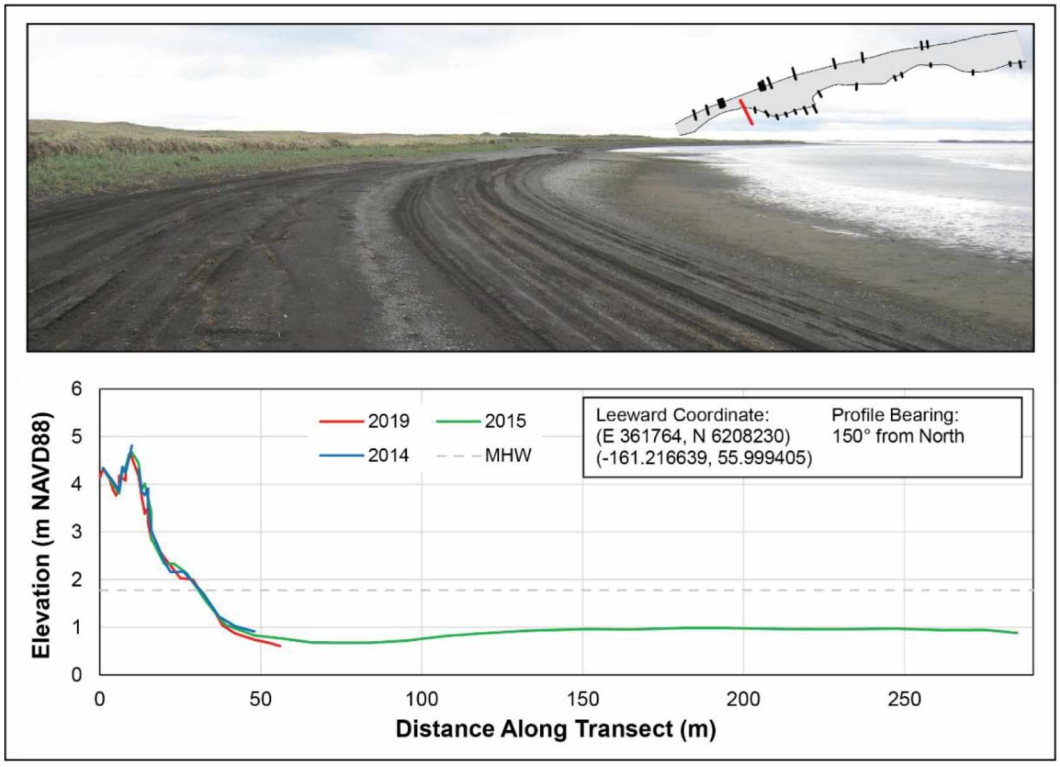

Figure B.30 Elevation profile Dd. Inset map denotes transect location.